DESIGN, FABRICATION, AND APPLICATION OF TRIBOELECTRIC NANOGENERATORS WITH TWO DIMENSIONAL MATERIALS FOR ENERGY HARVESTING AND SELF-POWERED SENSING

XIAO YANA

PhD

The Hong Kong Polytechnic University

2025

The Hong Kong Polytechnic University

School of Fashion & Textiles

Design, Fabrication, and Application of Triboelectric Nanogenerators with Two Dimensional Materials for Energy Harvesting and Self-powered Sensing

Xiao Yana

A thesis submitted in partial fulfilment of the requirements

for the degree of Doctor of Philosophy

April 2025

CERTIFICATE OF ORIGINALITY

I hereby declare that this thesis is my own work and that, to the best of my knowledge and belief, it reproduces no material previously published or written, nor material that has been accepted for the award of any other degree or diploma, except where due acknowledgment has been made in the text.

_____ _____ (Signed)

____XIAO Yana_____ (Name of student)

ABSTRACT

Energy plays a fundamental role in human civilization, and the rapid expansion of smart city development, coupled with the drive for carbon neutrality, has attracted significant research attention towards sustainable, renewable, and flexible energy harvesting solutions. Among the newly developed renewable energy sources, nanogenerators, including piezoelectric, pyroelectric, and triboelectric nanogenerators, present promising avenues to scavenge the ubiquitous, continuous, and inexhaustible mechanical energy available in nature or biomechanical energy from human movements. Triboelectric nanogenerators (TENGs) have garnered considerable interest owing to their advantages, such as simple fabrication, cost-effectiveness, environmental friendliness, and versatile applications in portable wearable electronics and natural energy harvesting. However, the development of TENGs faces challenges related to energy efficiency limits and the need for enhanced functionalities to enable integration

into various systems. The rapid advancements in multifunctional and wearable electronics have led to a growing demand for flexible and wearable power supply systems with high electric outputs and robust mechanical properties. Traditional chemical batteries, however, have become incompatible with the development of wearable electronics due to their inherent shortcomings, such as rigid complex structure, heavy weight, bulky volume, persistent recharging/replacement, and limited lifetime.

The pivotal innovations of this research study include:

Initially, two species of novel two-dimensional (2D) material Transition Metal Carbo-Chalcogenides (TMCCs), Nb_2S_2C and Ta_2S_2C, were first employed to be doped into Polydimethylsiloxane (PDMS) to explore its potential application for TENG and the best electrical performance was found at the concentration of 3 wt. ‰, i.e., open circuit voltage (Voc) of 112 V, short circuit current (Isc) of 8.6 μA, and Charge Transfer (Qsc) of 175 nC for Nb_2S_2C doped TENG, while Voc of 130 V, Isc of 9.2 μA, and Qsc of 200

nC for Ta_2S_2C doped TENG. In addition, tests on the current and output power density of the Nb_2S_2C/Ta_2S_2C doped PDMS-TENG at resistances from 1 Ω to 1 GΩ under 20 N and 2 Hz impact showed that the maximum power density of 1360 mW/m^2 and 911 mW/m^2 could be reached at 500 MΩ load respectively. Moreover, the Tribology Test revealed that the Ta_2S_2C doped PDMS, as the electronegative material, presented a lower Coefficient of Friction (COF) than Nb_2S_2C doped PDMS.

Subsequently, a triboelectric nanogenerator (TENG) based on polyvinyl alcohol (PVA) hydrogel doped with an innovative two-dimensional material g-C_3N_4 was designed. This material serves as a cost-efficient, flexible electrode and a positive dielectric component for TENGs with varying morphologies. At a dopant concentration of 2.7 wt.%, the TENG demonstrated a peak-to-peak open-circuit voltage of 80 V in single-electrode mode, significantly outperforming the pristine PVA hydrogel TENG. To showcase its potential applications, the g-C_3N_4/PVA hydrogel TENG was employed as

an electronic skin capable of tracking human body movements. Furthermore, mechanical energy harvesting devices were designed, fabricated, and evaluated with various shapes, such as discoid flakes, tubes, and spirals, operating in either single-electrode or contact-separation modes.

Furthermore, g-C_3N_4 was doped into electrospinning membrane PA_{66} to fabricate a multifunctional TENG, and the as-made TENGs showed twice enhancement in electric performance with an open-circuit voltage of 80 V and a maximum power density of 45 mW/m^2, lighting up 40 light-emitting diodes (LEDs) and powering different kinds of portable electronics. Comparison of triboelectric properties has also been made under UV light and dark environments, showing that charge transfer is very sensitive with doping g-C_3N_4. As demonstration of applications, the prepared doped composite was also made into an energy flag to scavenge natural wind energy.

Lastly, based on our previous research on a novel 2D material g-C_3N_4, we explored the

influence of g-C_3N_4 hybrid dopants with PDMS on the performance enhancement of TENGs. More specifically, systematic experiments with different ratios of hybrid dopants were conducted, including Ag nanowire with g-C_3N_4, carbon nanotube with g-C_3N_4, and MXene with g-C_3N_4. The systematic and optimization studies showed that carbon nanotube (CNT)/g-C_3N_4 at the optimal ratio of 1:1 in PDMS composite presented open circuit voltage (Voc) at 122 V, short circuit current (Isc) at 5.8 μA, and charge transfer (Qsc) at 105 nC, while Ag/g-C_3N_4 at the ratio of 3:1 with 1 wt. % in PDMS composite presented the best performance with Voc of 92 V, Isc of 4.6 μA, Qsc of 49 nC, and power density of 1.45 W/m^2. For applications, we also designed a dish and an insole with multiple TENGs for pressure sensing and multichannel data acquisition, as well as an intelligent wireless system with Bluetooth module and mobile software.

In summary, this work has successfully created flexible and wearable TENGs with

significant potential to provide sustainable power supply for multifunctional wearable applications. The findings of this research contribute to the ongoing efforts in the field of triboelectric nanogenerators, offering novel design strategies and material solutions to improve energy harvesting efficiency and broaden the applicability of these promising devices. The insights gained from this work have the potential to impact the development of next-generation energy harvesting technologies, supporting the transition towards a more sustainable and resilient energy landscape.

PUBLICATIONS

Published Journal Paper:

1. **Xiao, Y**.; Li, Z.; Xu, B*. Flexible Triboelectric Nanogenerators based on Hydrogel/g-C(3)N(4) Composites for Biomechanical Energy Harvesting and Self-Powered Sensing. *ACS Appl Mater Interfaces* **2024**, 16, 11, 13674–13684

2. **Xiao, Y.**; Li, Z.; Tan, D.; Carsten, G.; Xu, B*. Triboelectric Nanogenerators Based on Transition Metal Carbo-Chalcogenide (Nb_2S_2C and Ta_2S_2C) for Energy Harvesting and Self-Powered Sensing. *Advanced Science* 2024, 2409619

3. **Xiao, Y**, Lu J, Xu B. Synergistic Effect Study of g-C3N4 Composites for High-performance Triboelectric Nanogenerators. *Energy Mater* 2024; 4. http://dx.doi.org/10.20517/energymater.2024.155

4. **Xiao, Y**; Xu, B*; Bao, Q.; Lam, Y., Wearable Triboelectric Nanogenerators Based on Polyamide Composites Doped with 2D Graphitic Carbon Nitride. Polymers 2022, 14(15).

5. **Xiao, Yana***, Design, Fabrication, and Application Study of Droplet Tube-Based Triboelectric Nanogenerators. *Tribology in Industry* **2023,** *45* (4), 699-709.

6. Liu, X.; Xu, B. *; **Xiao, Y.**; Fang, C., Ion-sieving MXene flakes with quantum dots enable high plating capacity for dendrite-free Zn anodes. *Carbon Energy* 2024. DOI: 10.1002/cey2.603

7. S. Deng, B. Xu,* X. Liu, Y. Yang, **Y. Xiao**, S. Wang, J. Zhao, and T. Chen. Cationic Vacancy Modulation of Mn3O4 as a Superior Cathode for Durable Aqueous Zinc-Ion Batteries. *Advanced Functional Materials*, 2024, 2413711

8. Wang, Q.; Liu, X.; Han, J.; **Xiao, Y.**; Tan, D.; Yang, Y.; Zhang, J.; Xu, B., High-performance naturally crosslinked silk-based triboelectric nanogenerators for multimodal sensing and energy harvesting. *Nano Energy* 2025, 135.

Conferences

1. SERBIATRIB'23 18th International Conference on Tribology 17-19 May 2023, Kragujevac, Serbia (Proceedings: ISBN: 978-86-6335-103-5)

2. The 9th Qilu Youth Forum at Shandong University Weihai Institute for Interdisciplinary Research. Oct. 23, 2024

3. PolyU Research Student Conference (PRSC 2024), August 29, 2024

4. The 19th Chunhui Cup Innovation and Entrepreneurship Competition for Overseas Chinese Scholars, 2024

5. Novel Flexible Detachable Textile-Integrated Device with Dual-Functionality as Capacitive Mechanical Sensor and Triboelectric Nanogenerator. E-Textiles 2025 IEEE:

7th International Conference on Challenges, Opportunities, Innovations and Applications in Electronic Textiles

ACKNOWLEDGEMENTS

Completing this PhD thesis has been a remarkable journey of academic and personal development, which would not have been possible without the assistance and guidance of countless people and institutions. I gratefully acknowledge their contributions.

First and foremost, I would like to convey my heartfelt gratitude to my chief supervisor, Professor Xu Bingang, for his invaluable academic advice and professional guidance throughout the research. His unfailing support, intelligent feedback, and ongoing encouragement, as well as his commitment to quality and mentorship, have had a significant positive impact on my academic development and my character. I am extremely grateful for the patience and for pushing me to achieve the best standards.

Special appreciation to my colleagues and graduate students in our lab group, Dr. Yang Yujue, Dr. Zhang Junze, Dr. Fang Cuiqin, Dr. Li Zihua, Dr. Lu Jian, Dr. Tan Di, Dr. Deng Shenzhen, Dr. Liu Xinlong, Dr. Hanjing, and all the other members in Professor

Xu's lab and School of Fashion and Textile. All your friendship, intellectual debates, and mutual support have made the journey's hardships bearable and its victories more delightful. I greatly appreciate the administrative and technical assistance offered by the School of Fashion and Textile. The resources and facilities made available to me were critical in completing my research. This study would not have been possible without financial assistance from the Hong Kong Polytechnic University, which has allowed me to concentrate on my studies without financial constraints.

On a personal note, I would like to express my gratitude to my family and friends for their constant support and encouragement throughout this journey. To my parents, your faith in me has been a constant source of strength, and your patience, understanding, and love have served as a steadfast anchor for me throughout this process. I want to thank everyone who participated and collaborated on this study. Your willingness to

contribute your time and insights has proven beneficial. Thank you all for taking part in our journey. This achievement is as much yours as mine.

Table of Contents

LIST OF FIGURES

Ta_2S_2C/PDMS composite samples. (c) EDS-elemental mapping images of the Nb_2S_2C/PDMS composite sample. (d) EDS-elemental mapping images of the Ta_2S_2C/PDMS composite sample. (e-f) Raman pattern of pure PDMS, Nb_2S_2C/PDMS composite, and Ta_2S_2C/PDMS composite.

Figure 3.3 Morphology and elemental analysis (a) EDS-elemental mapping images of the Nb_2S_2C/PDMS composite. (b) EDS-elemental mapping images of the Ta_2S_2C/PDMS composite. (c) XRD Pattern of Nb_2S_2C/PDMS composite. (d) XRD Pattern of Ta_2S_2C/PDMS composite. (e) Frequency dependence of dielectric constant of Nb_2S_2C/PDMS composite with different concentrations of 0, 1 wt. ‰, 3 wt. ‰, and 10 wt. ‰. (f) Frequency dependence of dielectric constant of Ta_2S_2C/PDMS composite with different concentrations of 0, 1 wt. ‰, 3 wt. ‰, and 10 wt. ‰.

Figure 3.4 XPS spectra of TMCC/PDMS composites. (a) Nb_2S_2C, (b) Nb 3d, (c) C 1s, (d) S 2p. (e)Ta_2S_2C. (f) Ta 4f, (g) C 1s, (h) S 2p.

Figure 3.5 Electric performance at 40 N, 3 Hz, 16 cm^2 (a) Open circuit voltage, (b) Short circuit current, (c) Charge transfer of Nb_2S_2C based TENG at different weight ratios, and (d) Open circuit voltage, (e) Short circuit current, (f) Charge transfer of Ta_2S_2C based TENG at different weight ratios.

Figure 3.6 Different frequency and force on 3 wt. ‰ Nb_2S_2C based TENG of 4 cm^2 size for electrical performance (a) Open circuit voltage (b) Short circuit current (c) Charge transfer at different frequencies from 1 Hz to 7 Hz at a force of 20 N and (d) Open circuit voltage (e) Short circuit current (f) Charge transfer at different impact forces of 10 N, 20 N, 30 N, 50 N, and 100 N at a frequency of 2 Hz.

Figure 3.7 Different frequency and force on 3 wt. ‰ Ta_2S_2C based TENG of 4 cm^2 size for electrical performance (a) Open circuit voltage (b) Short circuit current (c) Charge transfer at different frequencies from 1 Hz to 7 Hz at a force of 20 N and (d) Open circuit voltage (e) Short circuit current (f) Charge transfer at different impact forces of

10 N, 20 N, 30 N, 50 N, and 100 N.

Figure 3.8 (a) Electrical circuit of TENG charging capacitor and powering electronic device. (b) The voltage curve of charging capacitors of 1.5 μF, 100 μF, and 330 μF and the inset of (b) is the image of powering clock by the charged capacitor. (c) Current and output power density curve of the Nb_2S_2C based TENG at different resistances from 1 Ω to 2 GΩ under 20 N and 2 Hz impact. (d) Current and output power density curve of the Ta_2S_2C based TENG at different resistances from 1 Ω to 2 GΩ under 20 N and 2 Hz impact.

Figure 3.9 (a) Applications of TMCC-TENG. The output response of wearable harvester and sensor under mechanical movements (i) clapping and (ii) running. The self-powered sensing at different positions of the human body (iii) elbow and (iv) finger bending. (b) Durability experiments for TENG (i) before and after six months and (ii) operated for 35,000 cycles at a frequency of 3 Hz.

Figure 3.10 Tribology Test for friction performance of pristine PDMS, Nb_2S_2C/PDMS composite, and Ta_2S_2C/PDMS composite substrate in ball-on-disk experiments (a) Derivatives and average COF of 3 times experiments from time 0 s to 850 s at the load of 1 N. (b) average COF after data stabilization (150s after the start of the experiment approximately) at the load of 1 N, 5 N,10 N, 20 N, 30 N, respectively. (c) Depth difference and SEM Micrograph of the steel ball and pristine PDMS, Nb_2S_2C/PDMS composite, and Ta_2S_2C/PDMS composite after the consistent ball-on-disk experiment for one hour under 1N.

Figure 4.1 (a) Schematic routes for the preparation of the PVA hydrogel and g-C_3N_4/PVA hydrogel. (b) Photographs of PVA hydrogels in different deformation states, such as original, elongated, and twisted. (c) Photographs of PVA hydrogels depicting the self-healing capability: original state, cut in half, automatic recovery within 15 minutes. (d) SEM of pure PVA hydrogel and g-C_3N_4/PVA hydrogel. (e) EDS mapping

of g-C_3N_4/PVA showing the existence of C, N, and O elements. (f) FTIR spectra of g-C_3N_4/PVA hydrogel and pure g-C_3N_4 powder.

Figure 4.2 (a) XPS survey spectra of g-C_3N_4 dopant PVA hydrogel (The additional 2 peaks marked * originated from the glass substrate used in XPS measurements) (b) High-resolution XPS spectrum showing the binding energy of N electrons. (c) XPS spectrum showing the binding energy of C-C and C-N.

Figure 4.3 The working mechanism of the hydrogel-TENG (a) Schematic structure and working principle of the single-electrode mode hydrogel-based TENG for energy harvesting and (b) demonstration of electrical potential distribution by COMSOL software simulation.

Figure 4.4 Demonstration of the hydrogel TENG for energy harvesting at an impact force of 30 N and frequency of 2 Hz (a) Open circuit voltage (b) Short circuit current (c) Charge Transfer of single electrode TENG of different external substrate materials

of Kapton, PTFE, Copper-nickel conductive fabric, copper coil (Sort by descending order of the electrical output performance). (d) Open circuit voltage (e) Short circuit current (f) Charge Transfer of single electrode hydrogel TENG at different concentrations of g-C_3N_4 by weight ratios (g-C_3N_4: PVA) of 0.4 wt. %, 1.2 wt. %, 2.7 wt. %, 3.8 wt. %, and 5.7 wt. %, respectively.

Figure 4.5 (a) Open circuit voltage (b) Short circuit current (c) Charge transfer of the concentration from 0 to 50 wt. %. (d) Open circuit voltage (e) Short circuit current (f) Charge transfer of the concentration from 7 wt. % to 25 wt. %. (g) Open circuit voltage (h) Short circuit current (i) Charge transfer of the concentration from 0.4 wt. % to 5.7 wt. %

Figure 4.6 performance of 2.7 wt. % g-C_3N_4/PVA hydrogel TENG (a) Open circuit voltage (b) Short circuit current at different impact forces of 20 N, 100 N, and 300 N,

respectively. (c) Open circuit voltage (d) Short circuit current at different frequencies from 1 Hz to 7 Hz.

Figure 4.7 (a) Mechanical property of PVA hydrogel with different dopants. (b) Charging behavior of the g-C_3N_4/PVA hydrogel TENG with capacitors of 1.5 μF, 4.7 μF, 22 μF, and 100 μF under the same working circumstances. (c) The relationship between short-circuit current and calculated power densities versus the resistance of the external loads of PVA hydrogels. (d) Dependence of short-circuit current and calculated power densities under different resistances of the external loads of 2.7 wt. % g-C_3N_4/PVA hydrogel TENG under the same circumstances. (e) Durability test of g-C_3N_4/PVA hydrogel TENG for a constant strike of 9,200 cycles. (f) Daily measurements for 6 consecutive days. (g) The electrical performance of original g-C_3N_4/PVA hydrogel TENG and recycled TENG.

Figure 4.8 (a) Morphology for tube hydrogel TENG (3 cm) with pure PVA as electrode (single electrode mode) and positive tribo-layer (contact separation mode). Comparison of their (b) open circuit voltage, (c) short circuit current, and (d) charge transfer by simple slapping. (e) Morphology for the single electrode tube hydrogel TENG (30 cm) fabricated into spiral and electrical output comparison with pure PVA TENG and g-C_3N_4/PVA hydrogel TENG of (f) open circuit voltage, (g) short circuit current, (h) charge transfer, by simple slapping.

Figure 4.9 Output voltages generated by different stretched states and self-powered sensors for monitoring body movements (a) Output voltage signals of tube hydrogel-TENG in response to the elbow bend at 45°, 90°, and 120°. Voltage signals of the flake hydrogel-TENG in response to continuous bends of (b) elbow, (c) wrist, (d) finger, (e) foot stepping, (f) hand clapping. (g) Demonstration of g-C_3N_4/PVA hydrogel TENG

light up 38 LEDs by gentle hand slapping. The photograph of a commercial (h) watch and (i) electrical calculator powered by a capacitor charged by hydrogel TENG.

Figure 5.1 (a) Schematic illustration for preparation of electrospinning membrane. (b) SEM images of (b1) Electrospinning PA_{66} and (b2) Nylon textile cloth at different magnifications. (c) Photographic images of electrospinning membrane PA_{66} with different concentrations (i) pure (ii) 0.1 wt. % (iii) 0.4 wt. % (iv) 0.7 wt. % of g-C_3N_4. (d) Fourier transform infrared (FTIR) absorption spectra for g-C_3N_4 powders. (e) Thermal gravimetric analysis (TGA) of PA_{66} and g-C_3N_4.

Figure 5.2 (a) Schematic diagrams of working mechanism for contact separation mode electrospinning membrane TENG with g-C_3N_4 dopant. (b) Simulation results of electrical potential distribution by COMSOL software.

Figure 5.3 Output performance comparison of electrospinning membrane from pure PA_{66} and electrospinning membrane PA_{66} based on 0.1 wt. % doped g-C_3N_4 (low

concentration) (a) open-circuit voltage (b) short circuit current (c) charge transfer. Output performance comparison of electrospinning membrane PA_{66} based on 0.1 wt. % doped g-C_3N_4(low concentration) and 0.4 wt. % doped g-C_3N_4 (high concentration) (d) open-circuit voltage (e) short circuit current (f) charge transfer.

Figure 5.4 (a) Open-circuit voltage (b) Short-circuit current (c) Charge transfer of PA_{66} electrospinning membrane TENG with different impacting forces at 40 N and 100 N intensity under the same frequency of 3 Hz. (d) Open-circuit voltage (e) Short-circuit current and (f) Charge transfer of PA_{66} electrospinning membrane TENG with different frequencies from 1 Hz to 8 Hz under the same impact force of 100 N.

Figure 5.5 Electrical output comparison of electrospinning membrane PA_{66} TENG with doped g-C_3N_4 under UV light condition and dark condition (a) open-circuit voltage, (b) short circuit current, (c) charge transfer. (d) Illustration of light and electric field influence. (e) Energy bandgap theory of g-C_3N_4. (f) The molecular structural formula

of g-C_3N_4.

Figure 5.6 Electronic Output of PVDF electrospinning membrane with and without g-C_3N_4 doping of (a) open-circuit voltage, (b) short circuit current, and (c) charge transfer.

Figure 5.7 (a) Open-circuit voltage (b) short circuit current (c) charge transfer output of PAN electrospinning membrane TENG with different frequencies 2 Hz, 3 Hz, 4 Hz, 5 Hz, 6 Hz, 7 Hz, 10 Hz under the same impact force of 100 N.

Figure 5.8 (a) Charging voltage curves of the electrospinning membrane TENG in the process of continuously powering devices like calculators and electronic watches. (b) Illustration of electrospinning membrane TENG for lighting up 40 LEDs. (c) Dependence of output current and average power density of the electrospinning membrane TENG on load resistances. (d) Charging curves of 1.5 μF, 4.7 μF, and 10 μF capacitors.

Figure 5.9 (a) Application of electrospinning membrane TENG for harvesting human

motions. (b) Electrospinning membrane TENG for harvesting wind energy under different levels of fan speed.

Figure 6.1 Illustration of the fabrication of hybrid dopants TENG (taking dopants-silver nanoparticles and g-C_3N_4 powder as an example). (a) Mixing of PDMS, silver nanoparticles, and g-C_3N_4 powders. (b) Blade coating of the mixture. (c) Structure of TENG. (d) XRD pattern of g-C_3N_4 powder. (e) FTIR spectra for PDMS composites with different ratios of Ag/g-C_3N_4. (f) Raman spectra of a sample with a total of 1 wt. % dopant of Ag/g-C_3N_4 at different ratios in PDMS composite. (g) SEM of Ag/g-C_3N_4 PDMS composite and EDS mapping of elements.

Figure 6.2 (a) XPS survey spectra of Ag/g-C_3N_4 PDMS composite. High-resolution XPS spectrum showing the binding energy of (b) C, (c) Ag, and (d) N electrons.

Figure 6.3 (a) (I-IV) Schematic diagrams of the working principle of contact and separation mode TENG. (b) Simulation results of electrical potential distribution by

COMSOL Multiphysics software. (c) Equivalent circuit of a self-powered system: TENG, capacitor, another device, and rectifier changing AC to DC. (d) Two opposite electric peaks during a single circle of contact and separation. (e) Schematic structure of dopant/PDMS TENG.

Figure 6.4 Electric performance of hybrid dopant TENG. (a) Open circuit voltage, (b) Short circuit current, (c) Charge transfer of TENG with different ratios of carbon nanotube and g-C_3N_4 at a total weight proportion of 1 wt. %. (d) Open circuit voltage, (e) Short circuit current, (f) Charge transfer of TENG with different ratios of Ag nanoparticles and g-C_3N_4 at a total weight proportion of 1 wt. %.

Figure 6.5 (a) Open circuit voltage, (b) Short circuit current, (c) Charge transfer at different frequencies from 1 Hz to 6 Hz and (d) Open circuit voltage (e) Short circuit current (f) Charge transfer at different impact forces of 10 N, 50 N, 100 N, and 200 N, respectively.

Figure 6.6 (a) Open circuit voltage, (b) Short circuit current, and (c) Charge Transfer of TENG with nickel-coated carbon nanotubes, nickel-coated carbon nanotubes together with g-C_3N_4. (d) Open circuit voltage, (e) Open circuit voltage, and (f) Charge Transfer of TENG with multiwall carbon nanotubes, g-C_3N_4, hybrid multiwall carbon nanotubes and g-C_3N_4. (g) Open circuit voltage, (h) Short circuit current, (i) Charge Transfer of TENG with MXene with different ratios of g-C_3N_4. (j) Open circuit voltage, (k) Short circuit current, and (l) Charge Transfer of TENG with Ag, Ag and g-C_3N_4, AgO, AgO and g-C_3N_4.

Figure 6.7 (a) The instantaneous peak power density of (a) Ag/g-C_3N_4 PDMS TENG (b) CNT/g-C_3N_4 PDMS TENG at a series of external resistance loadings and the corresponding current output. (c) The equivalent circuit of charging capacitance and photographic demonstration. (d) Durability study for Ag/g-C_3N_4 PDMS TENG after (1) 100, 500, 1000, 5000, 10000, and 20000 cycles, respectively, as well as (2) 0-hour, 1-

hour, 5 hours, 1 day, 2 days, 10 days, respectively. (e) Applications of Ag/g-C_3N_4 PDMS TENG as self-powered wearable sensors.

Figure 6.8 (a) Bar chart comparison of average sensing signals for a four-channel pressure sensing system, inset is the pattern illustration and real picture. (b) Sensing signal patterns by the sequence of pressing channels 1, 2, 3, and 4 in succession sequentially. (c) Signal pattern of the two-TENG insole while walking with the center of gravity at the front. (d) Signal pattern of the two-TENG insole while walking with the center of gravity at the back. (e) Bar chart comparison of average sensing signals while walking with center at the front, center at the back, and center at the middle, respectively, inset is the photo of the double-TENG insole.

Figure 6.9 Monitoring of elbow bending angles by pasting hybrid dopant PDMS composite TENG on the elbow (a) stretching, (b) moving to 90°, (c) bending to 30°. Voltage generated while moving (d) from position a to b, (e) a to c, (f) from position b

to c. (g) Bluetooth circuits intelligent wireless system and interface of mobile software.

LIST OF TABLES

ABBREVIATIONS

CNF	Copper-nickel coated conductive Polyester fabric (CNF)
LED	Light-emitting diode
PTFE	Polytetrafluoroethylene
PVDF	Polyvinylidene Fluoride
PLA	Polylactic Acid
PI	Polyimide
PET	Polyethylene terephthalate
PAN	Polyacrylonitrile
LM	Liquid metal
SEM	Scanning electron microscopy
EDS	Energy dispersive spectrometer
FTIR	Fourier transform infrared spectroscopy
TGA	Thermogravimetric analysis
XRD	X-ray diffraction analysis
XPS	X-ray photoelectron spectroscopy
SERS	Surface-enhanced Raman scattering
SPR	Surface plasmon resonance
CNT	Carbon nanotube
DMF	N, N-Dimethylformamide
HMI	Human-machine interface
IoT	Internet of Things
PDMS	Polydimethylsiloxane
2D	Two Dimensional
PA_{66}	Polyamide 6,6
PVA	Polyvinyl alcohol
TMD	Transition Metal Dichalcogenide
TMCC	Transition Metal Carbo-Chalcogenide
g-C_3N_4	Graphitic Carbon Nitride
TENG	Triboelectric Nanogenerator
PENG	Piezoelectric nanogenerator

TPU	Thermoplastic Polyurethane
FEP	Fluorinated ethylene propylene
MOF	Metal-organic framework
GO	Graphene oxide
BP	Black phosphorus
COF	Coefficient of Friction
h-BN	hexagonal boron nitride
AC	Alternating current
DC	Direct current
HOMO	Highest occupied molecular orbital
LUMO	Lowest unoccupied molecular orbital

CHAPTER 1 Introduction

1.1 Background

Sustainable and net-zero carbon emission power sources are acting as a thriving factor to alleviate the energy crisis and reduce fossil fuel pollution and global warming due to rising energy consumption. The energy consumption structure is transitioning from reliance solely on fossil fuels to a more diversified energy portfolio. The development and utilization of new energy sources, such as solar energy, hydropower, geothermal energy, and biomass energy, alongside innovative energy harvesting methods like nanogenerators, have become pivotal areas for prioritized development. For instance, self-driving power source systems that harvest energy from the environment without requiring maintenance are highly attractive. With advancements in nanoscience and technology, especially in the field of nanomaterials preparation, researchers are using nanomaterials to design and prepare devices that can produce electricity on a small

scale in different ways. Promisingly, collecting electric energy generated by triboelectrification or using the method to convert irregular kinetic energy from daily life into usable electric energy is expected to have an important impact on our daily lives, coupled with the rapid expansion of wearable technologies and Internet-of-Things (IoT) devices. In this context, nanogenerators have emerged as a pivotal technology in the advancement of clean energy solutions. These devices, including piezoelectric nanogenerators (PENGs), pyroelectric nanogenerators (PyNGs), moisture-enabled generators (MEGs), triboelectric nanogenerators (TENGs), tribovoltaic nanogenerators (TVNGs), and electromagnetic generators (EMGs), are designed to efficiently and sustainably capture and transform ambient energy into usable electrical power, such as mechanical, thermal, and solar energy.

Triboelectricity and static electricity are prevalent phenomena, existing in various aspects of daily life, from human movements like walking to various mechanical

movements like driving. Despite their ubiquity, these energy forms are often neglected due to the difficulties associated with their collection and utilization. Triboelectric nanogenerators, invented by Z.L. Wang, are gaining traction as a method for harvesting low-frequency, low-amplitude mechanical energy. The fundamental mechanism of triboelectric nanogenerators involves the coupling of triboelectrification and electrostatic induction, allowing operation in four modes: vertical contact separation, lateral sliding, single electrode mode, and freestanding triboelectric layer mode. Vertical contact separation utilizes relative motion perpendicular to the interface, whereas sliding mode employs relative displacement parallel to the interface[1]. The single electrode mode uses the ground or human body as the reference electrode, enhancing adaptability for energy harvesting, whereas freestanding modes utilize pairs of electrodes with electric output from asymmetric charge distribution[2]. TENG's high prospective use and potency scenario have also been boosted by hybridizing its many

modes or combining with other energy conversion devices.[3] Particularly, TENGs are attractive owing to their low costs, mechanical flexibility[4], ease of assembly, and their low-frequency working range[5]. For TENGs[6], two kinds of materials with differing electronegativities and electrodes are used, typically polymers such as polyethylene terephthalate (PET), Polydimethylsiloxane (PDMS), Polyamide (PA) and polyimide (PI)[7-8]. Polymers generally process a low dielectric constant, resulting in limited capacitance and poor charge retention capacity[9] , particularly when applied in TENGs for dual functions as energy harvesters and self-powered sensors. To date, efforts to improve TENG's electrical output have focused on enhancing the dielectric performance of triboelectric materials[10-11] as well as increasing the accumulated charge transfer density[12-13]. The introduction of high permittivity particles[14] into the substrate[15-16] at the interface, between the triboelectric materials[17], or with the electrode[18-20] has been proven effective in increasing the performance of TENG,

utilizing a diverse array of materials from carbon nanotubes[21] to ferromagnetic barium titanate[22], various two-dimensional materials[23-24], and liquid metals[25] etc. In addition to the need to improve the electric properties of TENGs, research indicates that their tribological properties are of paramount importance as well[26]. Specifically, wear resistance during sliding is a crucial factor in limiting their applicability[27]. Moreover, water-based graphene oxide can serve as a lubricant to enhance current density and reduce wear[28]. In this context, the addition of two-dimensional (2D) materials to the substrate matrix can positively influence wear behavior[29], in addition to improving the electrical performance of TENGs[30]. 2D materials with unique structures and properties at the atomic or molecular level have been widely studied in recent years, including graphene/graphene oxide[30], transition metal dichalcogenides (TMDs)[31], MXene[32], carbon nitride[23], and transition metal carbo-chalcogenide (TMCC)[33]. These materials have garnered significant attention in electronics, optics, and energy fields due to their

unique properties[34]. MXenes, belonging to the family of transition metal carbides and nitrides[35-36] are renowned for their good chemical stability, high mechanical strength and excellent electrical conductivity. The most commonly used TMDs are molybdenum disulfide (MoS_2) and tungsten disulfide (WS_2), characterized by different electronic band structures[37] and polymorphic structures[38]. The single-layered TMCC of these two species (Nb_2S_2C and Ta_2S_2C) was first successfully realized from multilayered Nb_2S_2C[39] and Ta_2S_2C through electrochemical lithiation and sonication in 2022, and it was experimentally verified that the delaminated Nb_2S_2C outperformed its multilayered precursor material as an electrode material in electrochemistry[40].

To address these challenges in energy, this research aims at designing, exploring, and developing enhanced TENGs with high performance and multifunctionality for mechanical energy harvesting, self-powered sensing and biomechanical sensors. This will be achieved by searching for new materials or composites, developing innovative

structures, and employing facile fabrication methods, especially through the adoption of two-dimensional materials. From the perspective of novel material, two species (Nb_2S_2C and Ta_2S_2C) of TMCCs, were first doped into PDMS to develop TENG. Moreover, the tribological performance was evaluated with the same materials. Subsequently, a PVA hydrogel TENG doped with graphitic carbon nitride was developed, which could act as both a cost-effective flexible electrode and a positive dielectric for TENG with different morphologies. Consequently, g-C_3N_4 in electrospinning membrane PA_{66} was fabricated into a multifunctional TENG. A comparison of triboelectric properties was conducted under UV light and dark environments, showing that charge transfer is highly sensitive to g-C_3N_4. Afterward, based on previous research on the novel 2D material g-C_3N_4, hybrid dopants were creatively studied, and systematic experiments with different dopant ratios, including Ag nanowire with g-C_3N_4, carbon nanotube with g-C_3N_4, and MXene with g-C_3N_4,

were conducted, These TENGs were further designed as a dish and an insole with multiple TENGs for pressure sensing and multichannel data acquisition, as well as an intelligent wireless system with a Bluetooth module and mobile software.

1.2 Research Objectives

This project aims at developing functional materials and novel structures for innovative flexible TENG for sustainable and renewable energy harvesting methods, including

(1) To introduce a new family of 2D material TMCCs (two species-Nb_2S_2C and Ta_2S_2C) into TENG for output enhancement.

(2) To develop g-C_3N_4 hydrogel as both tribopositive material and electrode to fabricate TENG with different morphologies and functions.

(3) To explore and synthesize g-C_3N_4, together with the electrospinning technique, to design and fabricate a nanofiber network structured TENG.

(4) To expand dopant and substrate and explore more applications together with

Bluetooth intelligent system and multichannel data acquisition.

(5) To integrate the prepared TENGs for applications in biomechanical energy harvesting and self-powered sensing.

The novel structure designs and efficient fabrication methods are also explored and studied in a facile and versatile manner. For the above-mentioned objectives, we adopted two species of TMCCs (Nb_2S_2C and Ta_2S_2C) into PDMS to develop TENG, TMCC was considered and selected because it could be assumed as combination of TMD and MXene and has not yet been researched. Moreover, the tribology performance was also evaluated with the same materials. Subsequently, we developed a PVA hydrogel TENG doped with graphitic carbon nitride (g-C_3N_4, which has some similarity with graphene), which could act as both cost-effective flexible electrode and positive dielectric for TENG with different morphologies. Consequently, g-C_3N_4 in electrospinning membrane PA_{66} was fabricated into a multifunctional TENG. A

comparison of triboelectric properties has also been made under UV light and dark environments, showing that charge transfer is very sensitive with g-C_3N_4. Based on our previous research on novel 2D material g-C_3N_4, hybrid dopants were creatively studied, and systematic experiments with different ratios of dopants, including Ag nanowire with g-C_3N_4, carbon nanotube with g-C_3N_4, and MXene with g-C_3N_4. We also designed a dish and an insole with multiple TENGs for pressure sensing and multichannel data acquisition, as well as an intelligent wireless system with Bluetooth module and mobile software.

1.3 Research Methodologies

Methods to achieve the research objectives are listed as follows:

(1) Thorough literature review and analysis of the current research situation and research gap of energy harvesting applications for triboelectric nanogenerators.

(2) Investigation of the optimal fabrication methods and conditions for preparation of

enhancements for dielectric materials by review and experimental trials.

(3) Synthesizing and evaluating various composite functional materials with different operational conditions and parameters, such as utilizing facile electrospinning techniques or 3D printing approaches.

(4) Designing and fabricating innovative structures for TENG to optimize output and achieve the purpose of multifunctionality.

(5) Evaluating the performance of as-made TENGs and comparing the outputs and enhanced functions with prior TENGs and incorporating the energy harvesting devices along with proper applications such as environment-friendly conversion as renewable power sources or self-powered sensors for human-machine interaction.

(6) Integrating and utilizing the fabricated TENGs for application into mechanical energy harvesting from nature or human and self-powered sensor systems, evaluating, and summarizing the mechanism, intrinsic natural regulation of triboelectrification, and

macro analysis for optimized energy structure toward a carbon-neutral smart city.

1.3.1 Material Selection and Modification

The selection of materials is generally referred to as triboelectric series [30, 41]. Despite that, the choices for triboelectric materials are extensive; selecting appropriate negative and positive triboelectric polarities is pivotal to obtaining expected performance. For example, the typical triboelectric material PDMS served as one option of ideal frictional materials for its flexibility and non-poisonousness, and it can also be easily solidified from viscous state. Other materials include Nylon (PA_{11} or PA_{66}), cotton, polyvinyl alcohol (PVA), Polyvinylidene Fluoride (PVDF), Polytetrafluoroethylene (PTFE), thermoplastic polyurethane (TPU), polyacrylonitrile (PAN), polylactic acid (PLA), PI, PET, aramid fiber, etc. Most importantly, novel materials dopants such as 2D materials and metal-organic frameworks in the above-mentioned common textile materials can greatly affect morphology, material properties, and output performance.

1.3.2 Fabrication and Structure

For microstructure, constructing nanostructure on the surface of triboelectric materials has been verified to achieve high-performance electrical outputs. Electrospinning has been explored to economically fabricate nanofibrous surface microstructural membranes and ultrathin fibers from viable common textile materials as an efficient technique that has mechanical stretching, electric poling, nanoparticle surface modification, large surface areas, and intrinsic porosity with inherent advantages of textile. Innovative microstructure fabrication methods mainly adopt 3D printing techniques, with a combination of software such as AutoCAD, Rhino, SolidWorks, and Autodesk 3dmax to draw unique structure designs as well as simulation software such as COMSOL.

1.3.3 Characterization, Measurement, and Devices

Field Emission Scanning Electron Microscope (SEM, Tescan MIRA) was used to

characterize the morphology and Energy Disperse Spectroscopy (EDS) data were acquired simultaneously. X-ray diffraction (XRD) pattern with scanning from 5 to 70° (2θ) was recorded on an X-ray diffractometer (Rigaku SmartLab) to identify the crystalline phase. X-ray photoelectron spectroscopy (XPS) spectra were investigated on an ESCALAB210 spectrometer. The dielectric constant was measured using a precision LCR meter (Keysight E4980A). Fourier transform infrared spectroscopy (FTIR) absorption spectra were carried out on a Perkin Elmer spectrometer (Spectrum 100). Raman spectra (RS) were obtained using a Nomadic^{TM} Raman 3-in-1 microscope with 532 nm lasers. UV-vis absorption spectra were recorded with a Hitachi UH5300 spectrometer, and transmission of UV-A radiation was measured according to the AS/NZS4399:1996 standard procedure. Electrical performances of TENG under different applied forces and frequencies were evaluated by a button/key durability life test machine (ZX-A03, Zhongxingda, Shenzhen) equipped with a high-speed self-

configuring digital indicator (Interface 9860). The open-circuit voltage, short-circuit current and short-circuit charge transfer were recorded by an electrometer (Keithley 6514, Tektronix). The output performance of the TENGs under different applied forces and frequencies has been evaluated by utilizing a keyboard life tester. Tensile/compression performance measurements were performed on a universal tensile testing machine (Instron 4411) equipped with a 5 kN load cell. The force signals can be monitored by DAQ system, and the electrical signal can be collected by oscilloscope or electrometer. The water contact angle was recorded using SDC-350 contact angle measurement equipment. The air permeability was measured using a KES Air Permeability Tester. Thermogravimetric analysis (TGA) was performed under a nitrogen atmosphere on a TGA/DSC Mettler-Toledo International Inc. The coefficient of Friction was investigated by the Rtec Tribometer Instrument. KEYENCE 3D Laser Scanning Microscope was employed to measure wear track, scratch, and depth and

produce 3D microscopic images. The simulation was conducted with COMSOL Multiphysics software. Inductance–capacitance–resistance (LCR) measurements were made with a Hioki IM 3536 (purchased from Linktronix; Switzerland). The tensile testing was completed on an Instron Electro Pulse E3000 or Zwick/Roell.

1.4 Research Significance

This perspective research is showing tremendous achievements in both fundamental understanding and technological improvements. The successful integration of various 2D materials into the design and fabrication of flexible TENGs has led to significant advancements in their energy harvesting capabilities, mechanical properties, and functional versatility. These innovative approaches have the potential to bridge the gap between advanced energy harvesting technologies and wearable platforms, paving the way for the development of next-generation self-powered and sustainable electronics. 2D materials are a class of materials with special structures and properties at the level

of a few atoms or molecules in thickness, which have attracted much attention in the fields of electronics, optics and energy due to their unique characteristic properties. 2D materials have a range of characteristic properties that favor electron transport and electrical conductivity due to their special structure and properties. These properties include atomic layer thickness, band gap modulation, surface activity, quantum effects and bending effects. By exploiting these properties, 2D materials with high electrical productivity can be designed and prepared for applications such as electronic devices, energy storage and sensors. This research emphasized common and economic 2D materials from fabrication to operation, achieved enhanced output through cost-effective and easy fabrication ways, broadened the application scope and multifunctionality, bridged other physical phenomena with triboelectrification, such as tribology test, and discussed the possible mechanisms. We have designed several TENGs that can harvest energy from the environment or humans with increased

performance owing to novel 2D materials and can be combined with other facilities for multifunctionality.

The research findings presented in this work contribute to the ongoing efforts in the field of flexible nanogenerators, offering novel material solutions and design strategies to enhance the performance and functionalities of these promising energy-harvesting devices. The insights gained from this study have important implications for the future of wearable power supply systems, enabling the seamless integration of energy harvesting capabilities into various textile-based platforms and applications. The research summarized in this work highlights the significant advancements in the development of flexible triboelectric nanogenerators through the strategic integration of novel two-dimensional materials. The enhanced electrical performance improved mechanical properties, and the versatile functionalities of these 2D material-based TENGs have paved the way for the next generation of self-powered and sustainable

electronics. The insights gained from this research contribute to the ongoing efforts in the field of flexible energy harvesting technologies, offering novel material solutions and design strategies to address the growing demand for portable and wearable power sources.

1.5 Outline of this Thesis

This thesis has made practice on systematic research from design, experiment, exploitation, and application of TENG. With a proper understanding of the research information, the following chapters of different works about TENG were attempted from materials, fabrication, devices, characterization, applications, analysis, and discussion correspondingly, to achieve the research aims and objectives, consisting of seven chapters listed as follows:

Chapter 1 briefly introduces the situation of renewable energy as a background for the development of triboelectric nanogenerators, then introduces the categories, characteristics, mechanisms, general research status, and problems of TENG. Then, the research objectives, research methodologies, research significance, and outlines used

in this work are presented.

Chapter 2 reviews the literature on the recent progress of related TENGs including electrospinning membranes, common dopants, and 2D materials in TENGs as well as the development history, working principles, and potential applications of TENGs. With a proper understanding of the research information, the following chapters of different works about TENG were taken correspondingly to achieve the research aims and objectives, involving materials, fabrication, devices, characterization, applications, analysis and discussion.

Chapter 3 innovatively introduced two species of novel 2D material TMCCs, Nb_2S_2C and Ta_2S_2C, as dopants into PDMS to fabricate TENG and exhibited enhanced electrical properties with top value of both at 3 wt. ‰. Moreover, Tribology Test revealed the Coefficient of Friction (COF) with the same material pairs as TENG.

Chapter 4 developed a PVA hydrogel TENG doped with 2D g-C_3N_4, which could act as both cost-effective flexible electrode and positive dielectric for TENG with different morphologies. Mechanical energy harvesting devices in different morphologies including discoid flake shape, tube shape, and spiral shape in single electrode mode or

contact separation mode have been designed, fabricated, and evaluated.

Chapter 5 utilized electrospinning membrane of PA_{66} to fabricate a multifunctional TENG and showed twice enhancement with g-C_3N_4 in electric performance. A comparison of triboelectric properties has also been made under UV light and dark environments, showing that charge transfer is very sensitive with doping g-C_3N_4. The doped electrospinning membrane composite was also made into a flag to scavenge natural wind energy.

Chapter 6 explored the influence of g-C_3N_4 hybrid dopants with PDMS, including Ag nanowire with g-C_3N_4, carbon nanotube with g-C_3N_4, and MXene with g-C_3N_4. We also designed a dish and an insole with multiple TENGs for pressure sensing and multichannel data acquisition, as well as an intelligent wireless system with Bluetooth module and mobile software.

Chapter 7 summarized the whole research study, pointed out the current limitations and presented the future work of TENGs with 2D materials, as well as structure development and applications.

CHAPTER 2: Literature Review

2.1 Fundamentals of TENG

2.1.1 History

Energy is a crucial resource for the quality of our lives. The energy crisis, as well as climate change mainly originated in fossil fuel burning, has been causing a tremendous amount of research effort to invent sustainable energy harvest production, recycling, storage, and conversion systems. However, fossil fuels are on the way to dying out if we continue consuming them in this way. In the meantime, mechanical motion energy associated with human beings, and the ambient environment is abundant.

In the new 20th century, nanogenerators have been invented to capture kinetic energy from the movement of biomechanical or human beings, as well as movement in nature, such as wind, water flow, blue energy in ocean tidal energy, etc. In addition, nanogenerators acting as flexible, sustainable, and portable energy source power supply

replacing the traditional chemical batteries, can be combined with smart textiles and wearable electronics and meet the demands of unlimited lifetime, persistent recharge, convenience, and lightness, etc.

Mechanical energy harvesting is one of the most essential approaches to converting mechanical energy into electricity for better utilization in mankind's society. Faraday invented the Electromagnetic Generator (EMG) in 1831 based on the fundamental principle of the electromagnetic induction phenomenon, which has been the primary and fundamental power generation even to date. Maxwell's equations in 1861 combined electromagnetism and displacement current as theoretical principles for EMG. When a conductor is stuck with an external electric circuit that moves across the magnetic induction lines, the induced electrodynamic potential is generated across the conductor stick: $E = B*l*v$, where B is the magnetic flux density, l is the length of the conductor stick, and v is the velocity of the conductor stick cutting the magnetic induction lines.

It is crucial to extract energy from sustainable and renewable sources, and among the many technologies for doing so, nanogenerators have garnered a lot of interest recently. PENG, pyroelectric and thermoelectric nanogenerators for energy harvesting were successively invented. TENG can scavenge mechanical energy with a theoretical basis on the coupled effect of contact electrification and electrostatic induction due to Maxwell displacement electricity. Extensive research and developments on TENG have been carried out as a burgeoning focus[1] for energy harvesting from low-frequency and low-amplitude[42] mechanical energy.

The coupling of triboelectrification and electrostatic induction acts as the fundamental mechanism of triboelectric nanogenerators[42], which can be classified into four operation modes: vertical contact-separation mode, lateral-sliding mode, single electrode mode, and freestanding triboelectric-layer mode. The vertical contact separation utilized relative motion perpendicular to the interface, while the sliding

mode took advantage of the relative displacement in the direction parallel to the interface[1]. The single-electrode mode utilizes the ground or human body as the reference electrode making it versatile in energy harvesting, and the freestanding mode is exploited using a pair of electrodes with electric output from asymmetric charge distribution[2]. TENG's great potential application and potency scenario have also been enhanced by hybridization of its different modes[3] or combination with other energy conversion devices like PENGs, pyroelectric nanogenerators, moisture electric generators, EMGs, etc.

TENG is one of the most effective ways of converting all forms of mechanical energy into the living environment. Rapid advancements in stretchable and multifunctional electronics imposed a challenge on corresponding power devices. Integrating an energy harvesting TENG with an energy storage supercapacitor improves uncontrollable fluctuation or instability in outputs to drive some peripheral electronic devices into one

functional textile material, which is qualified with complex mechanical deformations, wearable devices, or electrochemical power sources for sustainability.

2.1.2 Three main factors affecting the output efficiency of TENGs

(1) Electronegativity difference between the two tribo-layer materials

From the basic principle of the triboelectric nanogenerator, it can be inferred that for a relatively high-power output efficiency, the interacting friction materials must first produce sufficient electron exchange; that is, the electronegativity difference between the two materials should be as large as possible. The triboelectric series in Figure 2.1 is a list that ranks various materials according to their tendency to gain (negative) or lose electrons (positive) in the contact charging and sliding charging process. The further the two materials are located on the triboelectric series, the greater the electrical energy of the triboelectric nanogenerator can prepare. Although the mechanism of the triboelectrification effect is not fully understood, the friction sequences of different

materials have been widely reported. Therefore, materials at both ends of the friction sequence are used more frequently, such as PTFE, PDMS, PVDF, nylon, etc. Materials that possess a strong triboelectrification effect tend to be less conductive or insulating[43]. The materials that constitute the triboelectric nanogenerator are divided into friction materials and electrode materials. Almost all materials from metal to polymer, from silk to wood, exhibit triboelectrification effect. All these materials can be candidates for TENG fabrication. The further away two materials are from each other on the series, the greater the charges can be transferred. This new energy harvesting technology has the advantages of low cost in manufacturing and fabrication, excellent robustness, reliability, environmental friendliness, and so on.

(2) Surface topography of tribo-layer material

The surface morphology of the friction material is also an important factor affecting the output power of the triboelectric nanogenerator, so constructing a coarse surface by

nanotechnology is an effective way to amplify the effective contact area and enhance the triboelectric charge density. Modifying nanowires/rod arrays on the surface of the material can greatly improve the performance of the device, but there are also shortcomings such as reduction of the flexibility or ductility and the interface problems with the substrate can lead to poor wear resistance or stability of the device. Another polymer nanowire/rod array method achieves the purpose of removing part of the etched material using plasma. When this method is used to handle the surface of the polymer film, the interface problem between the nanowire/rod array is avoided, and the wear resistance of the device is greatly improved. This flexible nanowire array can be bent to adapt to the surface morphology of the opposite material, making the contact between the two friction surfaces closer, thus increasing the effective friction area and then the output power. Inductively coupled plasma etching method with anisotropy, high etching accuracy, good repetition, uniformity, and less pollution has been widely

used in various triboelectric nanogenerator devices.

The preparation of multi-stage micro-nano structures is also introduced into the preparation of triboelectric nanogenerators to obtain rough surfaces with micrometer or nanopattern arrays, greatly improving the output efficiency of triboelectric nanogenerators. Nanofiber structure is also a method to improve the output efficiency of the triboelectric nanogenerator[7]. For example, electrospinning is the jet spinning of a polymer solution or melts in a strong electric field, where the droplets at the needle change from spherical to conical and extend from the conical tip, producing a polymer filament of nanoscale diameter. Besides the choice of the materials in the triboelectric series, the surfaces of the materials can be functionalized chemically by introducing various molecules, nanotubes, nanostructures, nanowires, or nanoparticles, to enhance the local contact characteristics, surface potential and triboelectrification effect. Contact materials can be made of composites, such as embedding nanoparticles in polymer

matrix by changing the surface electrification as well as the permittivity of the materials in order to be effective for electrostatic induction. Generally, materials for electrodes usually come from three main types, i.e. transition metal materials, carbon-based materials or conductive polymers.

(3) Structure of a triboelectric nanogenerator

In terms of physical processes, the conversion of energy can generally be divided into three steps: the generation of electric charges, the separation of electric charges, and the flow of electric charges. For the triboelectric nanogenerator, the two points mentioned above mainly affect the generation process of electric charge; nevertheless, the separation of electric charge is also very important. Most kinds of triboelectric nanogenerators adopt plane structures. Under the action of external force, the positive and negative materials can only perform a small relative movement, which is unfavorable for the generation and separation of electric charges. Therefore, designing

a suitable structure of triboelectric nanogenerators is an effective way to improve output performance, as well as to adapt to different application scenarios and multi-functional self-driving systems. With the development of micro/nanotechnology, a lot of studies introduce different micron/nanostructures into the structural design of tribo-layer materials to increase power output. Growing nanowires or nanorod arrays on the material surface can greatly improve the specific surface area, so it is widely used in various fields of catalysis, sensing, energy storage, energy conversion, and so on. TENGs demonstrated huge applications as self-powered systems by harvesting biomechanical or ambient energy, as well as power sources to drive electrochemical reactions.

Table 1 Triboelectric series of materials and their triboelectric charge density (TECD)

Materials	Abbr.	Average TECD ($\mu C\ m^{-2}$)	STDEV	α
Chemical-Resistant Viton® Fluoroelastomer Rubber		−148.20	2.63	−1.31
Acetal		−143.33	2.48	−1.27
Flame-retardant garolite		−142.76	1.49	−1.26
Garolite G-10		−139.89	1.31	−1.24
Clear cellulose		−133.30	2.28	−1.18
Clear polyvinyl chloride	PVC	−117.53	1.31	−1.04
Polytetrafluoroethylene	PTFE	−113.06	1.14	−1.00
Abrasion-resistant polyurethane rubber		−109.22	0.86	−0.97
Acrylonitrile butadiene styrene	ABS	−108.07	0.50	−0.96
Clear polycarbonate (Glossy)	PC	−104.63	1.79	−0.93
Polystyrene	PS	−103.48	2.48	−0.92
Ultem polyetherimide	PEI	−102.91	2.16	−0.91
Polydimethylsiloxane*	PDMS	−102.05	2.16	−0.90
Polyester fabric (Plain)		−101.48	1.49	−0.90
Easy-to-machine electrical-insulating garolite		−100.33	1.79	−0.89
Food-grade high-temperature silicone rubber		−94.03	0.99	−0.83
Polyimide film	Kapton	−92.88	2.58	−0.82
DuraLar polyester film	PET	−89.44	0.86	−0.79
Polyvinylidene fluoride	PVDF	−87.35	2.06	−0.77
Polyetheretherketone	PEEK	−76.25	1.99	−0.67
Polyethylene	PE	−71.20	1.71	−0.63
High-temperature silicone rubber		−69.95	0.50	−0.62
Wear-resistant garolite		−68.51	1.99	−0.61
Low-density polyethylene	LDPE	−67.94	1.49	−0.60
High impact polystyrene		−67.37	1.79	−0.60
High-density polyethylene	HDPE	−59.91	1.79	−0.53
Weather-resistant EPDM rubber		−53.61	0.99	−0.47
Leather strip (Smooth)		−52.75	1.31	−0.47
Oil-filled cast nylon 6		−49.59	0.99	−0.44
Clear cast acrylic	PMMA	−48.73	1.31	−0.43
Silicone		−47.30	1.49	−0.42
Abrasion-resistant SBR rubber		−40.13	1.31	−0.35
Flexible leather strip (Smooth)		−34.40	0.86	−0.30
Noryl polyphenyl ether		−31.82	0.86	−0.28
Poly(phenylene Sulfide)	PPS	−31.82	0.86	−0.28
Pigskin (Smooth)		−30.10	0.86	−0.27
Polypropylene	PP	−27.23	1.31	−0.24
Slippery nylon 66		−26.09	0.50	−0.23
Weather- and chemical-resistant santoprene rubber		−25.23	0.50	−0.22
Chemical- and steam-resistant aflas rubber		−22.65	1.31	−0.20
Polysulfone		−18.92	0.86	−0.17
Cast nylon 6		−18.35	0.99	−0.16
Copy paper		−18.35	0.50	−0.16
Chemical-resistant and low-temperature fluorosilicone rubber		−18.06	0.86	−0.16
Delrin® Acetal Resin		−14.91	0.50	−0.13
Wood (marine-grade plywood)		−14.05	0.99	−0.12
Wear-resistant slippery garolite		−11.47	0.50	−0.10
Super-stretchable and abrasion-resistant natural rubber		−10.61	0.50	−0.09
Oil-resistant buna-N rubber		2.49	0.23	0.02
Food-grade oil-resistant buna-N/vinyl rubber		2.95	0.13	0.03

Note: STDEV refers to the standard deviation. The α refers to the measured triboelectric charge density of tested materials over the absolute value of the measured triboelectric charge density of the reference material. The material marked with an asterisk "*" means it has strong adhesion with mercury, a small drop of mercury is observed when it is separated with mercury. The measured TECD value may be a bit lower than its real value. Source data are provided as a Source Data file.

Figure 2.1 Triboelectric series[41] of materials

2.1.3 Working mechanism and Operation mode of TENG

In 2012, the world's first TENG was reported, which is a triboelectrification-based flexible thin-film generator with the combination of friction electric power and

electrostatic induction. After the further reasonable design of the device structure, the ancient phenomenon of friction electric power shows new applicable value and potential. Under the action of external forces, the device produces mechanical deformation, leading to mutual friction between the two polymer films, resulting in charge separation and potential difference. Two metal electrode plates serve as the power output of the generator, and inductive charges can be generated on the surface via electrostatic induction. The induced charge is formed by the external circuit driven by the potential difference. The power output mechanism of the triboelectric nanogenerator can be illustrated by the coupling effect of friction electric effect and electrostatic induction effect[44].

When an external force (switching, bending, sliding, colliding, rubbing, etc.) is applied to the triboelectric nanogenerator, the two polymers that were originally in close contact will move relative to each other at a small angle and separate slightly. Charges of

opposite signs form a macroscopic dipole layer at the interface; such a dipole layer will cause a potential difference between the two plate electrodes. And because the polymer is an insulator, the charge on its surface can remain for a long time without being conducted away or neutralized. At this time, the original neutral electrode will generate free electrons by electrostatic induction, and its charge will counteract the generated triboelectric potential through the flow of the external circuit, thereby generating a current and reaching a relatively balanced status. When the two polymer surfaces are in close contact with the original state, the original heterogeneous charges will also be neutralized (Figure 2.2).

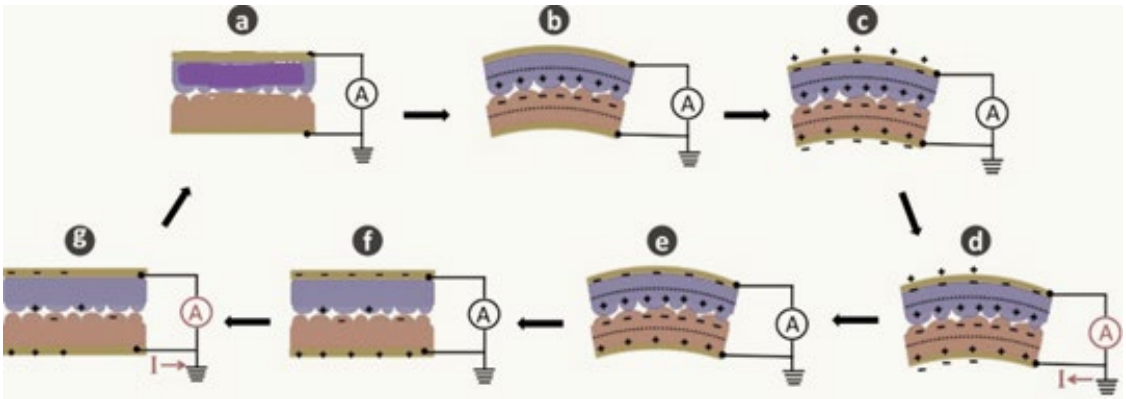

Figure 2.2 Detailed description of the entire power generation process (a) The initial

state of the device. (b) Electrostatic charges with opposite signs are generated and distributed on the two internal surfaces of the polymer films through a friction process. (c) Two neutral metal electrodes are charged via electrostatic induction. (d) The electron's flow across the external load generates a voltage/current peak. (e) A temporary potential equilibrium forms in the entire device. (f) Most of the electrostatic charges on the internal surfaces are neutralized during the releasing process. (g) Electrons flow back via the external circuit until the potential equilibrium forms between the two metal electrodes[45].

Four basic modes of TENGs have been established and classified based on divergent configurations and compositions of the electrodes and dielectrics while the electrostatic induction process generates electricity, including vertical contact-separation mode, lateral sliding mode, single electrode mode, and free-standing mode (Figure 2.3).

(1) Vertical contact-separation mode

Vertical contact-separation mode is the most basic mode of TENG with a simple design. In this mode, two different triboelectric layers confront each other in a stacked state. When the external force is removed and the organic film separates from each other, the charge at the interface of the two films will produce a potential difference, producing a positive current pulse. When the external force is applied to the device again, the potential difference in the opposite direction drives the flow, generating a negative current pulse. Therefore, if the device is constantly contacted or separated by external forces, then a continuous alternating current electrical signal is formed. The performance of contact separation mode TENGs is very efficient for vibrations and cyclic pressures as short-range periodic motions in kinetic energy harnesses.

(2) Lateral sliding mode

The device structure of the linear sliding mode is also simple and is similar to the vertical contact-separation mode. The layers separate from sliding in the in-plane

direction, where the sliding process can be achieved from planar motions, disc rotation, cylindrical rotation, etc. This kind of configuration has a large energy efficiency but the abrasion between triboelectric layers limited the application of this mode of TENG.

(3) Single-electrode mode

The single-electrode triboelectric generator does not have only one electrode but assumes the role of the other electrode by one original existing electrode such as the human body, ground, etc. The output of electrical energy is realized through the transfer of charges between the electrodes of the generator itself and the ground electrode.

(4) Free-standing triboelectric-layer mode

Freestanding mode TENG is an extension of the first two working modes. When the negative electrode and the positive electrode are not charged originally, all the charges are caused by the triboelectrification of the physical contact between the two, so the negative charge on the negative electrode should theoretically be equal to that on the

positive electrode. When the negative electrode and the first positive electrode on the left just cover each other, all the positive charges will be attracted to the upper surface of the left electrode. When the negative electrode slides toward the second positive electrode, the positive charge in the loop will flow, which is the first half-cycle in the process of electric energy generation. When the negative electrode reaches the position where it just overlaps with the right electrode, all the positive charges remain on the right electrode. Then, when the negative electrode slides back to the left electrode, the positive charge will flow from the right electrode to the left electrode, forming a current in the loop that is opposite to the direction of the first half cycle. This is the second half cycle of the electrical energy generation process.

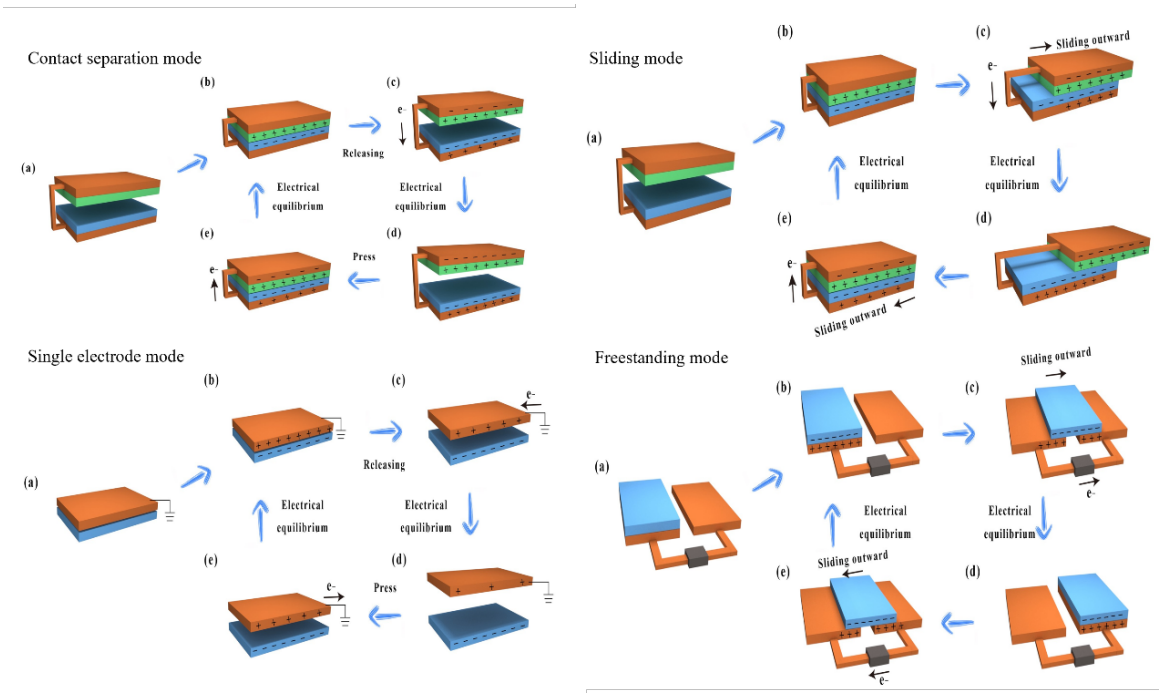

Figure 2.3 Mechanism of four working modes of TENG

2.2 Electrospinning TENG

Common techniques to design and fabricate micro or nano architectures include lithography[46], electrospinning, spin coating, doctor-blading, 3D printing[47], etc. and electrospinning[48] is versatile and cost-effective among these techniques. Operating conditions and solution parameters extremely affect the morphology[25] of the resulting membranes. Electrospinning as a simple and effective new processing technology that

can produce nanofibers has a wide range of applications for the development of nanotechnology. This membrane fabrication technique uses the electric potential difference to force charged polymer solutions to melt up to fiber diameters in which highly porous nanofibrous structures can be approached from a variety of polymers[49]. Electrospinning technology can effectively increase the surface area of fabricated membranes. The morphology and properties of electrospinning nanofiber are greatly influenced by factors such as solution concentration, viscosity, flow rate, applied voltage, needle size, and distance between needle and holder[50]. The performance of electrospinning nanofibrous membranes is closely related to features like pore-size distribution, hydrophilicity[51] or hydrophobicity[52], mechanical strength, and stability[53]. Electrospinning has already been adopted as a suitable method in the field of TENGs for fabricating diverse nanofibrous surface[54] microstructures from economical materials, such as electronegative materials including polyvinylidene fluoride

(PVDF)[54-57], polytetrafluoroethylene (PTFE)[50, 58], polyethylene terephthalate (PET)[59], and most commonly Polydimethylsiloxane[60-63](PDMS) whose pristine phase is liquid under normal circumstances, as well as electropositive materials including Al, Cu, acrylics[64], thermoplastic polyurethane (TPU)[65], cellulose[66-70], silk[71-72], polyvinyl alcohol (PVA)[73], and nylon/polyamide)[74] as strong electron donor polymer in common life. The performance of electrospinning nanofibrous membranes is closely related to features like pore-size distribution, hydrophilicity[51] or hydrophobicity[52], mechanical strength, and stability[53]. One is to design and fabricate micro or nanoarchitecture using ion etching process[75], such as photolithography[61], nanoimprinting lithography[76], laser interference[77], porous modification[78], etc. In comparison to dense films or fabricated textiles with micron-sized pores in triboelectric nanogenerators, electrospinning is a versatile, accessible, simple, and cost-effective method of producing ultrathin fibers with sufficient length, surface area, and hierarchically intrinsically nanoscale porosity.

Another strategy is to increase the permittivity of friction composites by doping specific elements into pure triboelectric layers, which includes miscellaneous carbon nanotubes[79], liquid metals[25], graphene or graphene oxide[80], metal nanowire or nanoparticle[81], ferroelectric materials[82] like $BaTiO_3$, electronegative halogen[83], etc. As shown in Figure 2.4a, common PA and PVDF can be fabricated into membrane coating layers by versatile electrospinning and made into core-shell yarns and then scalable woven into freestanding textile TENGs[46]. Tips in the electrospinning process could influence the nanostructure significantly, so different kinds of nozzle systems, including single nozzle, conjugated nozzle, and multi nozzles, as well as plate collector and drum collector, have been experimented with, as shown in Figure 2.4b, where TENG adopted PI and PVDF as electrospinning solutions[56]. PTFE has significant electronegativity but is insoluble in most solvents. Nanofibrous PTFE was fabricated by electrospinning with a suspension of PTFE particles in dilute polyethylene oxide

(PEO) aqueous solution, then thermally treated at 350 °C to remove the PEO component from the electrospun PTFE-PEO nanofibers. Sandwiching the PTFE nanofibrous membrane into two pieces of conducting carbon clothes nanogenerator can be directly used as a wearable self-powered sensor[58], as shown in Figure 2.4c. Electrospinning can also contribute to homogeneous doping for material modification. Electrospinning promoted the formation of highly polar crystalline β-phase of PVDF and δ-phase of nylon, resulting in cooperative and mutual alignment of polymer chains with ZnO NWs[55] (Figure 2.4d). Liquid metal (LM) particles with different concentrations were incorporated into polyacrylonitrile (PAN) electrospinning nanofiber by electrospinning as a positive tribo-layer. TENGs adopting 1.5 wt. % LM concentration PAN and PTFE achieved maximum output twice as high as compared to those of pure PAN but deteriorated drastically over 2.5 wt. % which generated spheroid and spindle particles[25] (Figure 2.4e). Liquid metal Galinstan nanodroplets were also

electrospun into PVDF-co-hexafluoropropylene (PVDFHFP) nanofibers with outstanding performance attributed to multiple factors, including the improved surface potential, capacitance, charge trapping capability, and secondary polarization[54] (Figure 2.4f). Besides material modification, the electrospinning technique can also be utilized for TENG's structure innovation[24]. Electrospinning ordered polymer nanofibers can result in an anisotropic triboelectric nanogenerator with superior tensile and mechanical strength over disordered electrospinning TENG. When not in use, the nanogenerator can be turned 90 degrees to reduce static charge accumulation and circuit burnout, giving a straightforward technique for mitigating electrostatic discharge (EDS) in a wearable environment[84] (Figure 2.4g). Fully biodegradable triboelectric nanogenerator (BD-TENG), optimizing gelatin and electrospun polylactic acid (PLA) nanofiber membrane could be degraded completely into the water in about 40 days with no adverse effect on the environment or human body[85] (Figure 2.4h).

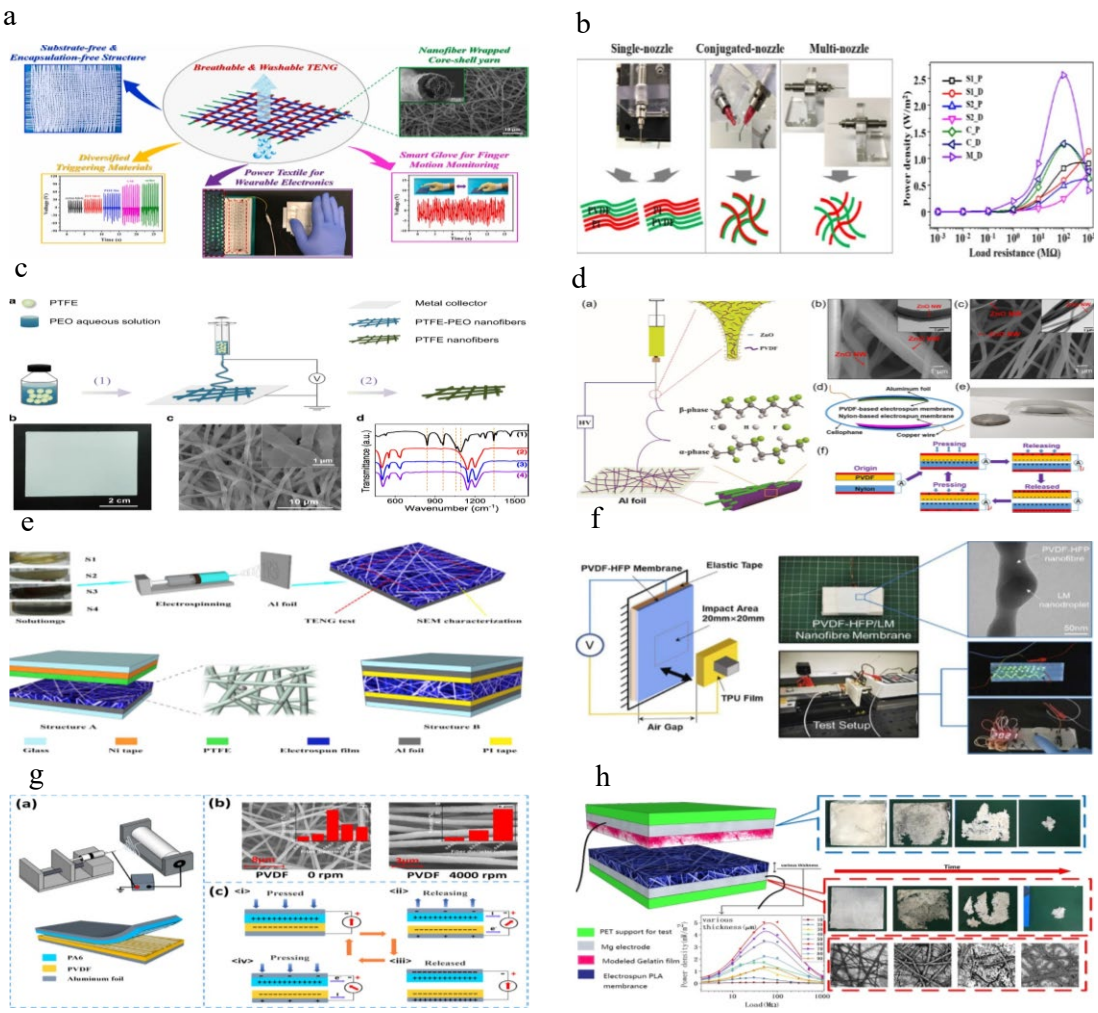

Figure 2.4 Several Electrospinning TENGs (a) Breathable, |Washable and Wearable Woven-structured Triboelectric Nanogenerators Utilizing Electrospun Nanofibers for Biomechanical Energy Harvesting and Self-powered Sensing[46] (b) Characterization of PI/PVDF-TrFE Composite Nanofiber-Based Triboelectric Nanogenerators Depending on the Type of the Electrospinning System[56] (c) Electrospun Polytetrafluoroethylene Nanofibrous Membrane for High Performance Self-Powered Sensors[58] (d) Flexible

PVDF/Nylon-11 Electrospun Fibrous Membranes with Aligned ZnO Nanowires as Potential Triboelectric Nanogenerators[55] (e) Effects of Liquid Metal Particles on Performance of Triboelectric Nanogenerator with Electrospun Polyacrylonitrile Fiber Films[25] (f) Electrospun liquid metal/PVDF-HFP Nanofiber Membranes with Exceptional Triboelectric Performance[54] (g) Anisotropic Triboelectric Nanogenerator Based on Ordered Electrospinning[84] (h) Fully Biodegradable Triboelectric Nanogenerators Based on Electrospun Polylactic Acid and Nanostructured Gelatin Films[85].

As discussed before, features such as rough surface, permeable structure, flexible texture, specific large surface area and cost-benefit fabrication process can greatly benefit TENG's fabrication and performance, which promotes nanofiber membrane prepared by electrospinning technique being widely used in developing triboelectric

nanogenerators, especially fabric-based flexible TENGs. In addition, functional materials could be easily mixed and doped into polymer solutions during the process of electrospinning. Owing to the porous micro and nano structures and large specific area, nanofiber network structures might also endow TENG devices with multifunctions such as removal[86], absorption[87], sterilization[88], wastewater filtering[59], biodegradability[69], etc.

2.3 Common dopants in the dielectric materials of TENG

The modification or functionalization of triboelectric materials is of great importance for improving the triboelectric nanogenerator's triboelectric performance[14]. Functionalization of TENG materials was one of the most effective methods for improving friction materials' triboelectric performance[10]. Generally, there is an enhanced effect at low concentrations in both positive and negative dielectrics for metal

substances, such as liquid metal or metal-organic framework (MOF)[89]. When added to the negative dielectric, the effect of halogens is obvious because of halogens' strong electron affinity, especially for some liquid substrates[10]. Ferromagnetic materials can be magnetized to saturation under the action of a very small magnetic field[90]. This type of magnetism is called ferromagnetism. Ferroelectric materials refer to a class of materials with ferroelectric effect, which has become one of the most popular research topics in the fields of condensed matter physics and solid-state electronics[82]. Many electrooptic crystals and piezoelectric materials are ferroelectric crystals. Ferroelectric crystals are of great significance both technically and theoretically. Because the internal microscopic electric field and the electric field generated by the positive and negative materials are coupled with each other[91], the doping of ferroelectric materials such as $KTiOPO_4$(KTP), $KNaC_4H_4O_6$, $BaTiO_3$, $KNbO_3$, $LiNbO_3$ within an appropriate concentration can generally greatly improve the power generation efficiency of the

nanogenerator[68-69, 92-97]. Similarly, ferromagnetic substances can also accelerate the coupling of electric fields, both as electrodes or dielectrics such as Fe, Co, Ni, or their compounds[98]. Light is also a kind of electromagnetic wave. Similarly, the light field can have an impact on the electricity generation performance of the nanogenerator, especially when it is doped with light-sensitive materials. The situation of semiconductor[99] doping is more complicated. Elements that easily lose electrons (such as N) doped into positive dielectric and elements that easily seize electrons (such as Si) into negative dielectric, generally have an enhancement effect but are not particularly prominent, and will also produce multifunction[100-102].

2.4 Two-dimensional 2D materials for enhancement of TENG output

Single-layer materials[103], or 2D nanomaterials, are generally categorized as either 2D allotropes or compounds with crystalline solids consisting of a single layer of atoms. 2D materials possess a large surface area, implying that within a limited volume, a more

active surface is available to increase charge separation. Additionally, some 2D materials exhibit excellent conductivity, aiding in the efficient transport of charges and reducing resistive losses[104]. Certain 2D materials have appropriate electronic band structures conducive to charge separation under the influence of external forces[105]. By doping or tuning 2D materials, it is possible to adjust the Fermi level, thereby altering the transport properties of electrons[106]. This tuning can optimize charge separation[40] and transport, contributing to the improved efficiency of TENG. Moreover, the formation of heterojunctions by combining different two-dimensional materials can induce additional charge separation effects[107]. Possible explanations for the mechanism of how they enhance electrical generation are listed as follows: (1) Atomic Layer Thickness: 2D materials are only a few atomic or molecular layers thick, which allows for less restricted movement of electrons within the material, reducing scattering and energy loss for higher electron mobility. (2) Higher mobility: electrons can flow more

easily and increase conductivity. (3) Bandgap modulation: TMDs have a tunable electronic bandgap. The size of the electronic bandgap of a 2D material can be altered by mechanical strain, external electric/magnetic fields, or chemical modification. This makes it possible to tailor the conductivity of the material to the needs of the application such as semiconductor devices. (4) Surface Activity: Most of the atoms of 2D materials are located on the surface, which gives them a high surface area that helps to improve the material's interaction with its surroundings, which is important for certain sensor applications and catalysts[108]. (5) Quantum effects: Since the thickness of 2D materials is close to nanoscale, quantum effects can be observed in these materials. For example, quantum dots, which are nanoscale energy levels formed in 2D materials, can affect the energy band structure and conductive properties of electrons[109]. (6) Bending effect: By curving or striking 2D material, additional electron energy levels could be introduced to affect electron transport and electrical conductivity, which is perfect for energy

harvesting, storage, and sensors in PENG and TENG[110].

Noteworthy, various 2D[30] structures have been discovered, including graphene[111], graphene oxide (GO)[80, 111-117], MXene[118], MoS_2[119], WS_2, transition metal dichalcogenides (TMDs)[120], MXenes[102, 118, 121], black phosphorus (BP), layered metal-organic frameworks (MOFs), layered covalent-organic frameworks (COFs), hexagonal boron nitride (h-BN), layered metals and g-C_3N_4, etc. Graphitic carbon nitride (g-C_3N_4) possesses distinctive features and has numerous applications in hydrogen evolution[99], photocatalytic degradation, gas sensor[122], antibacterial structure[123], and as a microwave absorber[124]. 2D materials have attracted significant research attention for essential characteristics such as high conductivity, flexibility, transparency, and a high surface-to-volume ratio, which facilitate the creation of charge storage sites that are more deeply embedded, allowing for the scavenging of the triboelectric charges accumulated at the surface of the triboelectric layer materials[125]. In 2018, the triboelectric charging

behaviors of various 2D nanomaterials, including MoS_2, $MoSe_2$, WS_2, WSe_2, graphene, and graphene oxide were investigated and measured through TENGs for relative charging polarity against representative materials, with explanations provided at the molecular level[30]. 2D materials have a commonality in their electrical production properties due to their specificity in electron transport, representing a breakthrough in our research on performance enhancement and the commonality of two-dimensional materials. 2D materials, characterized by their special structures and properties at the level of a few atoms or molecules in thickness, have been widely studied in recent years, including graphene/graphene oxide[30], transition metal dichalcogenides, MXene[32], carbon nitride[123], transition metal carbo-chalcogenide[33]. These materials have garnered significant attention in the fields of electronics, optics, and energy due to their unique properties[34]. The working principle of improving electrical performance depends on the type of device and the specific desired outcome. Generally, electrical performance can

be improved by reducing energy losses, increasing energy storage capacity, enhancing energy conversion efficiency, or boosting processing speed.

MXene is a specific type of 2D material that belongs to the family of transition metal carbides/nitrides[35]. Discovered in 2011, MXene is characterized by the general formula $Mn_{+1}XnTx$, where M represents a transition metal, X represents carbon and/or nitrogen, and Tx represents surface termination groups, such as hydroxyl or oxygen[126]. MXenes are known for their excellent electrical conductivity, high mechanical strength, and good chemical stability, making them promising candidates for applications in energy storage, catalysis, electronics, and sensors. TMDs, mostly commonly MoS_2 and WS_2, exhibit varying electronic band structures depending on their polymorphic structures[38]. The 2H-phase TMDs, with trigonal prismatic metal coordination and hexagonal symmetry, display semiconducting properties with a band gap of ~1.8 eV (monolayer 2H-MoS_2)[37]. In contrast, 1T- or 1T′-phase TMDs, prepared via chemical-intercalated

exfoliation or colloidal synthesis, possess octahedral metal coordination with tetragonal symmetry and are metallic or semi-metallic. Monolayer 2D TMDs possess unique fundamental properties that distinguish them from their bulk counterparts, making them suitable for broader green energy applications. This results from monolayer semiconductor TMDs with a direct band gap a high current on-off ratio for field-effect transistors. Transition metal carbo-chalcogenides (TMCCs) can be considered an atomic combination of transition metal carbides (MXenes) and transition metal dichalcogenides (TMDs). The layered transition metal carbo-chalcogenide Ta_2S_2C was synthesized first in the early 1970s by Beckmann, and later, in the 1990s, Boller and Hiebl successfully synthesized the metastable phase Nb_2S_2C, which shares a similar structure as Ta_2S_2C, through a topochemical reaction. The 2D version of TMCCs was first successfully obtained from multilayered Nb_2S_2C and Ta_2S_2C through electrochemical lithiation and sonication by Majed et al. and it was demonstrated that

the delaminated Nb_2S_2C outperformed its multilayered precursor material as an electrode material for Li-ion batteries[33]. Figure 2.5 listed some of the TENGs with 2D material published in recent years.

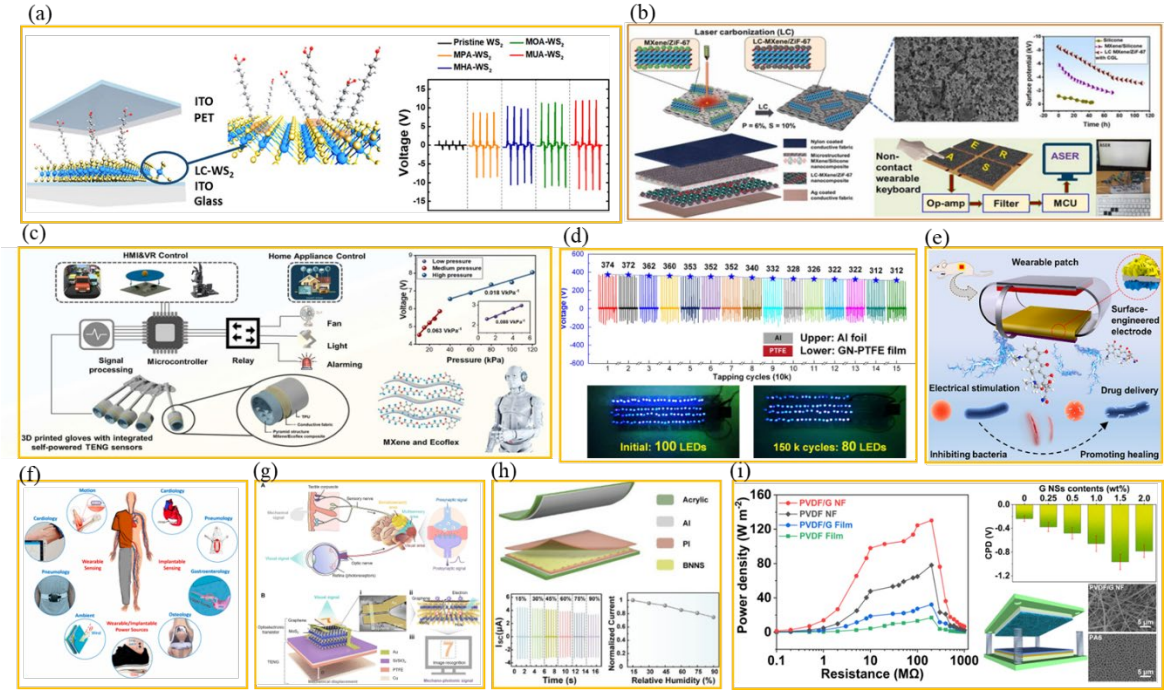

Figure 2.5 TENGs with 2D materials (a) Enhanced Triboelectric Nanogenerator Based on Tungsten Disulfide via Thiolated Ligand Conjugation.[37] (b) Laser-carbonized MXene/ZiF-67 Nanocomposite as an Intermediate Layer for Boosting the Output Performance of Fabric-based Triboelectric Nanogenerator.[127] (c) 3D Printed Smart Glove with Pyramidal MXene/Ecoflex Composite-Based Toroidal Triboelectric

Nanogenerators for Wearable Human-Machine Interaction Applications.[128] (d) Graphene Nanosheets Enhanced Triboelectric Output Performances of PTFE Films.[129] (e) Advanced Triboelectric Nanogenerator-driven Drug Delivery Systems for Targeted Therapies. [130] (f) Advances in Triboelectric Nanogenerators for Biomedical Sensing.[131] (g) Bioinspired Mechano-photonic Artificial Synapse Based on Graphene/MoS_2 Heterostructure.[132] (h) Triboelectric Nanogenerator Based on Polyimide/Boron Nitride Nanosheets/Polyimide Nanocomposite Film with Enhanced Electrical Performance.[133] (i) High-performance Triboelectric Nanogenerator Based on Electrospun PVDF-Graphene Nanosheet Composite Nanofibers for Energy Harvesting.[134]

2.5 Interface and Structure of TENG

Many attempts have been introduced to improve energy-producing and conversation efficiency, mainly from two approaches--innovative structure and materials, such as

increasing effective areas, producing micro/nanostructured interface, covering functional materials, new synthesis or doping into existing materials to increase dielectric constant. Triboelectric nanogenerators can also be defined into several types according to the interface phase of the positive dielectric and negative dielectric, such as solid-solid phase TENG, liquid-solid phase TENG, etc. Almost all the materials are in solid phase at the beginning because the solid phase material is common and easy to fabricate. TENGs with solid-solid contact[135] where the abrasion or friction heat generated by two solid surfaces[136] results in heat generation, dissipation, and physical deterioration, which significantly lowers the energy conversion efficiency[57, 135, 137-138] and durability of the devices[139]. In this regard, liquid-solid interface TENGs have raised people's attention[51], owning the advantage of better ductility, less abrasion, closer contact, etc. TENGs based on liquid-solid contact electrification can harvest kinetic energy from columbic scattering and photon coupling[140] with relatively high output

power.

In 2014, Guang Zhu's group from Chinese Academy of Sciences firstly invented the water liquid-solid TENG and published "Harvesting Water Wave Energy by Asymmetric Screening of Electrostatic Charges on a Nanostructured Hydrophobic Thin-Film Surface"[51], where liquid-solid electrification enabled generator made of fluorinated ethylene propylene (FEP) thin film to develop a single component energy converter. Feasible technology integrated an array of units on a single substrate to boost the electric output and demonstrate energy harvesting from ambient water waves and water drops for directly powering electronics[51], as shown in Figure 2.6a. Besides the frequently encountered solid-solid interface and liquid-solid interface TENG utilizing water as one dielectric, some scarce phases, such as liquid-liquid interface TENG, and liquid-gas interface TENG have also been demonstrated for some specific applications. For example, in "Self-Powered Triboelectric Micro Liquid/Gas Flow Sensor for

Microfluidics" from Chongqing University, a self-powered triboelectric microfluidic sensor is proposed by utilizing the signals produced from the droplet bubble via capillary and triboelectrification effects on the liquid-solid interface and liquid gas flow detection[136], where the alternating current (AC) can be converted into direct current (DC) by rectifier bridge or PN junction and the output signal of the sensor can be systematically measured, giving potential for the self-powered micro analysis system (Figure 2.6b). As shown in Figure 2.6c, a networked integrated triboelectric nanogenerator (NI-TENG) with PN junctions having an arrayed networking structure can accommodate diverse water wave motions and generate stable electric output regardless of water wave randomness, which is similar in real circumstances where water waves are highly variable and unpredictable[81]. Stretchable liquid-solid contact electrification-based nanogenerator (S-LSNG) enables water wave energy harvesting and subtle motion monitoring in water by an in-situ charged nanocomposite membrane,

which has excellent stretchability and high output performance (Figure 2.6d).

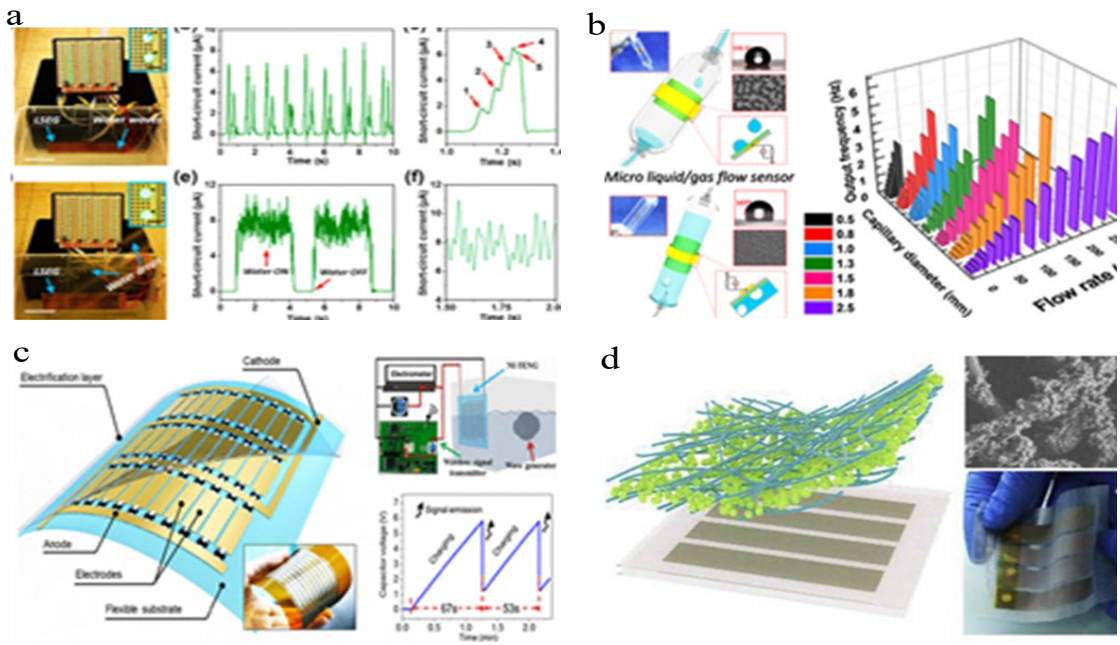

Figure 2.6 Liquid-solid interface TENGs with rectifier (a) Harvesting Water Wave Energy by Asymmetric Screening of Electrostatic Charges on a Nanostructured Hydrophobic Thin-Film Surface[51]. (b) Self-Powered Triboelectric Micro Liquid/Gas Flow Sensor for Microfluidics[136]. (c) Highly Adaptive Solid−Liquid Interfacing Triboelectric Nanogenerator for Harvesting Diverse Water Wave Energy[81]. (d) Stretchable Shape-adaptive Liquid-solid Interface Nanogenerator Enabled by In-situ Charged Nanocomposite Membrane[141].

The most common liquid-solid interface triboelectric nanogenerators adopt universal liquid-water as one tribo-material (usually positive tribo-layer)[142], and the water-energy in nature includes raindrops, water stream, and most importantly blue energy from ocean and tide[143] (Figure 2.7). As the most common liquid, water is very abundant in the ocean, and the mechanical energy generated by tides is huge but difficult to collect. The most practical liquid-solid triboelectric nanogenerator is utilized for energy harvesting of blue energy from tidal energy. Blue energy from the ocean, an energy device that collects ocean energy, makes full use of liquid water as a liquid dielectric friction layer to convert mechanical energy into electrical energy. The energy provided by marine tides and waves is huge and little dependent on season, day or night, weather, and environmental factors like temperature, etc. TENGs for blue energy harvesting from ocean and tide hold unique advantages because TENGs apply to a wide range of wave motions, subtle or strong, undercurrent or surface waves, multi-dimensional

waves, and flowing streams, especially low-frequency tides. Compared with electromagnetic effect-based wave energy harvesting devices, TENGs' materials are wide and most of the polymers are light and cost-effective compared with EMG's metal or magnet, which also makes it possible for packaging TENG units into a network architecture to multiply the output and tolerate the failure risk. The energy generated by ocean power generation may surpass "green energy" such as hydropower. A network of devices is possible to generate megawatt-level electricity per square kilometer of the sea surface. If these water-energy triboelectric nanogenerators are formed into a network and placed in the ocean, the irregular motion of seawater will be transformed into a steady stream of electricity.

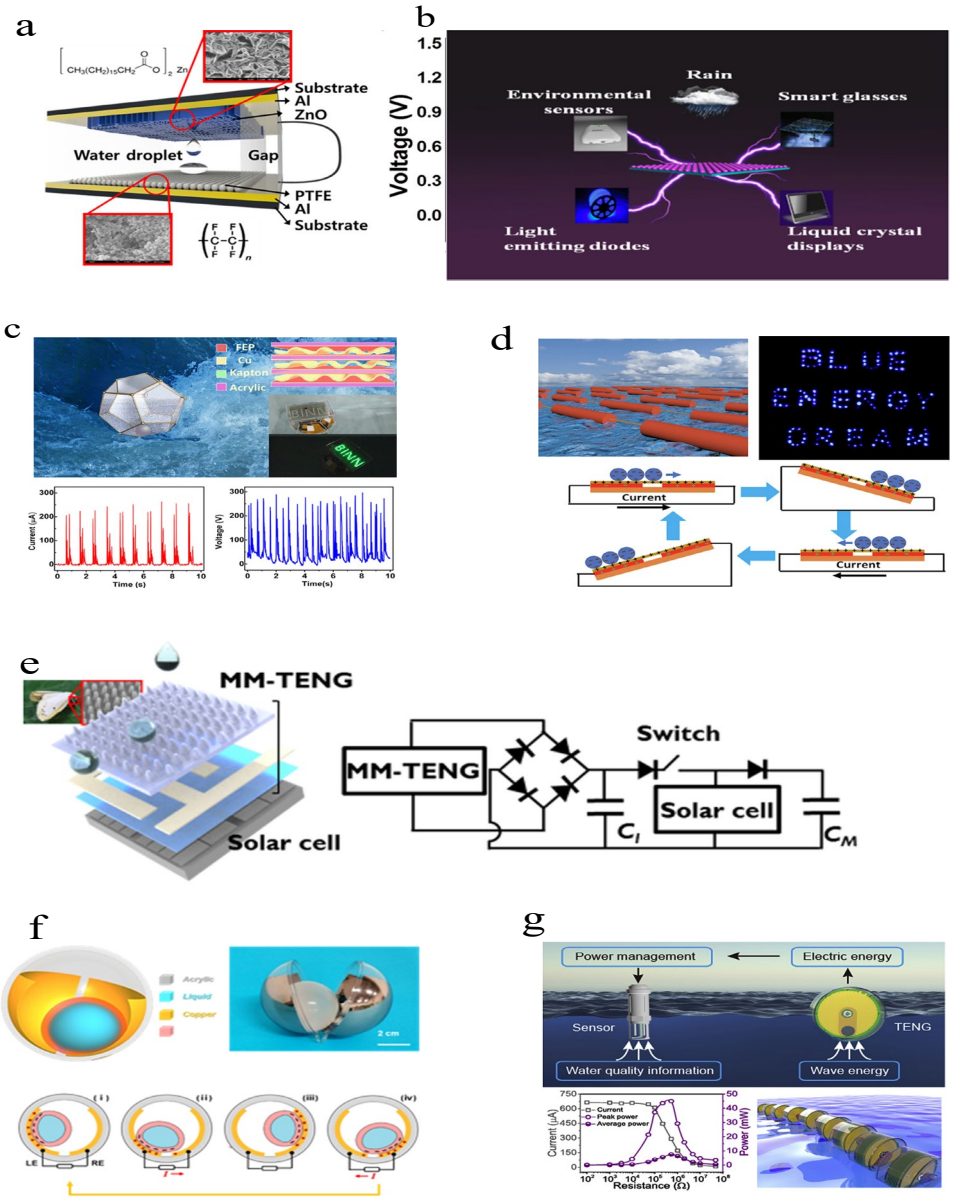

Figure 2.7 Blue Energy Harvesting Application (a) Water Droplet-driven Triboelectric Nanogenerator with Superhydrophobic Surfaces.[144] (b) Integrated Multi-unit Transparent Triboelectric Nanogenerator Harvesting Rain Power for Driving Dlectronics.[145] (c) Multilayer Wavy-structured Robust Triboelectric Nanogenerator for

Harvesting Water Wave Energy.[146] (d) Rationally Designed Sea Snake Structure-based Triboelectric Nanogenerators for Effectively and Efficiently Harvesting Ocean Wave Energy with Minimized Water Screening Effect.[147] (e) Biomimetic Anti-reflective Triboelectric Nanogenerator for Concurrent Harvesting of Solar and Raindrop Energies.[148] (f) Largely Enhanced Triboelectric Nanogenerator for Efficient Harvesting of Water Wave Energy by Soft Contacted Structure.[149] (g) High-performance Triboelectric Nanogenerators for Self-powered, In-situ, and Real-time Water Quality Mapping[150].

2.6 Summary

This chapter briefly introduced the fundamental status, historical background, working mechanisms, and material selection systems of typical triboelectric nanogenerators, mainly including the current research situation of these types of triboelectric

nanogenerators on which we did research and experiments on electrospinning membrane TENGs, 2D material dopant TENGs, different interface TENGs for blue energy, etc. To fully overview and discuss the structure design, material selection, and fabrication techniques of triboelectric nanogenerators, this chapter also highlights recent representative publications of related TENGs with innovative designs.

The environment offers a diverse array of energy sources, including mechanical, optical, thermal, and chemical energy sources. Within the human living environment, the mechanical energy generated from the human body by activities such as walking, running, typing, touching, even blinking, and breathing can serve as potential sources of energy. The collection of these waste energy sources is essential to meet long-term energy demands and promote sustainable development. The development of high-efficiency energy harvesting techniques and composite energy systems enables the acquisition of various energy sources and ensures that the devices or sensors can work

continuously under diverse conditions. Multiform nanogenerators have been extensively studied to improve the conversion efficiency of energy devices and establish self-powered energy supply systems for potential applications. Hybrid devices based on triboelectric nanogenerators refer to the devices that integrate, transform, and convert waste mechanical energy while effectively using solar energy, thermal energy, magnetic energy, and other environmental energy sources.

CHAPTER 3 Triboelectric Nanogenerators Based on Transition Metal Carbo-Chalcogenide (Nb_2S_2C and Ta_2S_2C) for Energy Harvesting and Self-Powered Sensing

3.1 Introduction

Sustainable and net-zero carbon emission power sources are acting as a thriving factor due to booming energy consumption. Particularly, TENGs as energy harvesting technology devices are attractive owing to their low costs, mechanical flexibility[9], easy assembly, and their low frequency working range[10].

Nowadays, Polydimethylsiloxane (PDMS) is often employed for material of TENG, which is a bio-friendly, non-toxic, flexible, highly durable, translucent, low-cost, and highly electronegative material. However, polymers usually obtain low dielectric constant as well as low capacitance and low charge abstaining capacity[14] accordingly, especially on TENGs during application with other electronic devices[15] as both energy

harvesters and self-powered sensors[16]. So far, major strategies implemented for improving TENG's electrical output have aimed at enhancing the triboelectric material dielectric performance[17-18] as well as the accumulated charge transfer density[19-20]. The introduction of high permittivity particles[21] into the substrate[22-23] at the interface, between the triboelectric materials[24] or with the electrode[25-27] has been proven effective in increasing the performance of TENG, from a wide variety of carbon nanotubes[28], ferromagnetic barium titanate[29], various two-dimensional materials[30-31], to liquid metals[32], etc.

In addition to the need to improve the electric properties of TENGs, research has shown that their tribological properties are of paramount importance as well [33]. Specifically, their wear resistance during sliding is a crucial factor in limiting their applicability[34]. For example, by adding PAO_4 as a lubricant, the coefficient of friction (COF) of the TCDC-TENG[35] was lowered. Moreover, water-based graphene oxide could be utilized

as a lubricant to enhance current density and reduce wear [36]. In this context, the addition of specifically 2D materials to the substrate matrix can have positive effects on the wear behavior[37] apart from improving the electric performance of TENGs[38].

2D materials have a commonality in their electrical production properties owing to their specificity in electron transport, which is another breakthrough for our research on performance enhancement and the commonality of 2D materials. These materials have attracted much attention in the fields of electronics, optics, and energy owing to their unique characteristic properties[42]. For example, MXenes belonging to the family of transition metal carbides and nitrides[43-44] are well-known for their good chemical stability, high mechanical strength, as well as excellent electrical conductivity. The two most used TMDs are molybdenum disulfide (MoS_2) and tungsten disulfide (WS_2) with different electronic band structures [45] and polymorphic structures[46]. The single-layered TMCC of these two species (Nb_2S_2C and Ta_2S_2C) was first successfully realized from

multilayered Nb_2S_2C[47] and Ta_2S_2C through electrochemical lithiation and sonication in 2022 and it was experimentally verified that the delaminated Nb_2S_2C outperformed its multilayered precursor material as an electrode material in electrochemistry[41].

TMCC can be considered an atomic combination of transition metal carbonitrides (MXene)[48] and transition metal dichalcogenides (TMDs)[10], which could be obtained by combining one layer of MXene with two half-layers of TMD[49]. The nature of the interaction between those 2D materials could contribute greatly to applications of energy storage[49], especially to the enhancement of TENG's performance demonstrated by plenty of previous research with TMD[10] and MXene[50-52]. It is expected that TMCC as their combination at the atomic level, would have a positive role in improving the electric performance of TENGs. However, to our best knowledge, there is no such research so far, not to mention the combination of tribology and triboelectric performance.

Therefore, in this research, two new species (Nb_2S_2C and Ta_2S_2C) of Transition Metal Carbo-Chalcogenides (TMCCs) were originally employed to develop TENGs doping with PDMS. In terms of the enhancement of electrical performance, both Nb_2S_2C-based TENG and Ta_2S_2C-based TENG were comparable, achieving the best electrical performance at the concentration of 3 wt. ‰. In addition, the tribological properties were investigated on a ball-on-disk setup against a steel ball counterbody. Ta_2S_2C/PDMS composite as the electronegative material was softer and presented a lower COF than pristine PDMS and Nb_2S_2C/PDMS composite. Their applications for energy harvesting and self-powered sensing were also demonstrated.

3.2 Experimental Section

3.2.1 Materials

PDMS (SYLGARD 184 Silicone Elastomer kit) was purchased from Dow Corning Co,

Ltd. Copper (Cu) wire and Aluminum foil were bought from DongguaYishengxing Copper and Aluminum Materials Co, Ltd, China. Cu/Ni conductive fabric (CNF) was purchased from 3M Corp. TMCCs (Nb_2S_2C and Ta_2S_2C powder) were synthesized from the laboratory. All reagents were used as received without further purification.

3.2.2 Characterization and Measurement

Field Emission Scanning Electron Microscope (SEM, Tescan MIRA) was used to characterize the morphology and Energy Disperse Spectroscopy (EDS) data were acquired simultaneously. X-ray diffraction (XRD) pattern with scanning from 5 to 70° (2θ) was recorded on an X-ray diffractometer (Rigaku SmartLab) to identify the crystalline phase. XPS spectra were investigated on an ESCALAB210 spectrometer. Fourier transform infrared (FTIR) absorption spectra were recorded on Spectrum 100, Perkin Elmer. The dielectric constant was measured using a precision LCR meter (Keysight E4980A). The triboelectric performance measurements under cyclic contact-

separation motion with adjustable frequencies were realized by a life test machine (ZX-A03, Zhongxingda, Shenzhen) with impact force signal monitored simultaneously by the DAQ (Dewetron, Dewe-2600 DAQ system). An oscilloscope (Keysight Infiniivision DSOX3024T) was adopted to measure the voltage, while an electrometer (Keithley 6514, Tektronix) was operated to record short-circuit current and short-circuit charge transfer. The coefficient of Friction was investigated by the Rtec Tribometer Instrument. KEYENCE 3D Laser Scanning Microscope was employed to measure wear track, scratch, and depth and produce 3D microscopic images. The simulation was conducted with COMSOL Multiphysics software.

3.2.3 Fabrication

The TMCC-TENGs were prepared by the blade coating method, as illustrated in Figure 1(a-b). TMCC was added at a certain weight ratio into PDMS and ultrasonicated for more than 12 hours for thorough distribution and dispersion, subsequently the curing

agent with 1/9 the weight of PDMS liquid was added into the mixture and stirred for 20 minutes, then blade coating the liquid to film with a thickness of ~2mm, finally put in an oven at 80° for 12 hours until completely cured. PDMS solution was cured by heat and the TMCC particles were mixed and dispersed uniformly and fixed in the cured PDMS matrix. To quantify the triboelectric performance, TMCC-TENGs were assembled as follows: the TMCC/PDMS composite adhered to Cu/Ni conductive fabric (CNF) to form the negative part, and the positive part was only CNF acting as both triboelectric material and electrode or Nylon as tribopositive material and adhered to CNF as an electrode. The CNF electrodes were connected through copper wire and then to the electrometer to measure and collect signals of open-circuit voltage (Voc) and short-circuit current (Isc) as well as short-circuit charge transfer (Qsc).

3.2.4 Tribology Evaluation

A ball-on-disk tribometer in linear reciprocating sliding (Rtec Instruments) was used to

test the frictional properties of the composites using a stroke length of 1 mm, a linear sliding velocity of 1 mm/s, an acceleration of 0.1s (1cm/s^2), and normal loads of 1, 5, 10, 20, and 30 N. The load of 1 N corresponds to a Hertzian contact pressure of around 0.5 MPa. The temperature was 19.5-24.8 °C and the relative humidity of 23%-56%. Stainless steel balls (100Cr6) with a diameter of 6 mm were used as counter bodies against the pristine PDMS plate and the composite plates. The tribological experiments were repeated three times for statistical representation, and the curves were used to calculate the corresponding mean values and standard deviations.

3.2.5 Finite Element Simulation through COMSOL

The Electrostatics Interface module of COMSOL was used to model the operation of TENG in contact-separation mode. The model was made with the same thickness (1 mm) and width (40 mm) as the experimental samples. The contact-separation behaviors were realized by the parametric sweep investigation with a separation distance of 10 mm. The simulations of the potential distribution correspond to various separation distances. The simulated open-circuit voltage was around 170 V while the measured values were around 120 V. The simulation results confirm the TMCC/PDMS TENG's operational concept, as shown in Figure 3.1e.

3.3 Results and discussion

3.3.1 Fabrication, Mechanism and Characterization

Monolayer Nb_2S_2C has a molecular structure where one layer of carbon atoms is sandwiched by two layers of Nb/Ta atoms, with a layer of S atoms above and below the

outermost layer, while NbS_2 has a molecular structure where 2 hexagonal S atomic layers sandwich a layer of transition metal atoms, as shown in Figure 3.1a. Therefore, 2D layers of Nb_2S_2C can combine the chemical reactivity of NbS_2 while maintaining a mechanically robust and metallic conductor carbide core which is not achievable by transition metal carbide or nitride alone. The other TMCC Ta_2S_2C has similar structure and properties.

The creation of TMCC/PDMS composites involved the incorporation of TMCC particles into a PDMS precursor as depicted in Figure 3.1a, followed by a blading process in Figure 3.1b. After curing, the TMCC/PDMS composite was then constructed into a contact-separation mode TENG, as demonstrated in Figure 3.1c. Here, nylon served as the positive dielectric, while the TMCC/PDMS composite functions as the negative dielectric. Both dissimilar dielectric films were attached to Cu/Ni conductive fabric (CNF) as electrodes on each side with the other side opposite each other. We

chose Cu/Ni conductive fabric as the electrode because the Cu/Ni conductive fabric has good flexibility and air permeability as well as strong conductivity, which is very suitable for wearable electronics. The operational mechanism of the vertical contact-separation mode under an external force is schematically represented, demonstrating the electron transfer process in Figure 3.1d. Due to their varying electron affinities, an equal number of positive and negative charges were generated on the surface of both dielectric layers in the initial state (Figure 3.1d (i)). In the second state (Figure 3.1d (ii), the external force separated the two membranes, creating a gap and an electric potential difference, thus generating an electrical current with electron transfer from one electrode to the other via an external load (or electrometer). When the two layers were fully separated (Figure 3.1d(iii)), electrostatic equilibrium was achieved, and no electron movement occurred. When the external force disrupted this equilibrium, a new opposite potential difference was created, causing the electron current to flow in the

opposite direction (Figure 3.1d(iv)). Besides electron transfer where orbital overlap leads to charge tunneling, there is also mass (material) transfer where polymer chain entanglement and intermolecular bonding lead to heterolytic bond scission[53] as well as ion transfer[54-55]. Throughout the contact and separation process, electrons continuously flowed between the bottom and top electrodes, generating alternating current (AC)[56]. For an understanding, the associated potential distribution of the positive and negative dielectric materials was simulated and displayed using COMSOL Multiphysics software, as shown in Figure 3.1e.

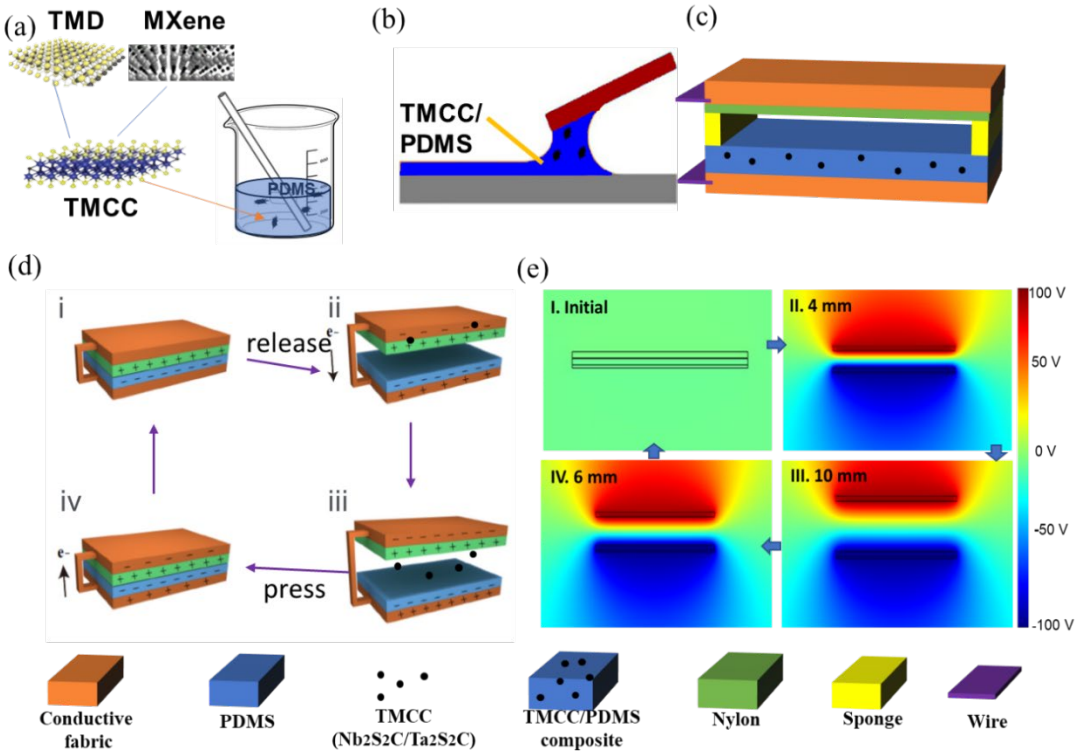

Figure 3.1 Fabrication process of (a) Doping (b) Blade coating for TMCC/PDMS composites. (c) The architecture of vertical contact-separation mode of TENG (d) Mechanism illustration and (e) COMSOL simulation for a cycle of contact-separation.

From the scanning electron microscopy (SEM) images of Nb_2S_2C/PDMS composite film in Figure 3.2a and Ta_2S_2C/PDMS composite in Figure 3.2b, it could be seen that Nb_2S_2C and Ta_2S_2C particles were dispersed into the PDMS matrix. The corresponding

EDS-elemental mapping images authenticated the obvious presence of Niobium (Figure 3.2c) or Tantalum (Figure 3.2d) elements. As silicon was only present in PDMS but not in the dopants, the silicon element was shaded in the corresponding EDS image where the transition metal, carbon, and sulfur elements were present, indicating that TMCC/PDMS composites were successfully prepared.

Raman spectroscopy in Figure 3.2e-f can detect the fingerprint pattern and quantitatively be employed to identify phases. The Raman spectroscopy showed peaks at wavelengths of ~ 2,960 cm^{-1} and 2,970 cm^{-1} in Nb_2S_2C/PDMS composites and Ta_2S_2C/PDMS composites respectively, which were absent as compared to pure PDMS. Moreover, other Raman characteristic peaks of PDMS at ~ 490 cm^{-1}, ~ 600 cm^{-1}, ~ 700 cm^{-1}, ~ 1,280 cm^{-1}, ~ 1,420 cm^{-1}, ~ 2,500 cm^{-1} became less significant after doping of TMCC particles.

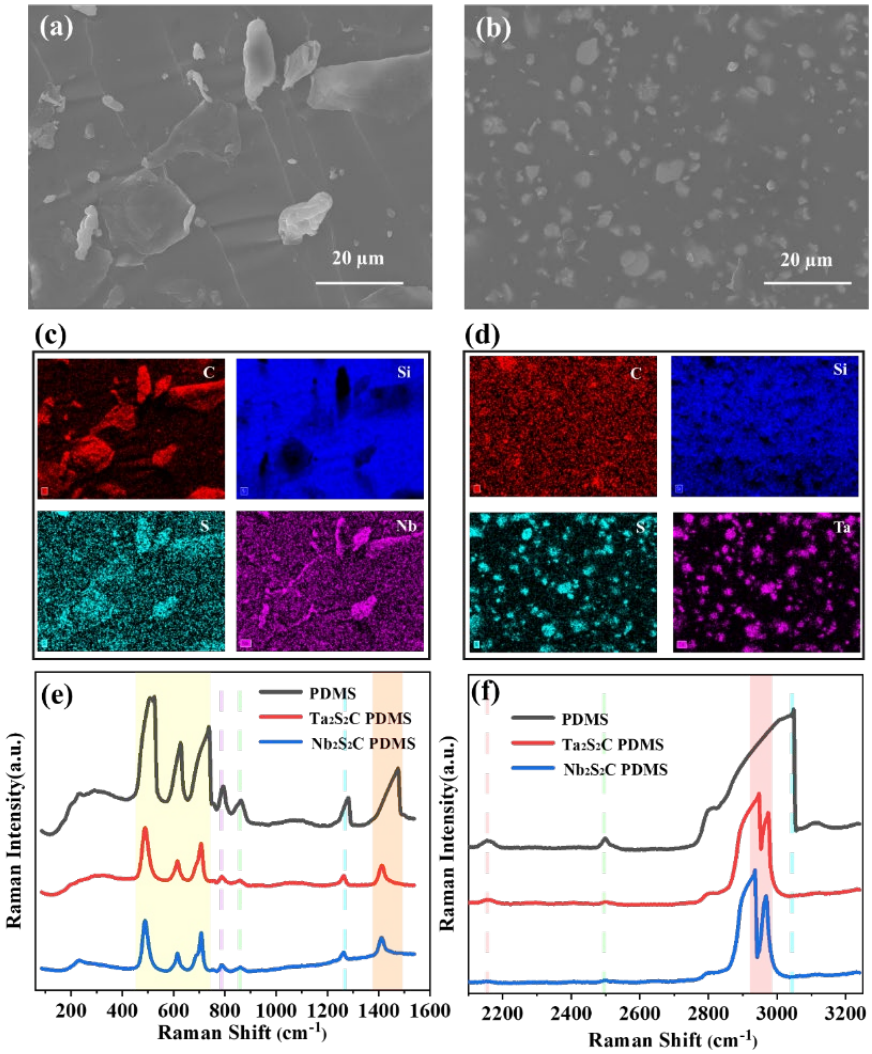

Figure 3.2 Morphology analysis and structural characteristics of tribo-layer materials.

(a) SEM images of Nb_2S_2C/PDMS composite samples. (b) SEM images of Ta_2S_2C/PDMS composite samples. (c) EDS-elemental mapping images of the Nb_2S_2C/PDMS composite sample. (d) EDS-elemental mapping images of the Ta_2S_2C/PDMS composite sample. (e-f) Raman pattern of pure PDMS, Nb_2S_2C/PDMS

composite, and Ta_2S_2C/PDMS composite.

More EDS mapping was shown in Figure 3.3a-b, and X-ray diffraction patterns were listed in Figure 3.3c-d. The diffraction peaks at 2θ ~12° and ~13° were attributed to doping of Nb_2S_2C and Ta_2S_2C, respectively. The dielectric constant plays a crucial role in determining the electric performance of TENGs, and the influence of dopants on the dielectric properties of PDMS was examined. PDMS films of 4 cm^2 were encapsulated on both sides of conductive plates to create a parallel plate capacitance model. The capacitance values of all samples were measured across a frequency range of 10^2 to 2MHz. The method for measuring the dielectric constant is based on the parallel plate capacitor conditions, and the dielectric constant can be calculated using the following formula:

$$C = \varepsilon S / 4\pi k d$$

In the formula above, C stands for capacitance, ε symbolizes the dielectric constant, k is the electrostatic force constant ($k = 8.9880 \times 10^9$ Nm/C), d represents the thickness of the film (or the distance between two electrode plates), and S refers to the effective area (or overlapping surface area) of two electrode plates[16]. The dielectric constant (or permittivity) was related to the contents of the dopant in the PDMS substrate. The dielectric constant slightly increased when the ratio of TMCC doped into pure PDMS is from 1 wt. ‰ to 3 wt. ‰, while excessive amount of TMCC dopants in PDMS up to 10 wt. ‰ could decrease the dielectric constant of TMCC composite, for both Nb_2S_2C (Figure 3.3e) and Ta_2S_2C (Figure 3.3f). This is consistent with the electrical output trend at different concentrations, confirming that a higher dielectric constant results in more electrostatic energy storage capacity in an electric field and thus better performance of TENG[15].

X-ray photoelectron spectroscopy (XPS) was utilized to study the surface chemistry of

the Nb_2S_2C/PDMS composite, as shown in Figure 3.4a-d, as well as the Ta_2S_2C/PDMS composite shown in Figure 3.4e-h. The Ta 4f spectrum at ~ 24 eV was assigned to Ta_2S_2C. Comparatively, the Nb 3d spectrum at ~ 203 eV assigned to Nb_2S_2C was not that obvious. C elements had significant existence in both TMCC and PDMS substrates, and S element also showed for C-Nb-S or C-Ta-S.

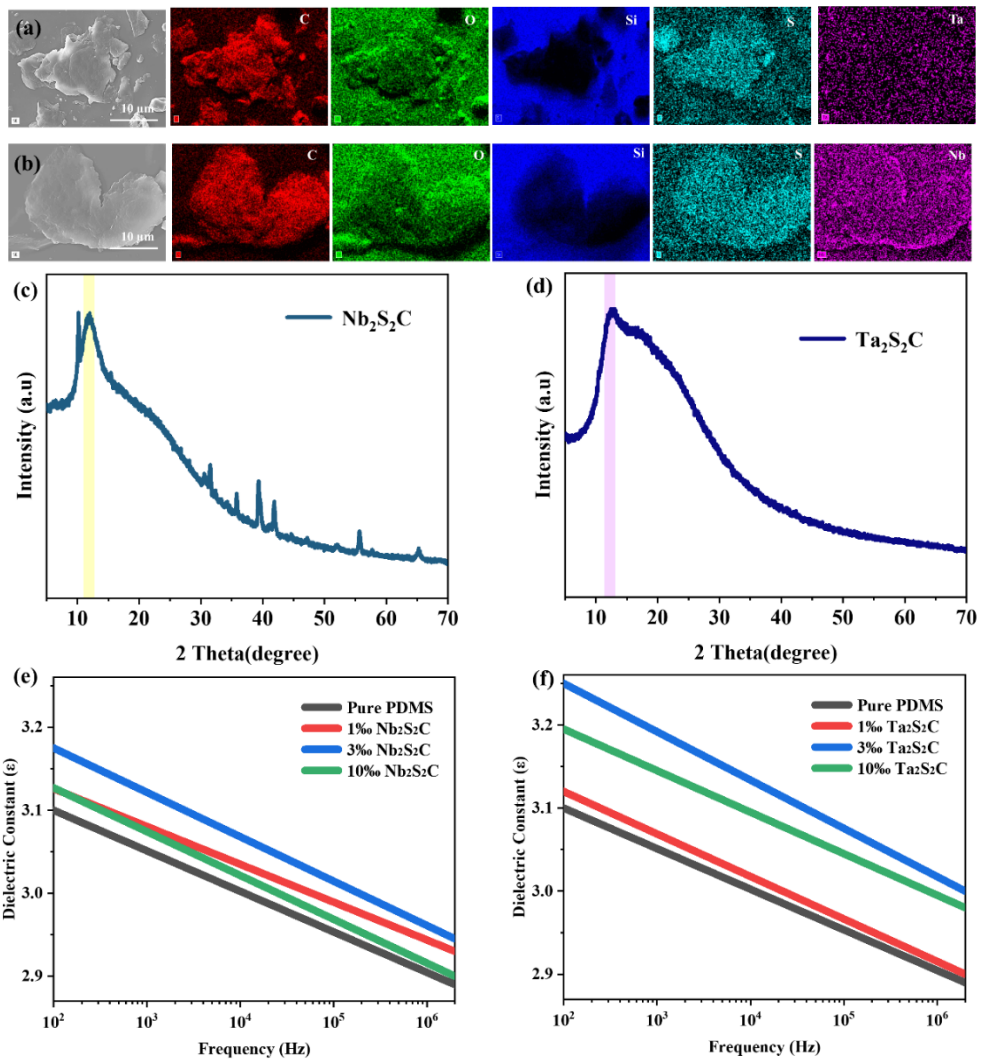

Figure 3.3 Morphology and elemental analysis (a) EDS-elemental mapping images of the Nb_2S_2C/PDMS composite. (b) EDS-elemental mapping images of the Ta_2S_2C/PDMS composite. (c) XRD Pattern of Nb_2S_2C/PDMS composite. (d) XRD Pattern of Ta_2S_2C/PDMS composite. (e) Frequency dependence of dielectric constant of Nb_2S_2C/PDMS composite with different concentrations of 0, 1 wt. ‰, 3 wt. ‰, and

10 wt. ‰. (f) Frequency dependence of dielectric constant of Ta_2S_2C/PDMS composite with different concentrations of 0, 1 wt. ‰, 3 wt. ‰, and 10 wt. ‰.

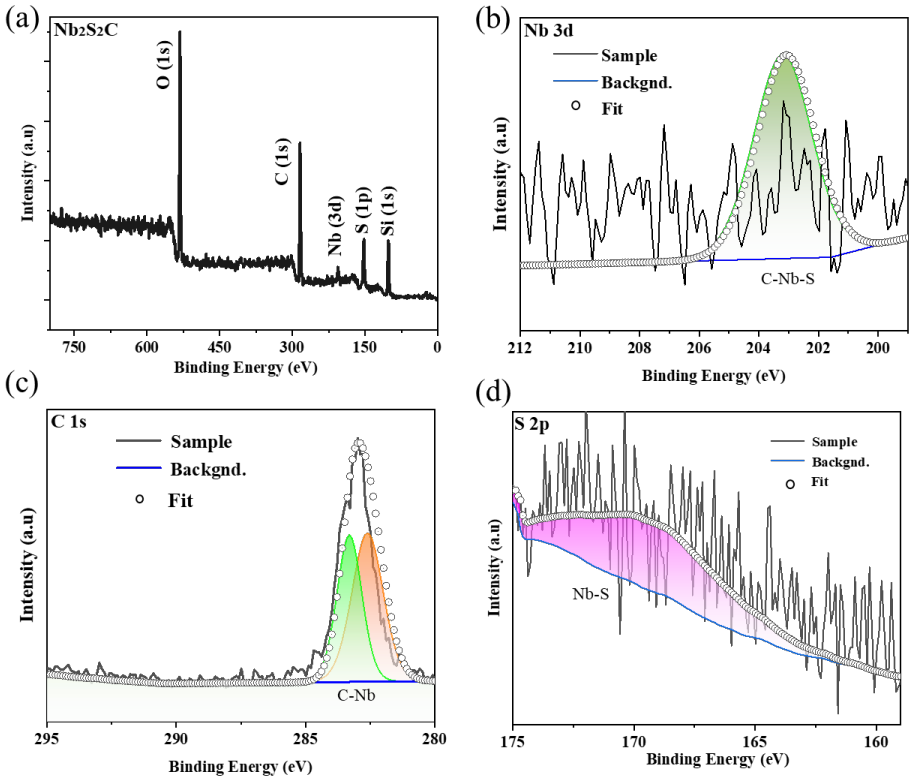

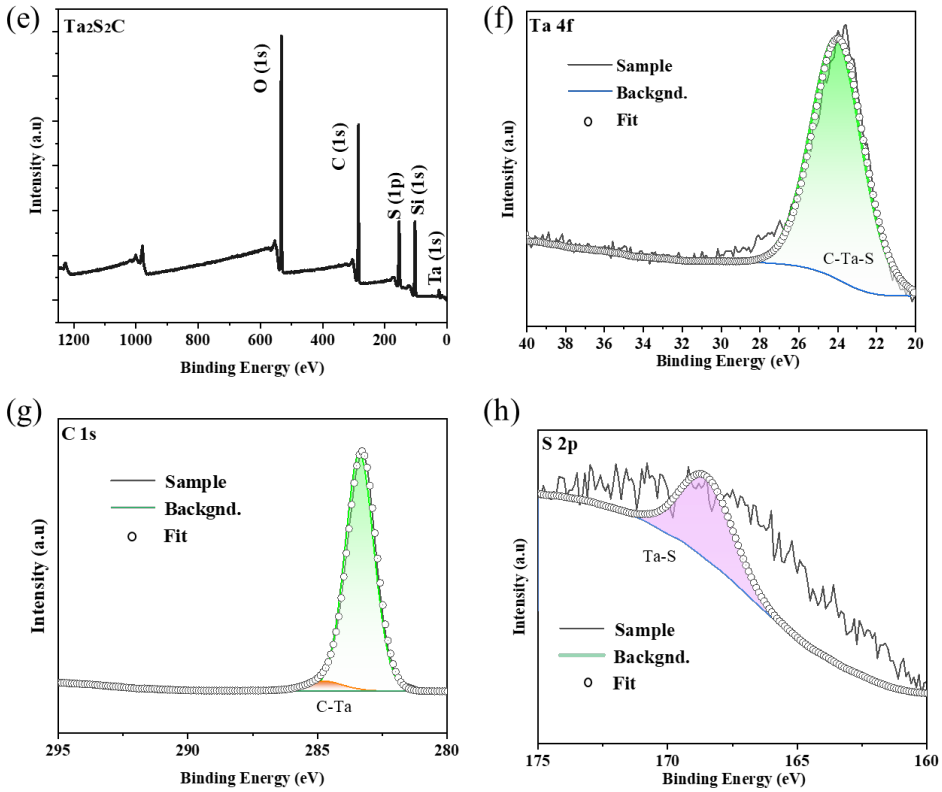

Figure 3.4 XPS spectra of TMCC/PDMS composites. (a) Nb_2S_2C, (b) Nb 3d, (c) C 1s, (d) S 2p. (e)Ta_2S_2C. (f) Ta 4f, (g) C 1s, (h) S 2p.

3.3.2 Electrical Output

Both TENGs using tribonegative material of TMCC/PDMS composites (TMCC-TENGs) were systematically fabricated and evaluated with different weight ratio concentrations of 1 ‰, 3 ‰, and 10 ‰, respectively. To test the electric performance

in dependence on the TMCC concentrations, the voltage, current, and charge transfer were measured (Figure 3.5) in contact separation mode at 40 N impact force and 3 Hz frequency, utilizing TENG of 16 cm^2 size (4 cm×4 cm). For the pristine PDMS, an open circuit voltage (Voc) of 25 V, short circuit current (Isc) of 1.8 μA, and charge transfer (Qsc) of 21 nC. Compared with pristine PDMS, TMCC-TENGs substantially improved electrical performance regardless of the concentration. The optimum weight ratio to achieve the best electric performance for Nb_2S_2C based TENG appeared at 3 wt. ‰, with open circuit voltage (Voc) of 112 V, short circuit current (Isc) of 8.6 μA, and charge transfer (Qsc) of 175 nC. Similarly, the optimum weight ratio for Ta_2S_2C based TENG was also 3 wt. ‰, reaching a Voc of 127 V, Isc of 9.6 μA, and Qsc of approximately 230 nC. This trend indicates that the incorporation of Nb_2S_2C and Ta_2S_2C into PDMS significantly enhances its ability to store charge. The enhancement in TENG performance might be mainly attributed to the polarization of particles with an increase

in dielectric constant and charge trapping. The introduced TMCC nanoparticles increased the permittivity of composite and the capacitance of friction materials, and then comprehensively enhanced the output performance[17, 21], while over a certain concentration, the permittivity and electrical performance will decrease. Niobium and tantalum are transition metals as indispensable twin elements with shared physical and chemical properties, which is why Nb_2S_2C/PDMS and Ta_2S_2C/PDMS TENG had similar performances. Furthermore, TMCC/PDMS composite materials exhibit a significantly higher surface charge density as calculated by charge transfer, being 1.09375×10^{-4} C/m^2 for Nb_2S_2C/PDMS composite and 1.4375×10^{-4} C/m^2 for Ta_2S_2C/PDMS composite, which is 8.33 times and 10.95 times higher than pristine PDMS, respectively. Thereby, higher surface charge density resulted in better electrical performance as well as friction and energy efficiency for TMCC/PDMS composite with identical tribopositive materials.

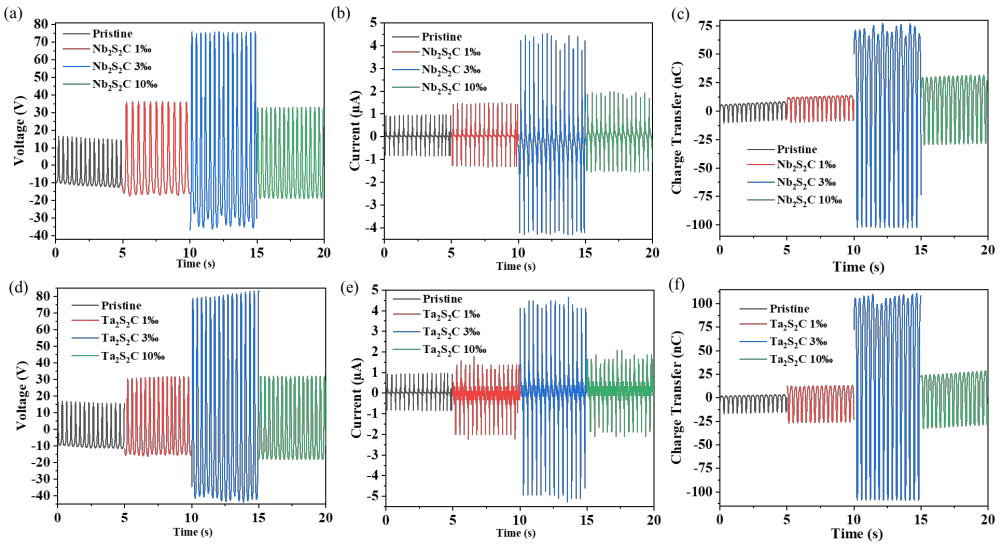

Figure 3.5 Electric performance at 40 N, 3 Hz, 16 cm^2 (a) Open circuit voltage, (b) Short circuit current, (c) Charge transfer of Nb_2S_2C based TENG at different weight ratios, and (d) Open circuit voltage, (e) Short circuit current, (f) Charge transfer of Ta_2S_2C based TENG at different weight ratios.

3.3.3 Impact of external factors

We have also evaluated the influence of two main external impact factors (force and frequency) on the electrical output performance of both Nb_2S_2C based TENG (Figure 3.6) and Ta_2S_2C based TENG (Figure 3.7). We adopted Cu/Ni conductive fabric as both

positive dielectric and electrode and PDMS composite as negative dielectric with a smaller effective size of 4 cm^2 (2 cm×2 cm). Specifically, at a fixed impact force of 20 N, with the frequency increased gradually from 1 Hz to 7 Hz, the Voc increased slightly from 50V to 59V (Figure 3.6a), with Isc raised from ±0.3 μA to ±1.5 μA (Figure 3.6b) and Qsc increased from 17 nC to 20 nC (Figure 3.6c). While at a set frequency of 2 Hz, when the impact force increased from 10 N to 20 N, the Voc and Qsc increased significantly from 15 V/6 nC to 65 V/24 nC, but only increased slightly when further increased the impact force up to 100 N with the maximum value of 90 V (Figure 3.6d)/32 nC (Figure 3.6f), while the Isc increased sequentially from 0.8 μA to 1.8 μA (Figure 3.6e), correspondingly to the impact forces from 10 N to 100 N.

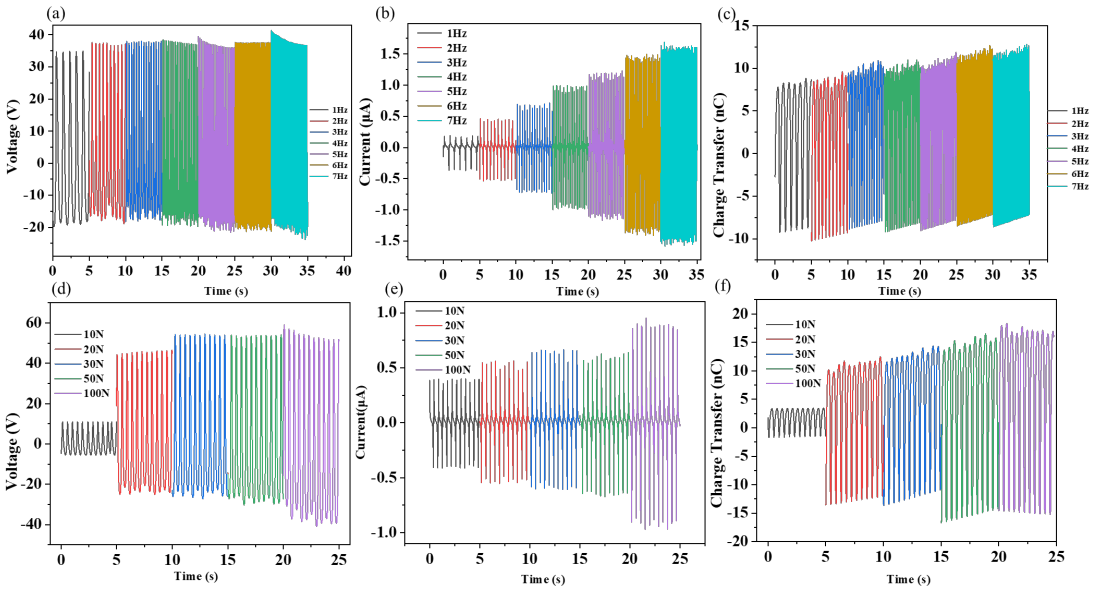

Figure 3.6 Different frequency and force on 3 wt. ‰ Nb_2S_2C based TENG of 4 cm^2 size for electrical performance (a) Open circuit voltage (b) Short circuit current (c) Charge transfer at different frequencies from 1 Hz to 7 Hz at a force of 20 N and (d) Open circuit voltage (e) Short circuit current (f) Charge transfer at different impact forces of 10 N, 20 N, 30 N, 50 N, and 100 N at a frequency of 2 Hz.

For the Ta_2S_2C based TENG, at a fixed impact force of 20 N with a contact-separation distance of approximately 1.7 cm, as the frequency increased gradually from 1 Hz to 7 Hz, the Voc and Qsc remained similarly at around 70 V (Figure 3.7a)/42 nC (Figure

3.7c), while the Isc increased constantly from 1.0 μA to 3.05 μA (Figure 3.7b). The influence of different impact forces of 10 N, 20 N, 30 N, 50 N, and 100 N at a fixed frequency of 2 Hz showed a general increase in Voc, Isc, and Qsc, with an approximate increase from 37 V to 125 V (Figure 3.7d), 1.08 μA to 2.6 μA (Figure 3.7e), 14 nC to 39 nC (Figure 3.7f), respectively.

A greater force leads to more intimate contact between the two triboelectric surfaces with a larger contact area and more charges. The output voltage and current of a TENG are directly related to the amount of charge transferred and the rate at which this transfer occurs. A greater force represents a higher mechanical energy input into the system, which can lead to a higher output because it enhances the charge transfer process and the rate of change in the electric field, which is both crucial for generating electricity in a TENG. At certain impact forces, a higher frequency can stimulate electrons faster and the surface charge of the contact layer cannot be quickly neutralized at an elevated

frequency, which generates an enlarged current. Attributed to more intimate contact between positive and negative dielectric, the output of the TENG increases at a larger magnitude of applied impact force[151]. The inconsistent variation of electrical outputs Voc/Qsc and Isc with frequency change might be explained according to the Gauss theorem, where the Voc and Qsc are independent of speed, which means that the variation of contact frequency will cause little change of the Voc and Qsc[152], while Isc is strictly in positive correlation with the relative movement speed/frequency[153].

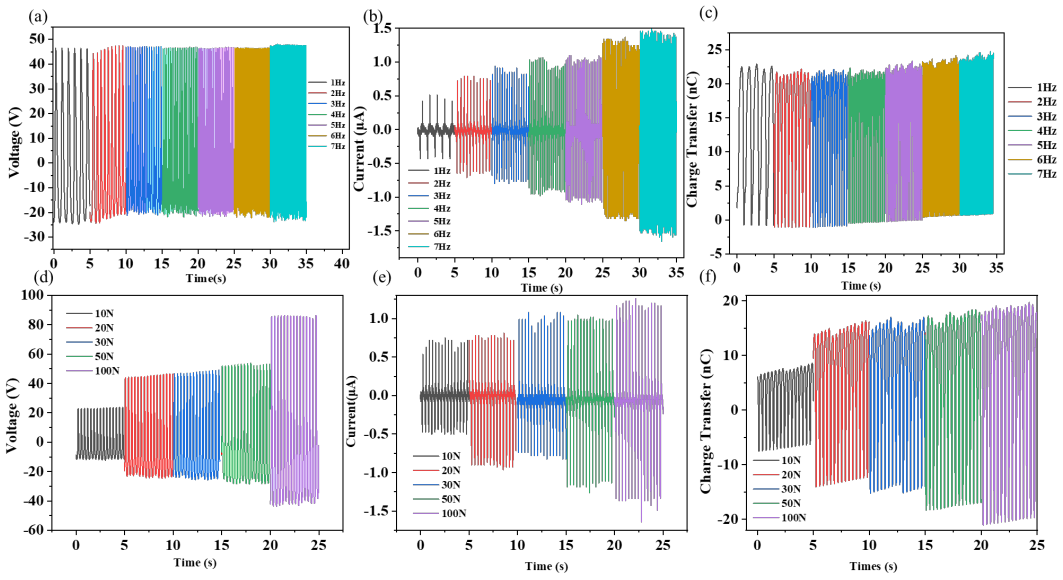

Figure 3.7 Different frequency and force on 3 wt. ‰ Ta_2S_2C based TENG of 4 cm^2 size for electrical performance (a) Open circuit voltage (b) Short circuit current (c) Charge

transfer at different frequencies from 1 Hz to 7 Hz at a force of 20 N and (d) Open circuit voltage (e) Short circuit current (f) Charge transfer at different impact forces of 10 N, 20 N, 30 N, 50 N, and 100 N.

3.3.4 Applications

Because the contact-separation mode TENG can only generate an alternating current, a rectifier needs to be used for converting an AC into DC. The full-wave rectifier uses two diodes to pass both the positive and negative halves of the incoming AC wave to the output, resulting in a smoother DC signal with a polarity that is always the same, and then capacitors could be charged periodically to power devices. With rectifier and capacitor circuit integration (Figure 3.8a), a capacitor of 100 μF was charged by TENG, and then a calculator or watch could be powered up consistently and stably[154]. The charging capacity was further evaluated by charging different values of capacitors

including 1.5 μF, 100 μF, and 330 μF with charging rates of 220 mV/s, 4 mV/s, and 1.4 mV/s, respectively, as shown in Figure 3.8b. It is worth noting that the triboelectric generator has a high internal impedance output characteristic, making it hard to directly charge batteries[12-13].

Under 20 N force and 2 Hz frequency impact with a size of 10 cm^2, different resistors ranging from 1 kΩ to 2 GΩ were adopted to evaluate the output voltage and current, and then the power density output was calculated accordingly[17]. The voltage rises as resistances increase, and by contrast, the current decreases gradually with the increase of resistances. The instantaneous peak power density of the TMCC-TENG could be calculated by $P = I^2R/S$, where P, I, R, and S denote power density, output current, external resistance, and effective size of the TMCC-TENG, respectively[155]. The power density of Nb_2S_2C based TENG increased with the resistances changed from 1 kΩ to 500 MΩ and reached the maximum of 1,360 mW/m^2 at 500 MΩ load resistor (Figure

3.8c). Under the same circumstances, the power density of Ta_2S_2C based TENG also reached a top value of 911 mW/m^2 with a resistor of 500 MΩ load (Figure 6d).

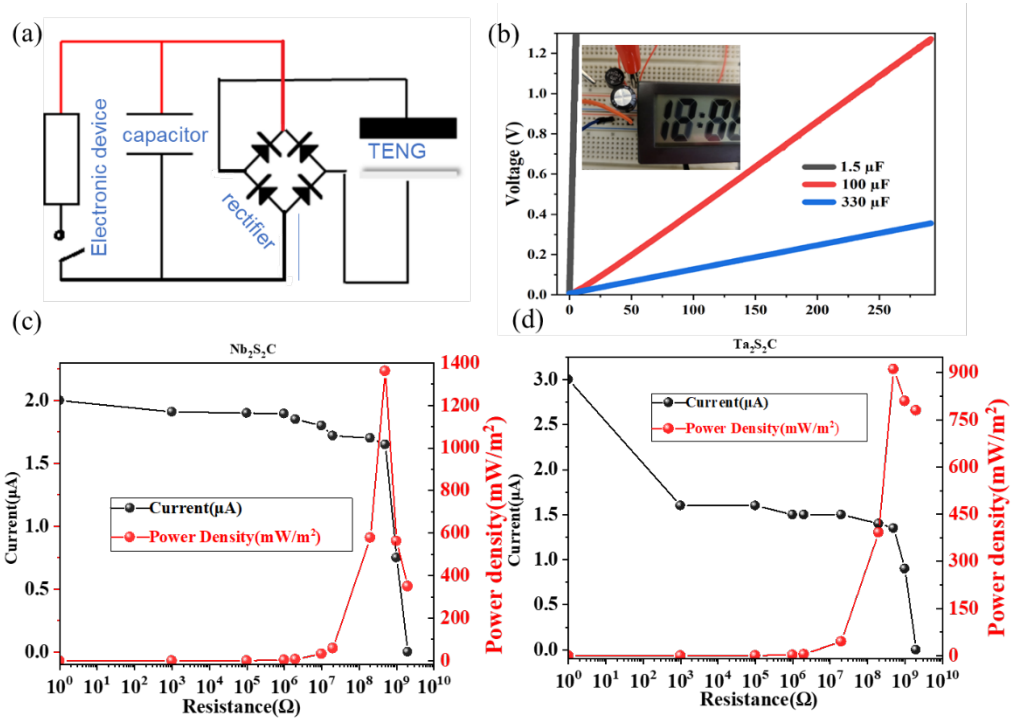

Figure 3.8 (a) Electrical circuit of TENG charging capacitor and powering electronic device. (b) The voltage curve of charging capacitors of 1.5 μF, 100 μF, and 330 μF and the inset of (b) is the image of powering clock by the charged capacitor. (c) Current and output power density curve of the Nb_2S_2C based TENG at different resistances from 1 Ω to 2 GΩ under 20 N and 2 Hz impact. (d) Current and output power density curve of the Ta_2S_2C based TENG at different resistances from 1 Ω to 2 GΩ under 20 N and 2 Hz

impact.

Figure 3.9a shows that TMCC-TENG can be attached to several parts of the human body for energy harvesting and act as self-powered human gesture sensors. Mechanical energy could be harvested by clapping with Voc at 15 V (Figure 3.9a(i)), and when one single TMCC-TENG was attached under the insole while running, generating Voc up to ~ 90 V (Figure 3.9a(ii)). In order to study the electric performance of human gesture sensors, TMCC-TENG were deformed into various shapes and fixed at different positions of the human body to investigate the electrical signal generated while repeated bending, where TMCC-TENG adhered to elbow exhibited Isc of 0.33 μA (Figure 3.9a(iii)) and finger exhibited Voc of 2 V, respectively (Figure 3.9a(iv)). It is also vital to assess TENG's physical reliability during long-term operation in actual application scenarios. It is noted that TMCC-TENG's voltage output remained stable after being

exposed to air for up to 6 months (Figure 3.9b(i)) owing to PDMS's stale physical and chemical nature. Moreover, after 35,000 cycles of continuous contact separation strikes, the amplitude of the triboelectric output signal remained almost consistent (Figure 3.9b(ii)), demonstrating the excellent durability of TMCC-TENGs.

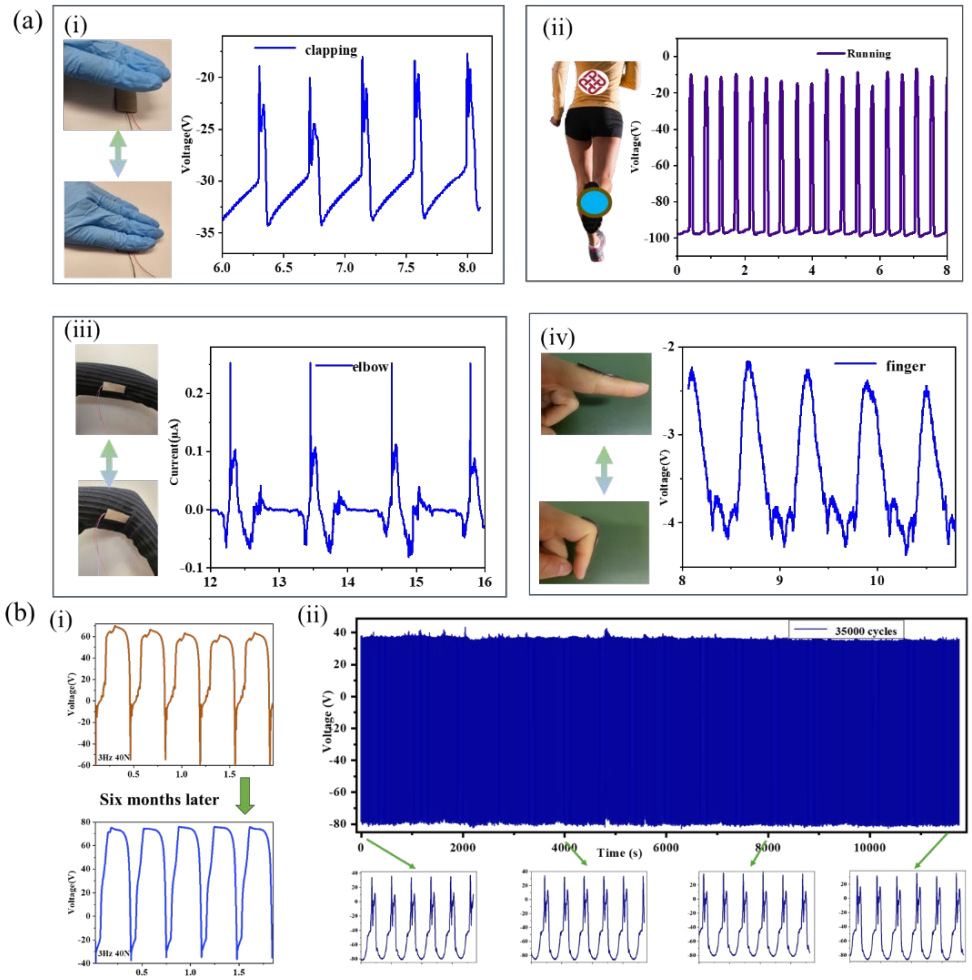

Figure 3.9 (a) Applications of TMCC-TENG. The output response of wearable harvester and sensor under mechanical movements (i) clapping and (ii) running. The

self-powered sensing at different positions of the human body (iii) elbow and (iv) finger bending. (b) Durability experiments for TENG (i) before and after six months and (ii) operated for 35,000 cycles at a frequency of 3 Hz.

Comparison of some similar work results in representative publications, which demonstrated that our TMCC-TENG achieved above-average enhanced performance, is listed in Table 1 below.

Table 1. Performance comparison of our device with other two-dimensional materials based TENGs

Negative Layer (Dopants@)	**Positive Layer**	**V (V)**	**I (μA)**	**Power density** (mW/m^2)	**Ref.**
PDMS	AgNPs/MXene ink fibre	7.7	7	/	[156]
Graphene	PET	5	0.5	/	[157]
Graphene Nanosheets/PTFE	Al	96	3.66	390	[129]
Silicone	Crumpled Graphene	9.3	/	15	[158]
PTFE	g-C_3N_4@PA_{66}	80	6	45	[24]
Al_2O_3/Hexagonal Boron Nitride	Graphene	1.2	/	/	[159]
Polyimide/Boron Nitride Nanosheet	Al	65.9	4.5	214	[133]
PDMS	MoS_2/SiO_2	25	1.2	22.5	[160]
LC-WS_2	PET	12.2	/	138	[37]
Crumpled Mxene	Skin	16.4	2.67	28.9	[161]
Carbonized MXene/ZiF-67	hand	35	12.5	55	[127]
Mg-Al Layered Double Hydroxides	water droplet	13	1.6	/	[162]
Kapton/PI	rGO	90	6.3	/	[163]

Nb_2S_2C@PDMS	Nylon	112	8.6	1,360	this work
Ta_2S_2C@PDMS	Nylon	130	9.2	911	this work

3.3.5 Tribology Properties

To evaluate the friction and wear performance of the fabricated TMCC/PDMS composites as compared to the pristine PDMS samples, we performed reciprocating ball-on disk experiments[164] using a 100Cr6 6 mm diameter steel ball as counter body. At a load of 1 N, the average coefficient of friction (COF) quickly increased within the first 100 seconds of running-in to a maximum value of 0.71, 0.43, and 0.395 for Nb_2S_2C/PDMS composite, Ta_2S_2C/PDMS composite, and pristine PDMS, respectively. Subsequently, the COF slightly decreased until it stabilized at a steady-state value of 0.62, 0.43, 0.28 for Nb_2S_2C/PDMS composite, Ta_2S_2C/PDMS composite, and pristine PDMS, respectively. The tribological experiments were repeated three times[118] at the load of 1 N, and then the corresponding standard deviations (shade area) and mean values were calculated, as shown in Figure 3.10a. Besides, experiments under other

loads including 5 N, 10 N, 20 N, and 30 N were also investigated with the average values shown in bar graph Figure 3.10b. Generally, the COF of both TMCC/PDMS composites was higher than that of the pristine PDMS samples, while the COF of the Nb_2S_2C/PDMS composite was found to be consistently higher than that of the Ta_2S_2C/PDMS composite under different loads. This can be attributed to the evolution of the real contact area, leading to higher adhesion between the friction partners. With an increase in load from 1 to 5 N, the COF of all tested samples drastically drops by more than 50 %. The lowest COF for the pristine samples was observed at the maximum load of 30 N, whereas both composites demonstrated the lowest COFs at 20 N from where the COF again increases at 30 N. We anticipated that this is related to the activation of the beneficial tribological properties of the TMCCs with higher loads resulting from their layered structure facilitating easy shear. At the highest load of 30 N, the TMCC might start to degrade during sliding and, therefore, lose its beneficial

tribological effect.

For the reciprocating ball-on-disk system in the tribological experiment of COF, we used 6 mm diameter stainless steel balls (100Cr6) as a counter body with PDMS plates of around 2 mm thickness underneath. Figure 3.10c shows the scratches on the steel ball, pristine PDMS, and micrographs of 10 wt. ‰ Nb_2S_2C/PDMS composite and 10 wt. ‰ Ta_2S_2C/PDMS composite after COF

experiment under the same conditions. After one hour of friction under 1 N with the counter body of 100Cr6 steel ball and PDMS substrate, the average depth difference values of ten times of pristine PDMS, Nb_2S_2C/PDMS composite, Ta_2S_2C/PDMS composite were 9.244 µm, 6.096 µm, 4.708 µm, respectively. In these examinations imitating sliding mode TENG, significant wear tracks were not detected for TMCC/PDMS composites. Nanoindentation or nano scratch experiment can be further experimented with to recognize wear or scratches. Overall, Ta_2S_2C/PDMS composite

exhibited smaller COF, reduced wear, and softer texture as compared to Nb_2S_2C/PDMS composite, while maintaining excellent electrical performance with slightly larger Voc, Isc, and Qsc. The triboelectric performance of TMCC/PDMS was higher than pristine PDMS. The COF of TMCC/PDMS is higher than that of pure PDMS, which means it generates higher friction in sliding situations and might prevent contact-separation TENG from sliding sideways.

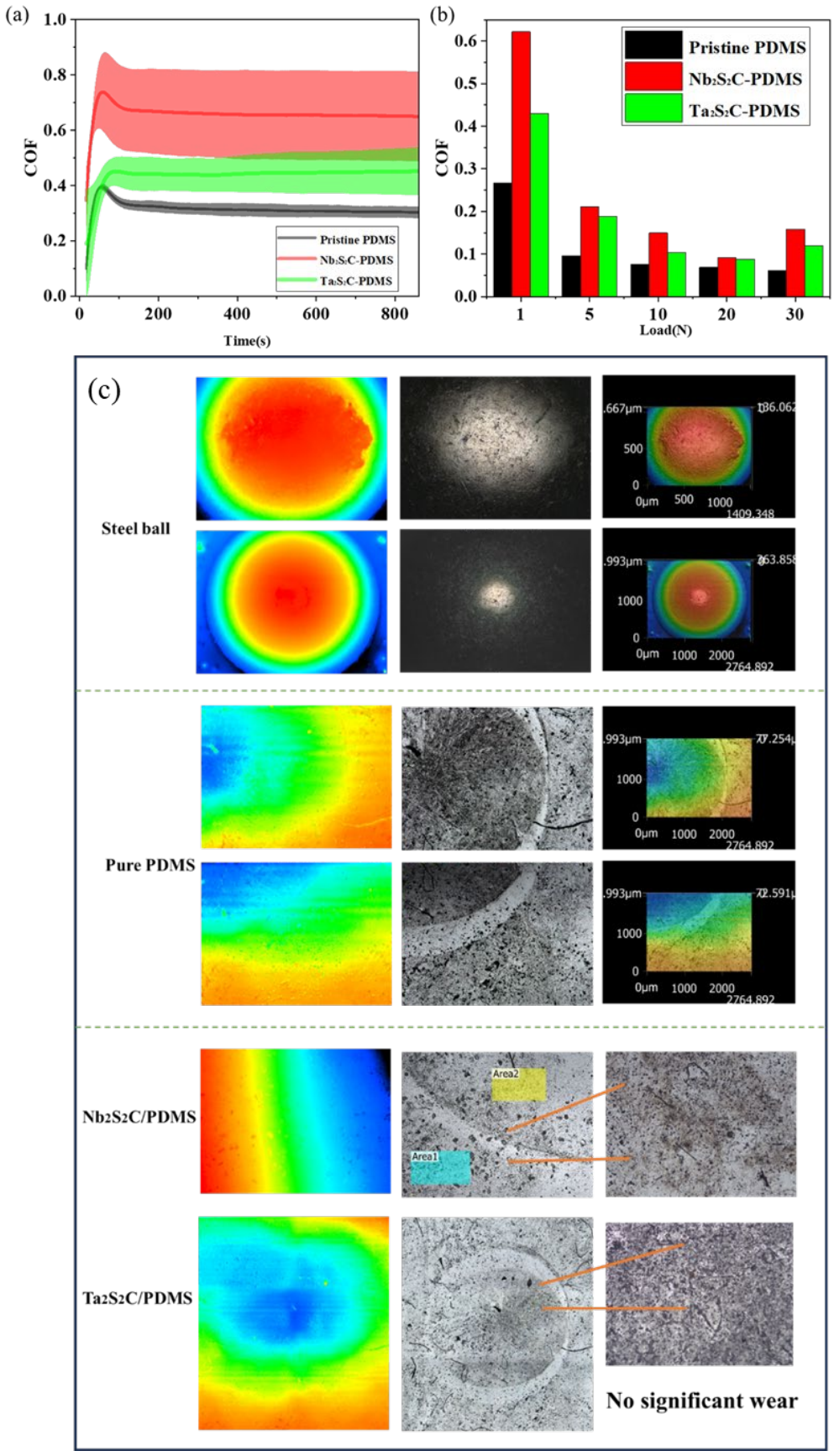

Figure 3.10 Tribology Test for friction performance of pristine PDMS, Nb_2S_2C/PDMS

composite, and Ta_2S_2C/PDMS composite substrate in ball-on-disk experiments (a) Derivatives and average COF of 3 times experiments from time 0 s to 850 s at the load of 1 N. (b) average COF after data stabilization (150s after the start of the experiment approximately) at the load of 1 N, 5 N,10 N, 20 N, 30 N, respectively. (c) Depth difference and SEM Micrograph of the steel ball and pristine PDMS, Nb_2S_2C/PDMS composite, and Ta_2S_2C/PDMS composite after the consistent ball-on-disk experiment for one hour under 1N.

3.4 Conclusion

In summary, two species (Nb_2S_2C and Ta_2S_2C) of a new family of 2D materials, Transition Metal Carbo-Chalcogenides (TMCCs), were first employed to develop new TENGs with PDMS. The optimum concentration ratio of 3 wt. ‰ was identified to achieve the best electric performance. The maximum power density of 1,360 mW/m^2 and 911 mW/m^2 could be reached for Nb_2S_2C and Ta_2S_2C based TENG respectively. The influence of impact frequency and force was also studied. Moreover, the tribology evaluation revealed that the Ta_2S_2C/PDMS composite presented a lower coefficient of friction (COF) than Nb_2S_2C/PDMS composite. The as-made TENGs could perform as a sustainable power source for charging capacitors and driving small electronics, as well as perform as self-power sensors for the detection of human movements. In the future, the TMCC-TENG may play a useful role in human-machine interaction and large-scale energy harvesting for sustainable and renewable energy applications

CHAPTER 4 Flexible Triboelectric Nanogenerators Based on Hydrogel/g-C_3N_4 Composites for Energy Harvesting and Self-powered Sensing

4.1 Introduction

Based on the previous chapter, harvesting energies directly from our environment is a promising way to construct self-powered smart systems[165]. While TENG has demonstrated extraordinary advantages as energy suppliers and electronics in direct contact with the human body because they can be easily fabricated, cost-efficient, and versatile to adapt with other devices[166-168], except contact-separation mode TENG, single electrode TENGs are another type that have been widely adopted in applications. To facilitate the application of TENGs in devices in contact with the human body, materials that are human-friendly and transformable for both dielectrics and electrodes should be adopted. Although there is a wide range of candidates for flexible TENGs'

dielectric materials, bionic-skin electrode materials are very limited. Hydrogels can act as flexible electronic materials stably without damage under stretching, twisting, bending, or other external forces[102] and combine the advantages of environmental friendliness, transparency, low internal resistance, and tunable ionic conductivity with economic benefits. Electrical conductivity in hydrogels is usually achieved by incorporating a metal or carbon connection network inside the hydrogel, which might greatly reduce the stretchability of hydrogel. However, with the reduced mechanical reliability between hydrophobic polymers and hydrophilic hydrogels, charge transfer and device performance could be negatively affected. Single-electrode mode configuration is most frequently adopted when utilizing hydrogels as electrodes in TENGs because they are easy to fabricate and can be used for wearable devices. PVA, a water-soluble and biocompatible synthetic polymer, contains a large number of hydroxyl functional groups, which can be cross-linked to form hydrogels[169]. Among

different hydrogels, PVA is easy to fabricate, cost-benefit, biodegradable, and biocompatible, moreover, it is non-acidic and will neither alter the pH content of other materials nor cause any deterioration. PVA hydrogels can act as both electrodes and dielectric by adjusting the water content ratio. Pure PVA relies mostly on the water in it to conduct electricity, thus enhancing its conductivity can effectively enhance electrical performance for TENG using PVA composite as electrodes.

The incorporation of inorganic nanomaterials into hydrogel is one effective approach for fabricating conductive hydrogels and improving the composites' permittivity[11, 102] where the most common way is doping certain materials into pristine hydrogels, such as carbon nanotubes[79], electronegative halogens[83], metal nanowires or nanoparticles[9, 25], 2D materials, ferroelectric materials[82] (e.g., SrTiO3 or $BaTiO_3$[96, 170]). Doped PVA hydrogel can be developed as high-performance flexible bionic-skin electrodes as well as triboelectric layer dielectrics, which are novel, unique, and essential. Except for

TMCC, which we used in the previous chapter, the frequently mentioned 2D material, graphene, has been researched extensively. With a similar molecular structure as graphene, graphitic carbon nitride (g-C_3N_4) is a light-sensitive semiconductor, and its rich nitrogen element is susceptible to losing electrons. Particularly, g-C_3N_4 has salient features and promising applications in hydrogen evolution[99], photocatalytic degradation, gas sensors[122], antibacterial structures[123], and microwave absorbers[124]. Pure g-C_3N_4 nanosheets[171] have demonstrated attractive functionalities owing to their photo absorption characteristics[172], bio-friendly nature[173], and metal-free semiconductor properties[174]. Hence, human-friendly, and multi-functional TENGs with enhanced properties could be obtained by properly designing and integrating g-C_3N_4 into hydrogels. To the best of our knowledge, there is no such work incorporating g-C_3N_4 into hydrogels for TENGs currently.

Herein, we innovatively developed a conductive hydrogel based on PVA doped with g-C_3N_4, and prepared g-C_3N_4/PVA hydrogel TENG for the first time. A suitable amount of g-C_3N_4 (i.e. 2.7 wt. %) could increase the hydrogel's conductivity and hence enhance the triboelectric performance of g-C_3N_4/PVA hydrogel TENG, which reached an optimum electrical performance in open-circuit voltage (*Voc*) of 80 V, short-circuit current (*Isc*) of 2.5 μA, and charge transfer amount (*Qsc*) of 28 nC. Moreover, the electrical performance of dehydrated g-C_3N_4/PVA hydrogel TENG can recover up to 80% of its pristine state after soaking in water, showing great recyclability and sustainability. As it is non-toxic and non-irritating, it could be attached directly to different parts of the human body. Therefore, we utilized it as electronic skin and investigated its application as a motion detector, monitoring the range of human movements, such as elbow rotation, and wrist/knee/finger bending angles. Simultaneously, we tested its capabilities as a human biomechanical energy harvester

by scavenging behaviors like clapping and stepping. To further enhance the performance of the hydrogel-based TENG, different morphologies including discoid flake shape, tube, and spiral shape were fabricated and evaluated in either single electrode or contact separation mode. The simple and cost-effective preparation process can provide promising potential for integrating g-C_3N_4 into other biodegradable or sustainable materials and expanding their related hydrogel TENGs in wearable application fields.

4.2 Experimental Section

4.2.1 Materials

Poly (vinyl alcohol) 0588 (PVA, low viscosity, alcoholysis degree 87.0–89.0 mol mol^{-1}) was supplied by Shanghai Aladdin Biochemical Technology Co., Ltd. Boric acid (H_3BO_3) powder (≥99%), gelatin, glycerin (99.6%, ACS reagent), $ZnCl_2$, LiCl, and

absolute alcohol (≥99.5%, ACS reagent) were purchased from Sigma-Aldrich. Nitrogen-doped multiwall carbon nanotubes were purchased from Nanjing XFNANO Materials Tech Co., Ltd (China). Polytetrafluoroethylene film (PTFE, 0.15 mm) was bought from Shanghai Dongmeng Industrial Co., Ltd. Polydimethylsiloxane (PDMS, SYLGARD 184 Silicone Elastomer kit) was purchased from Dow Corning Co., Ltd. All the materials were used as received without further purification. Enamelled Copper (Cu) wire and Aluminum foil were bought from Dongguan Yishengxing Copper and Aluminum Materials Co., Ltd., China. Copper/nickel-coated polyester fabric (CNF) applied as the conductive fabric was bought from the 3M company. Silicon tube was bought from a local company and was cleaned with deionized water extensively before use.

4.2.2 Synthesis of g-C_3N_4

The preparation of g-C_3N_4 material was based on the method of classical high-temperature calcination. 10.0 g of melamine ($C_3H_6N_6$, 99% purity) raw material powder was placed in a quartz tube furnace, heated up to 650 ℃ from room temperature at a heating rate of 8 ℃ per minute, and kept at this temperature for over 12 hours in a nitrogen protective atmosphere. After the reaction was completed, the oven was switched off and the powders were cooled down to room temperature. Subsequently, the as-made initial pale-yellow powders were grounded and rinsed with deionized water, filtered, and squeezed in a mortar to obtain comparatively pure g-C_3N_4. Finally, the g-C_3N_4 powders were crushed in a mortar, ultrasonically vibrated for more than six hours, freeze-dried for 24 hours, and then dried in a vacuum drier overnight at the temperature of 60 ℃.

4.2.3 Fabrication of doped PVA Hydrogel TENG

The fabrication process for the PVA hydrogels was based on chemical crosslinking. Firstly, the aqueous PVA solution (10 wt. %) was prepared by dissolving PVA powders (10 g) in 90 mL of deionized water for 12 hours with magnetic stirring until all the granulates were dissolved[175]. Simultaneously, the boric acid powders were also agitated in deionized water for 12 hours until all particles were dissolved, generating an aqueous 8 wt. % boric acid solution. Then, the PVA solution was divided into equal parts, and one part was mixed with the boric acid to form a pristine PVA hydrogel, whereas the other parts were mixed with different amounts of g-C_3N_4 dopants in varied weight ratios, as well as other dopants including $ZnCl_2$, LiCl, gelatin, glycerin, carbon nanotubes. Afterward, the mixed PVA solutions were ultrasonically vibrated for 2 hours to ensure an even and thorough distribution of the dopants. Finally, the doped PVA solutions were gradually mixed with the crosslinking agent boric acid solution while continuously stirring.

Following this, the triboelectric nanogenerator architecture was sandwiched between PDMS materials on top and bottom and the hydrogel layer was contained inside the PDMS. The PDMS gels were fabricated by mixing the elastomer and the curing agent with a ratio of 10:1, stirring for 20 min, and then vacuum-pumping to eliminate air bubbles. For the bottom layer, the PDMS gel was transferred to a 3 cm diameter Petri dish with approximately 1 mm thickness and then stored in a constant temperature oven at 60 ℃ for 2 hours. After full solidification of the PDMS gel, a conductive aluminum wire was attached to the center of the bottom PDMS layer to link the external devices to the generated fix sized doped PVA hydrogel. The top layer PDMS was then put into the model using the same PDMS gel transferred onto the solid bottom PDMS and hydrogel and then exposed at the same cure process as the bottom part, to make sure that the hydrogel core was fully enfolded and sealed with PDMS. As weak durability via water loss is the main disadvantage of hydrogel, by optimizing the sealing

of PDMS, the water loss rate can be lowered and the hydrogel TENG can be kept for dozens of days with consistent output.

4.2.4 Characterization and Measurements

A universal tensile testing machine (Instron 4411) equipped with a 5 kN load cell was adopted to measure the mechanical properties while stretching. A scanning electron microscope (TESCAN VEGA3) operating at 20 kV was employed to investigate the morphology of the fabricated TENGs. The output voltage signal was collected by a Keysight DSO-X3014A oscilloscope and the open-circuit voltage and short-circuit current were measured using an electrometer (Keithley 6514). The output performance under impacting/releasing was evaluated by utilizing a Keyboard Life Tester (ZX-A03) Zhongxinda Shenzhen. Fourier-transform infrared spectroscopy (FTIR) was performed using Hitachi UH5300. UV-vis absorption spectra were recorded with a Hitachi UH5300 spectrometer. Impedance of hydrogel was measured by Keithley 2401, and

capacitance was measured by LCR-6300. The SEM images were taken by device Hitachi TM-3000, Japan. XPS spectra were recorded on an ESCALAB210 spectrometer.

4.3 Results and Discussion

4.3.1 Fabrication and Characterization

The PVA hydrogel was synthesized by chemical crosslinking (Figure 1a). A boracic acid solution of 8 wt. % was added to the 10 wt. % PVA solution to form a crosslinked soft solid. Additionally, doped PVA hydrogels were fabricated by adding g-C_3N_4 and other dopants (including $ZnCl_2$ powder, LiCl powder, and glycerin) to the aqueous PVA solution (Figure 4.1a) and mixing it with the boric acid solution. Crosslinking is only initiated after adding boric acid, which showed that the dopants could not crosslink the PVA to form a hydrogel and that the crosslinking agent was mainly boric acid.

Moreover, the pristine PVA hydrogel also exhibited great flexibility as it could be stretched to 15 folds of its original length (2 cm) (Figure 4.1b) and demonstrated good self-healing capability within 15 minutes (Figure 4.1c). Besides conventional disk plate TENG architecture, under the same design and mechanism, we also fabricated tube hydrogel TENG, where we replaced polydimethylsiloxane (PDMS) with a 2 mm inner diameter silicon tube and injected dopant hydrogel into the inner core of the tube, and then spiraled the tube into a disc. Both straight and helix tube TENGs had been evaluated.

Figure 4.1d showed the SEM images of pure PVA hydrogel and g-C_3N_4/PVA hydrogel. From the SEM results, g-C_3N_4 particles are uniformly dispersed into the PVA matrix, and Figure 4.1e shows that the corresponding EDS mapping images also confirm the uniform existence of N elements in g-C_3N_4, indicating that g-C_3N_4/PVA hydrogel was successfully prepared. FTIR of g-C_3N_4/PVA hydrogel was presented in Figure 4.1f.

The typical peaks at around 1081 and 1713 cm^{-1} in g-C_3N_4/PVA hydrogel can be assigned to C=O carbonyl stretching and C-O stretching of acetyl groups in the structure of PVA. In addition, two obvious absorption peaks located at around 1420 and 1244 cm^{-1} can be observed in both g-C_3N_4/PVA hydrogel and g-C_3N_4 powder, which can be associated with C–N stretching vibrations and C=N stretching vibrations of the CN aromatic repeating unit[176], and the strong peak observed at 807 cm^{-1} was attributed to the breathing mode of s-triazine units[177], identifying the existence of g-C_3N_4 in the composite.

Moreover, the XPS survey of g-C_3N_4/PVA hydrogel (Figure 4.2) shows that C1s and O1s could be observed, while N1s is not significant due to the low doped concentration of g-C_3N_4 in the composite. Furthermore, the XPS spectrum of N1s is used to confirm the existence of low concentration g-C_3N_4 in g-C_3N_4/PVA hydrogel.

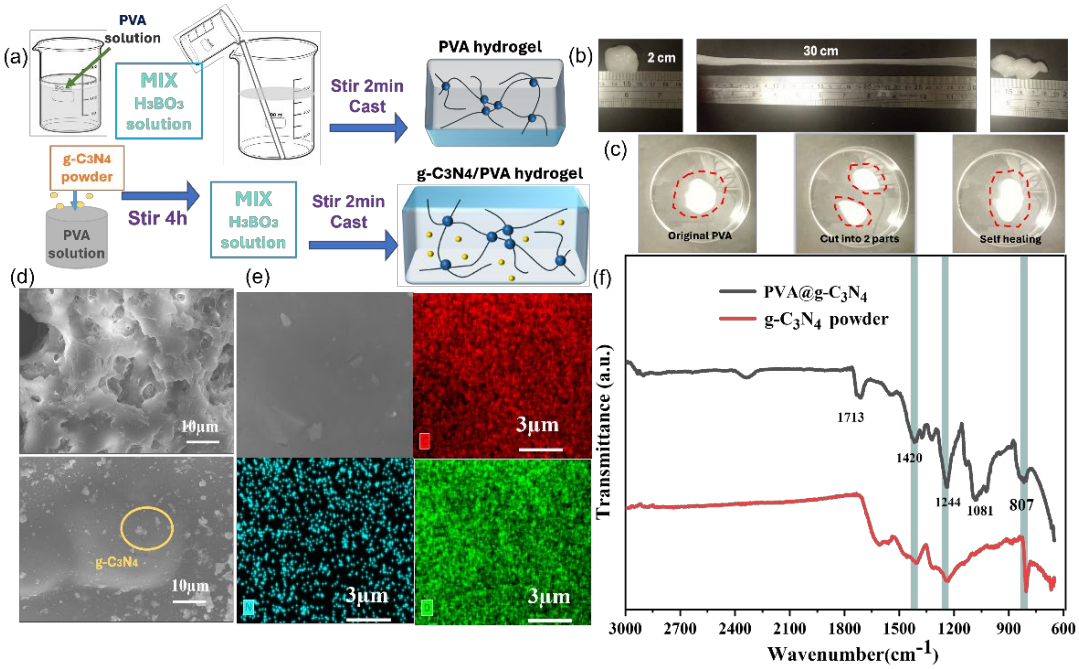

Figure 4.1 (a) Schematic routes for the preparation of the PVA hydrogel and g-C_3N_4/PVA hydrogel. (b) Photographs of PVA hydrogels in different deformation states, such as original, elongated, and twisted. (c) Photographs of PVA hydrogels depicting the self-healing capability: original state, cut in half, automatic recovery within 15 minutes. (d) SEM of pure PVA hydrogel and g-C_3N_4/PVA hydrogel. (e) EDS mapping of g-C_3N_4/PVA showing the existence of C, N, and O elements. (f) FTIR spectra of g-C_3N_4/PVA hydrogel and pure g-C_3N_4 powder.

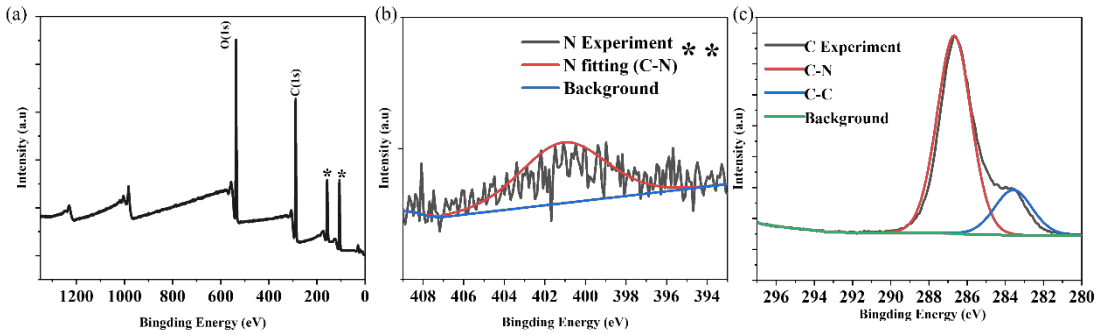

Figure 4.2 (a) XPS survey spectra of g-C_3N_4 dopant PVA hydrogel (The additional 2 peaks marked * originated from the glass substrate used in XPS measurements) (b) High-resolution XPS spectrum showing the binding energy of N electrons. (c) XPS spectrum showing the binding energy of C-C and C-N.

4.3.2 Mechanism of TENG

In single-electrode mode hydrogel TENG, g-C_3N_4/PVA hydrogel (as an electrode) is encapsulated into a silicon tube (as a triboelectric layer). The working mechanism of g-C_3N_4/PVA hydrogel TENG can be seen in Figure 4.3. When a substrate is away from the TENG, there is no electric potential between them. As soon as the substrate contacts TENG, electrons are injected from substrate to silicon tube, leaving substrate positively

charged and silicon tube negatively charged (Figure 4.3a(i)). When the substrate moves away from the TENG, an electrical potential difference is established because of the dipole moment, and positive ions in the hydrogel are induced by the unscreened negative charges on silicon tube, emerging from the upper interface between silicon tube and hydrogel electrode. Meanwhile, an electrical double layer is formed at the bottom hydrogel at interface with the conductive wire connecting the hydrogel to the ground (through resistor or electrometer), with the same number of negative ions. To maintain the double layer, electrons flow from the conductive wire to the ground through external circuit, generating a negative current signal (Figure 4.3a(ii)). So long the substrate is far enough from the TENG, all the charges (positive/negative) and ions (positive/negative) are in an electrostatic equilibrium state (Figure 4.3a(iii)). Once the substrate approaches the TENG again, electrons start to transfer back from the ground to hydrogel to neutralize the positive charges in the electrical double layer, producing

a positive current signal (Figure 4.3a(iv)). Thus, AC electric signal is generated upon continuous contact-separation motion between the substrate and the TENG[10, 14, 20, 78].

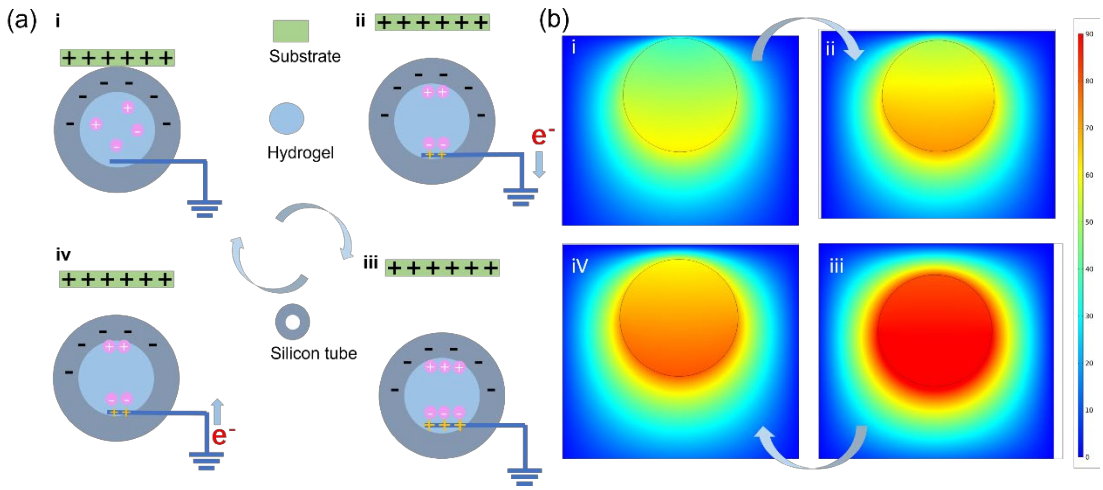

Figure 4.3 The working mechanism of the hydrogel-TENG (a) Schematic structure and working principle of the single-electrode mode hydrogel-based TENG for energy harvesting and (b) demonstration of electrical potential distribution by COMSOL software simulation.

4.3.3 Different Substrate Materials and Dopant Concentrations

We studied the electrical performance of the fabricated hydrogel-based TENGs in single-electrode mode using four different substrate materials, including Kapton, PTFE, conductive Cu/Ni fabric, and copper coil. In terms of open-circuit voltage (*Voc*) value, Kapton has the highest value of 45 V, followed by PTFE of 38 V, conductive Cu/Ni fabric of 28 V, and lowest 24 V for copper coil (Figure 4.4a). Similarly, short-circuit current (*Isc*) values from high to low are 0.75 μA for Kapton, 0.65 μA for PTFE, 0.4 μA for conductive Cu/Ni fabric, and 0.25 μA copper coil (Figure 4.4b). Charge transfer value (*Qsc*) also followed the same sequence of Kapton (20 nC), PTFE (16 nC), conductive Cu/Ni fabric (10 nC), and copper coil (6 nC) (Figure 4.4c).

For the g-C_3N_4 doped hydrogels, the effects of the 2D material doping concentration ranging from 0.4 wt. % to 5.7 wt. % were studied to explore the optimum concentration for achieving the highest output performance, where 2.7 wt % was the best. The suitable amounts of added g-C_3N_4 will initially increase the conductivity of the g-C_3N_4/PVA

hydrogel composite, thereby increasing the electric output of g-C_3N_4/PVA hydrogel TENG. It may be because the introduction of semiconducting g-C_3N_4 helps in the transport of charges or ions in the g-C_3N_4/PVA hydrogel[102]. However, when increasing dopant concentrations, the agglomeration of g-C_3N_4 particles would significantly inhibit ion transport in the hydrogel and increase the resistance. This is reflected by the optimum dopant concentration of 2.7 wt. % that produced the highest output performance with open-circuit voltage (*Voc*) of 80 V, short-circuit current (*Isc*) of 2.5 μA, and charge transfer (*Qsc*) amount of 28 nC, when contacting with a PTFE film (Figure 4.4d-f).

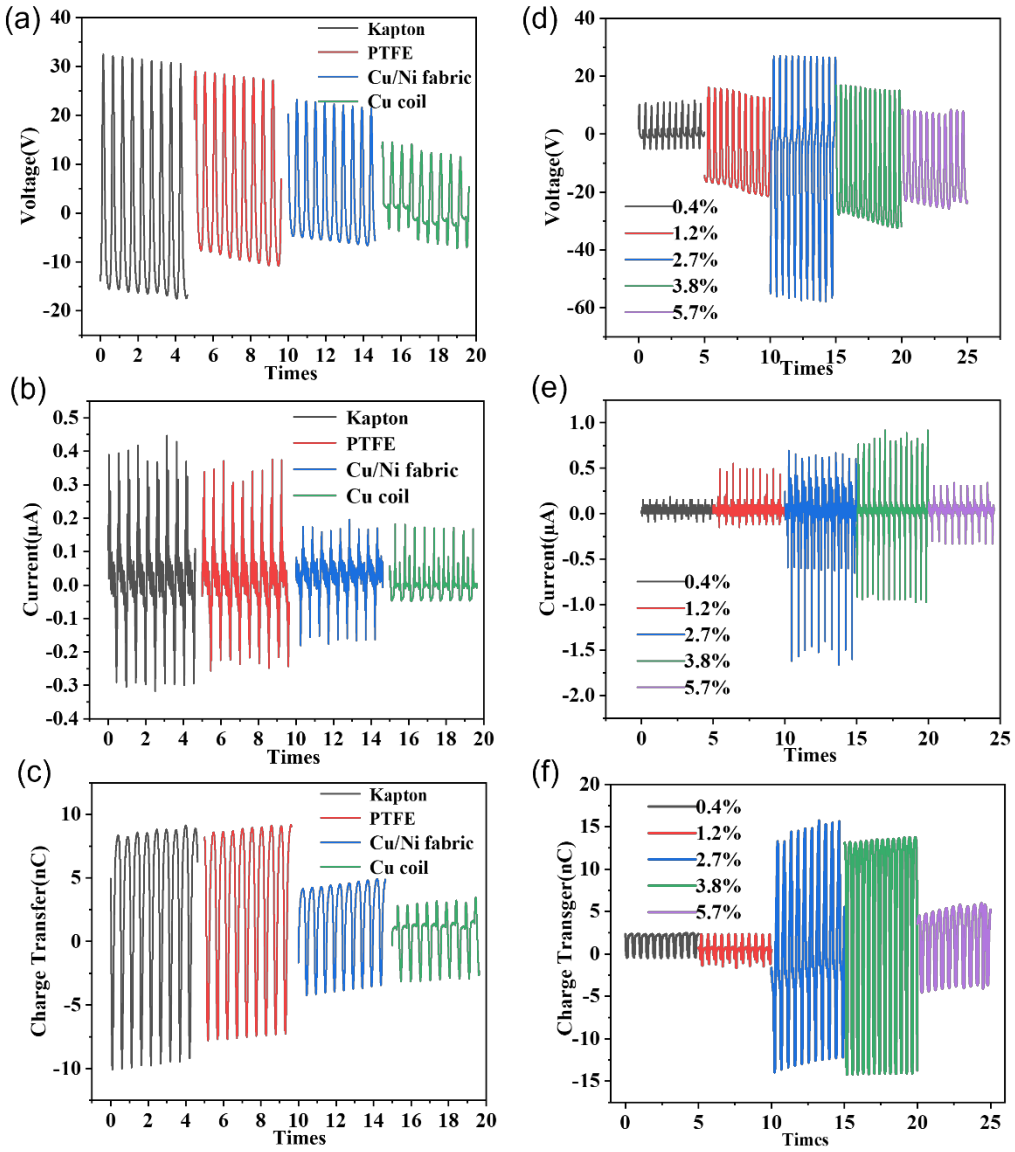

Figure 4.4 Demonstration of the hydrogel TENG for energy harvesting at an impact force of 30 N and frequency of 2 Hz (a) Open circuit voltage (b) Short circuit current (c) Charge Transfer of single electrode TENG of different external substrate materials of Kapton, PTFE, Copper-nickel conductive fabric, copper coil (Sort by descending

order of the electrical output performance). (d) Open circuit voltage (e) Short circuit current (f) Charge Transfer of single electrode hydrogel TENG at different concentrations of g-C_3N_4 by weight ratios (g-C_3N_4: PVA) of 0.4 wt. %, 1.2 wt. %, 2.7 wt. %, 3.8 wt. %, and 5.7 wt. %, respectively.

For systematical study as shown in Figure 4.5, firstly we adjust the concentration with 0 wt. %, 0.4 wt. %, 4 wt. %, 28 wt. %, and 50 wt. % respectively. In this initial test, we found that the 4 wt. % showed a maximum at voltage, current, and charge. Then we narrowed the scope to measure the area between 4 wt. % to 28 wt. %, and the concentrations of 7 wt. %, 14 wt. %, 20 wt. %, and 25 wt. % showed output in descending order. After that we focus on refining the concentration scope of 0.4 wt. % to 4 wt. % with concentration s of 0.4 wt. %, 1.2 wt. %, 2.7 wt. %, 3.8 wt. %, 5.7 wt. %,

where the concentration 2.7 wt. % had the maximum output and was used in the experiments afterward.

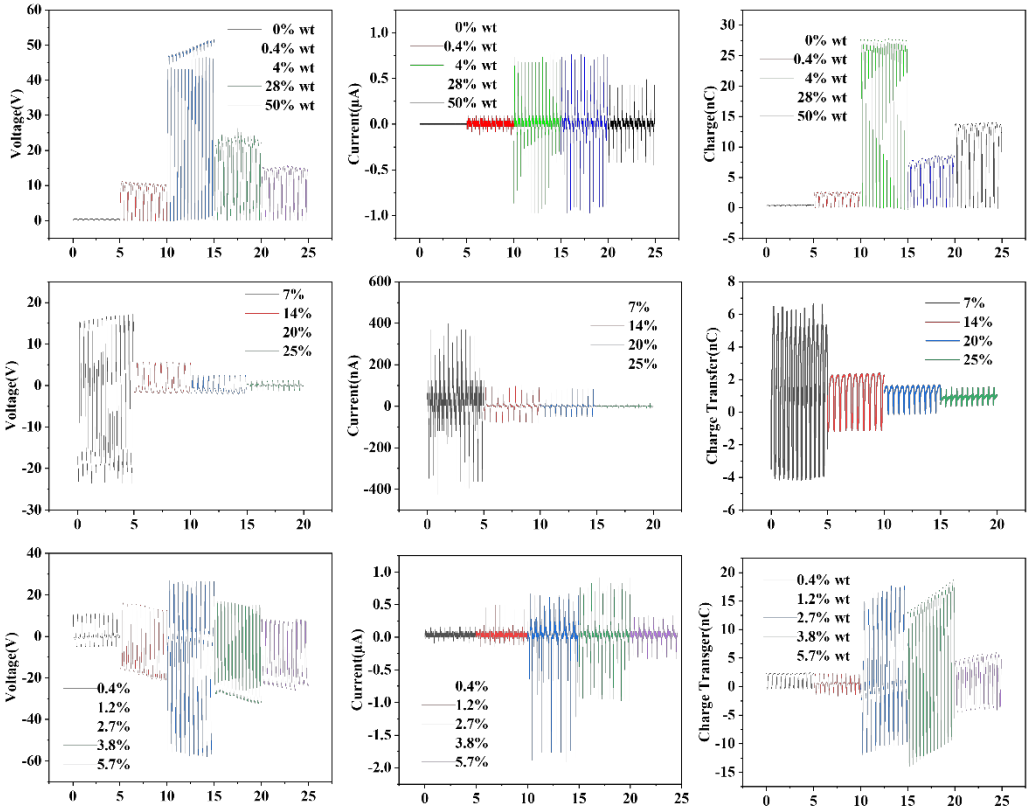

Figure 4.5 (a) Open circuit voltage (b) Short circuit current (c) Charge transfer of the concentration from 0 to 50 wt. %. (d) Open circuit voltage (e) Short circuit current (f) Charge transfer of the concentration from 7 wt. % to 25 wt. %. (g) Open circuit voltage (h) Short circuit current (i) Charge transfer of the concentration from 0.4 wt. % to 5.7 wt. %

4.3.4 Influence of External Factors

During practical applications, the impact force and frequency will certainly vary, and thus the influences of single-electrode hydrogel TENG under different forces and frequencies are also important for both academic and practical purposes. Therefore, we measured electrical performance in dependence on both impact force and frequency (Figure 4.6). At a fixed frequency of 3 Hz, when the impact force was increased from 20 N to 100 N, the voltage was increased from 30 V to 40 V and then stayed almost constant when the impact force further increased to 300 N (Figure 4.6a). Meanwhile, the current was increased from 0.9 μA to 1.5 μA and then to 2.5 μA upon the impact force increasing (Figure 4.6b). This increase in voltage and current with impact force is possibly profiting from the hydrogel's flexibility and elasticity resilience, resulting in intimate contact between the hydrogel and dielectric polymer during loading. In terms of the influence of frequency on the electrical performance of the g-C_3N_4/PVA

hydrogel-based single electrode TENG, the voltage was increased gradually from 70 V to 120 V (Figure 4.6c), while the current was increased gradually from about 1 μA to 8 μA as the frequency was increased from 1 Hz to 7 Hz at a force of 200 N (Figure 4.6d). A higher impact frequency can stimulate electrons in a shorter time which may result in an increased current output[151]. Additionally, a larger magnitude of applied impact force could attribute to more intimate contact for enhanced electrical output of the TENG.

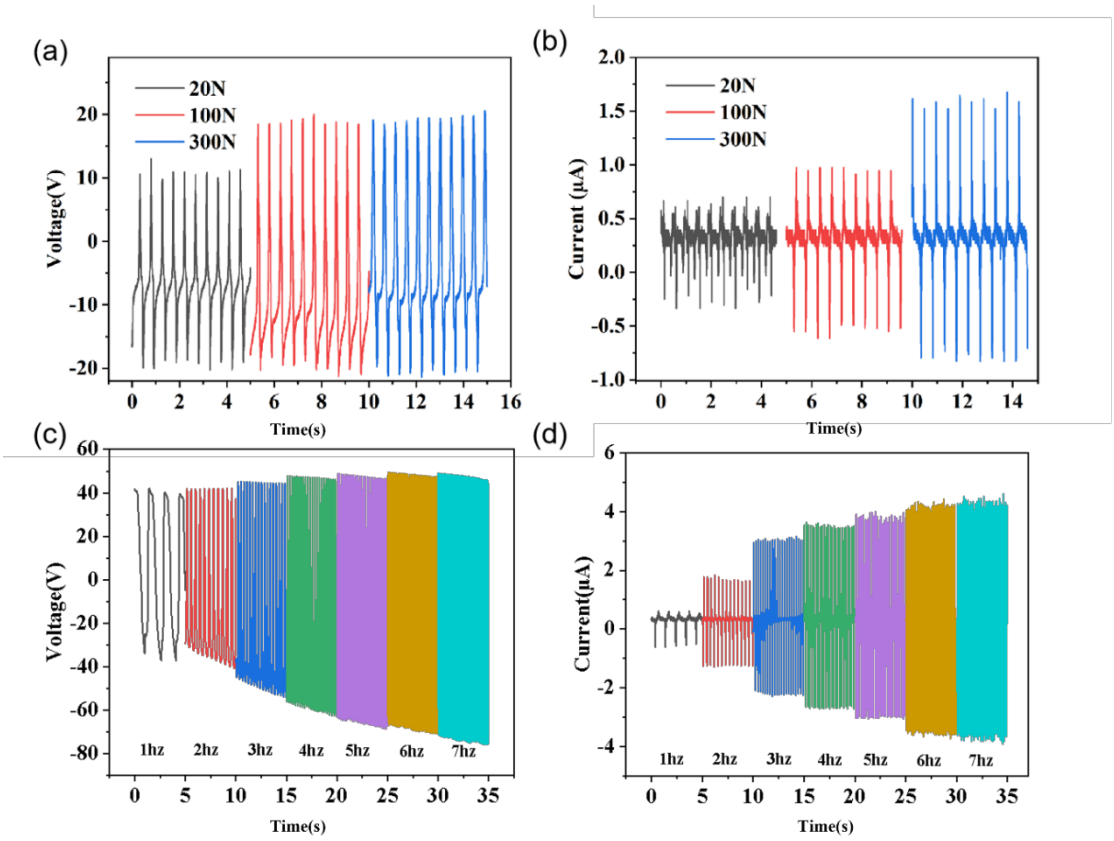

Figure 4.6 Performance of 2.7 wt. % g-C_3N_4/PVA hydrogel TENG (a) Open circuit voltage (b) Short circuit current at different impact forces of 20 N, 100 N, and 300 N, respectively. (c) Open circuit voltage (d) Short circuit current at different frequencies from 1 Hz to 7 Hz.

4.3.5 Mechanical Property and Power Density

Previous studies showed that dopants in hydrogel can significantly change the physical properties such as MXene[102], and LiCl[175]. Tensile tests were then performed to evaluate

the mechanical properties of PVA hydrogel with dopants $ZnCl_2$, LiCl, and g-C_3N_4, separately. As shown in Figure 4.7a, PVC hydrogel showed ultimate tensile strength at break of 1 N with g-C_3N_4, 1 N with pure PVC, 9 N with $ZnCl_2$, 10.5 N with LiCl, respectively (at a concentration of 2 wt. % and with the same size of 10×10 mm^2). G-C_3N_4 dopant hydrogel showed insignificant improvement in the elastic property of PVA hydrogel. Interestingly, other dopants such as muriate could increase tensile strength. By connecting with different capacitors, the charging capacity of g-C_3N_4/PVA hydrogel TENG with an optimum dopant concentration of 2.7 wt. % was also evaluated (Figure 4.7b). The charging rates of different capacitors were calculated as 35 mV/s for 1.5 μF, 20 mV/s for 4.7 μF, 16 mV/s for 22 μF, and 4.5 mV/s for 100 μF, respectively. Different resistors from 1 kΩ to 1GΩ were also connected to measure the electric output current at a fixed frequency of 3 Hz and impact force of 40 Hz. Based on the measurements of $P=I^2R/S$ (where P is the power density, I is current, R is the resistance value, and S is

the contact area), the power density can be calculated that the pure PVA hydrogel TENG only showed a maximum power density of 10 mW/m^2 at a load resistance of 100 MΩ (Figure 4.7c), while the optimal power density of g-C_3N_4/PVA hydrogel TENG reached a maximum value of 45 mW/m^2 at a load resistance of 10 kΩ (Figure 4.7d). The long-term cycling durability of this g-C_3N_4/PVA hydrogel TENG has also been demonstrated. After 9,200 continuous contact-separation strikes, it is hard to observe any significant change in the amplitude of the voltage output signals, indicating outstanding electrical output durability (Figure 4.7e). Although hydrogels can easily dehydrate when exposed to air, as our TENG is sealed with PDMS, it could stay effective for a long time. Daily electrical testing for seven consecutive days resulted in only a small decrease in current signals, indicating that our TENG has good environmental tolerance (Figure 4.7f). In addition, the recyclability of g-C_3N_4/PVA hydrogel TENG is also investigated. A major problem with hydrogels is that they tend to dehydrate and lose their flexibility

and conductivity. Our dehydrated g-C_3N_4/PVA hydrogel composite can be put into pure water to reabsorb the water to recover the structure of the original hydrogels. Figure 4.7g shows the comparison of the electrical properties of original and recreated g-C_3N_4/PVA hydrogel TENG after 12 hours of water absorption. Compared with the fresh hydrogel TENG under the same circumstances, the recreated g-C_3N_4/PVA hydrogel TENG just suffered a slight decrease in voltage signal, indicating good recyclability and sustainability.

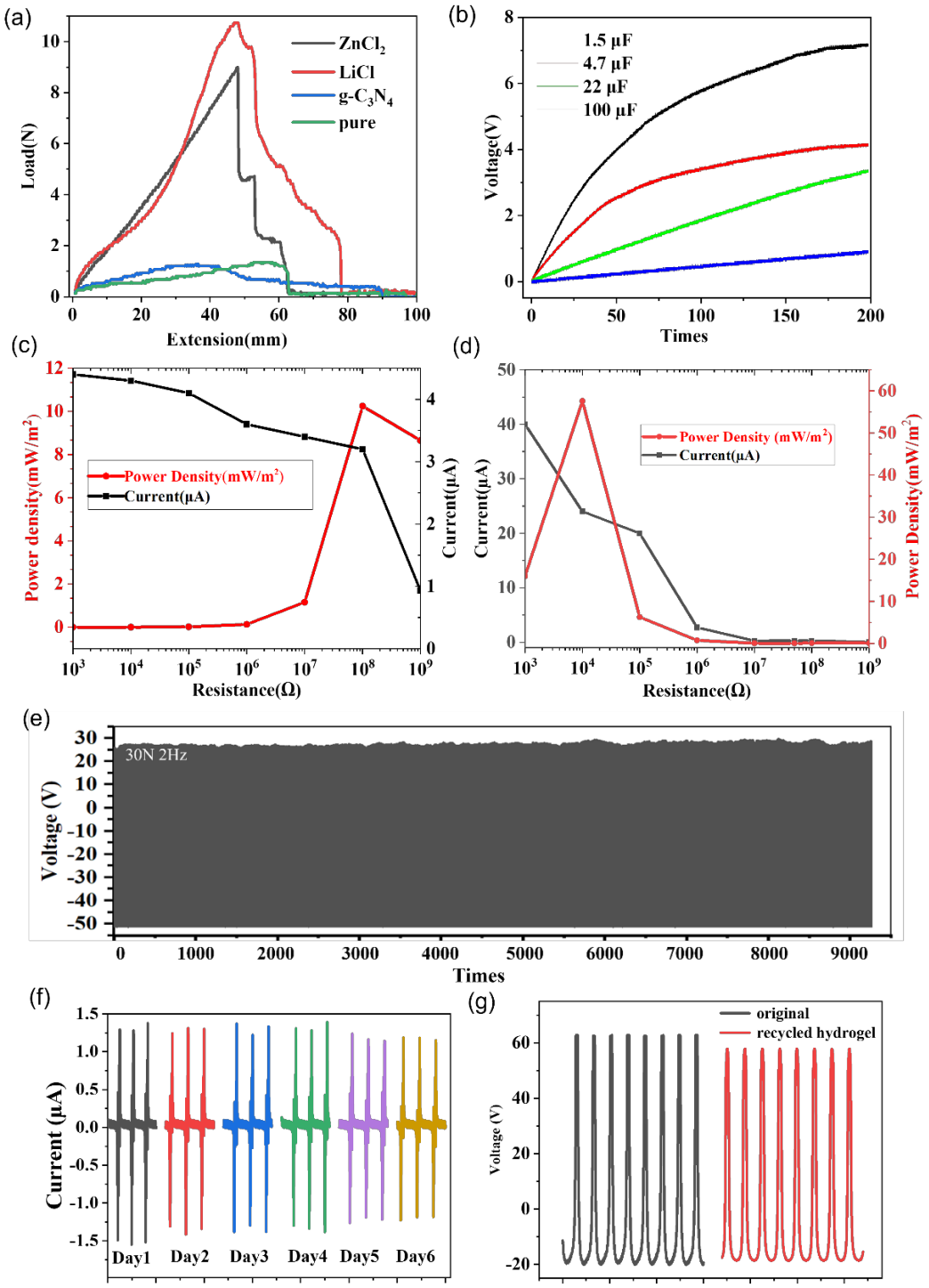

Figure 4.7 (a) Mechanical property of PVA hydrogel with different dopants. (b)

Charging behavior of the g-C_3N_4/PVA hydrogel TENG with capacitors of 1.5 μF, 4.7

μF, 22 μF, and 100 μF under the same working circumstances. (c) The relationship between short-circuit current and calculated power densities versus the resistance of the external loads of PVA hydrogels. (d) Dependence of short-circuit current and calculated power densities under different resistances of the external loads of 2.7 wt. % g-C_3N_4/PVA hydrogel TENG under the same circumstances. (e) Durability test of g-C_3N_4/PVA hydrogel TENG for a constant strike of 9,200 cycles. (f) Daily measurements for 6 consecutive days. (g) The electrical performance of original g-C_3N_4/PVA hydrogel TENG and recycled TENG.

4.3.6 Different Structural Morphologies

One great feature of PVA is that it can act both as an electrode or tribo-positive material. According to the structural figure-of-merit[178] for TENGs, the output of single-electrode TENGs is much lower than that of equal-sized two-electrode TENGs under the same

measurement conditions because of limited transfer charges and suppressed built-in voltage. To test the electrical performance of the hydrogel-based TENG in two different electrode modes, we have designed and fabricated two types of hydrogel-TENGs, as shown in Figure 4.8a. One is a single electrode mode TENG with the inner core made of PVA hydrogel with an inner diameter of 5 mm and an outer silicone tube with a diameter of 7 mm acting as tribo-negative layer. We compared this with a double electrode hydrogel TENG, where a bare copper wire is added to the inner core to conduct electricity, and a layer of copper/nickel-coated polyester fabric (CNF) is wrapped and pasted on the outside of the silicone tube as negative electrode so that the PVA and the silicon form a TENG in contact separation mode. As shown in Figure 4.8b-d, under the same conditions, the double-electrode hydrogel-based TENG produced four times of voltage, seven times of current, and three times of charge transfer as compared to the single-electrode hydrogel-based TENG. When used as a

positive electrode material, the water content ratio of PVA should not be too high. As easy dehydration is also a major weakness for hydrogels, adding glycerin can appropriately slow down the dehydration rate. Mechanical deformations such as pressing, enwinding, bending, knotting, and stretching could be easily performed with the tube PVA TENGs, demonstrating their excellent flexibility.

Furthermore, to expand its application potential as a useful power source, we have also fabricated the hydrogel-based TENG into a spiral discoid shape (Figure 4.8e), where the output during gentle slapping of the g-C_3N_4/PVA hydrogel TENG also increased more than two times as compared to pure PVA, including the voltage from 13 V to 25 V (Figure 4.8f), the current from 0.4 μA to 1.0 μA (Figure 4.8g), and the charge transfer from 5 nC to 12 nC (Figure 4.8h). This spiral shape can expand the contact area between the hydrogel and the silicone as compared to the simple sandwich flake shape hydrogel TENG.

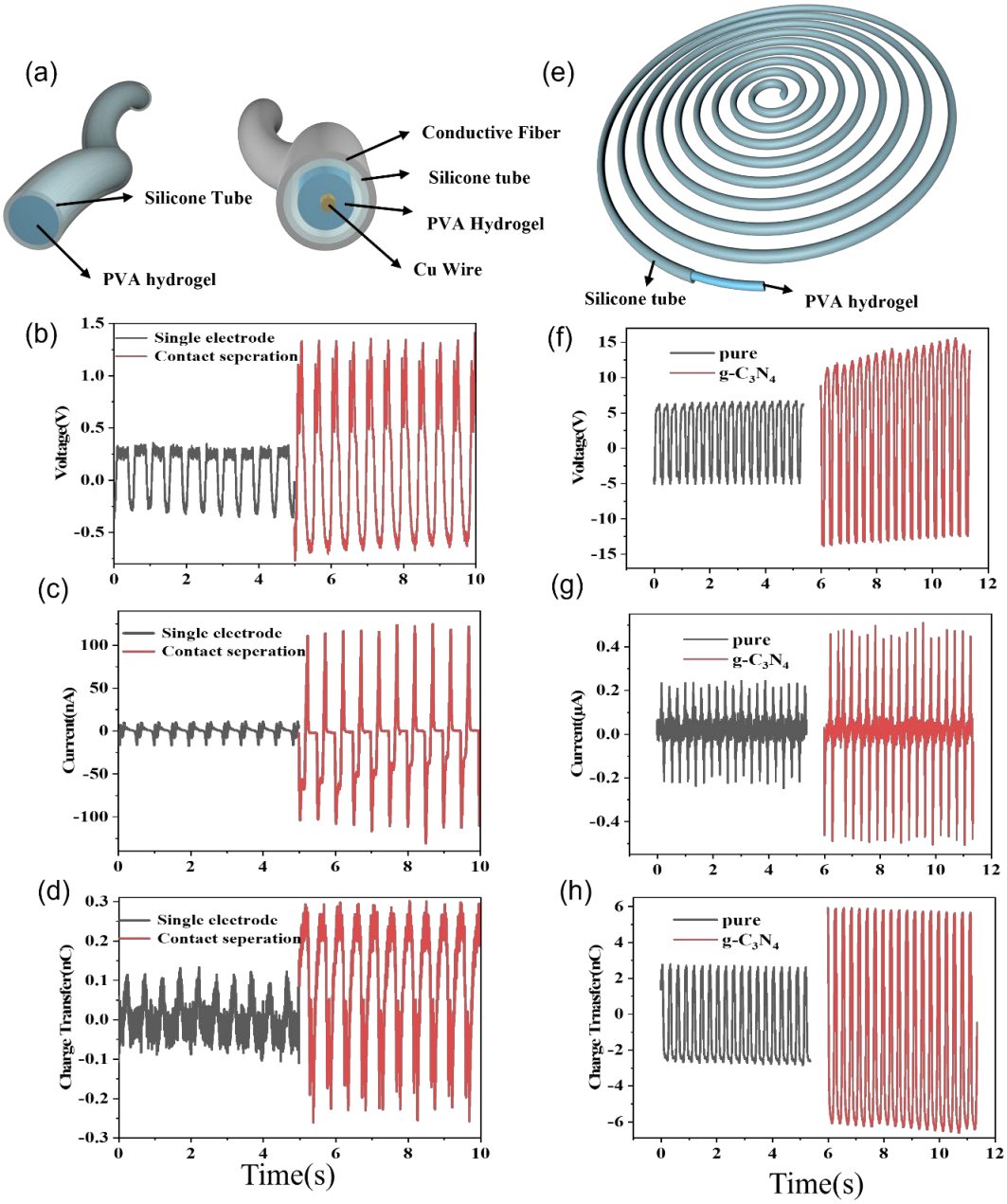

Figure 4.8 (a) Morphology for tube hydrogel TENG (3 cm) with pure PVA as electrode (single electrode mode) and positive tribo-layer (contact separation mode). Comparison of their (b) open circuit voltage, (c) short circuit current, and (d) charge transfer by

simple slapping. (e) Morphology for the single electrode tube hydrogel TENG (30 cm) fabricated into spiral and electrical output comparison with pure PVA TENG and g-C_3N_4/PVA hydrogel TENG of (f) open circuit voltage, (g) short circuit current, (h) charge transfer, by simple slapping.

Comparison of some hydrogel-TENGs is listed in Table 2 below.

Table 2. Comparison of other works for hydrogel-TENGs

Hydrogel Materials	Size (cm^2)	V (V)	I (μA)	Power density (mW/m^2)	Ref.
catechol-chitosan-diatom	3 × 3	110	3.8	29.8	[179]
PAM-BIS-cyclodextrin	2.5×2.5	95	10	0.64	[180]
PAM-graphene hydrogel	1.5×1.5	40	-	-	[181]
Starch-PDMS elastomer hydrogel	-	25	2	-	[182]
Polyacrylamide/montmorillonite/carbon nanotube	0.12	86.4	1.1	41.2	[183]
Egg white hydrogel	-	20	-	-	[184]
Cellulose-PVA hydrogel	-	41	0.5	-	[67]
PAM-LiCl hydrogel	4	75	3.6	41	[185]
Bacterial Cellulose/ZnO	-	57.6	5.78	42	[186]
PAM/Silk	-	12	0.4	-	[187]
PVA/HEC	-	0.151	-	-	[188]
Gelatin-PAA-NaCl hydrogel	6	22	0.4	29	[189]
PVA+g-C_3N_4	4.9	80	2.5	45	This work

4.3.7 Applications

Finally, we have also measured the output voltages generated by the TENGs through different body movements. So far, we have produced different morphologies from linear to three-dimensional (tube, sandwich flake, and spiral) structures, showing the great formability and flexibility of this PVA hydrogel TENG. Thus we can use different

shapes in different parts of the human body, such as a tube along the arm or, a flake at the palm or foot. The hollow fiber TENG with PVA hydrogel core is well suited for body motion monitoring sensors based on its proportional relationship of open circuit voltage to the corresponding stretch length, resulting in a good response to different movements of the human body as well as its great biocompatibility and flexibility, which enables it to be fixed directly to human skin, it could present 45°, 90°, and 120° bending angles of the elbow into electrical signals (*Voc*) (Figure 4.9a-b), moreover it gives a stable signal to action changes, such as half-to-full bending of the wrist (Figure 4.9c) and finger (Figure 4.9d), as well as harvest biomechanical energy (Figure 4.9e-f). Especially, as g-C_3N_4/PVA hydrogel TENG device is self-insulating when completely enclosed, it can generate electricity in direct contact with the skin. The single-electrode hydrogel TENG can light up more than 38 LEDs connected in series by gentle hand slapping (Figure 4.9g) and can also power an electronic watch and a calculator with the

capacitors it charged (Figure 4.9h-i). The simple preparation methods, cost-effectiveness, and promising applications of g-C_3N_4/PVA hydrogel TENGs make them promise to expand for large-scale mass production in industrialization.

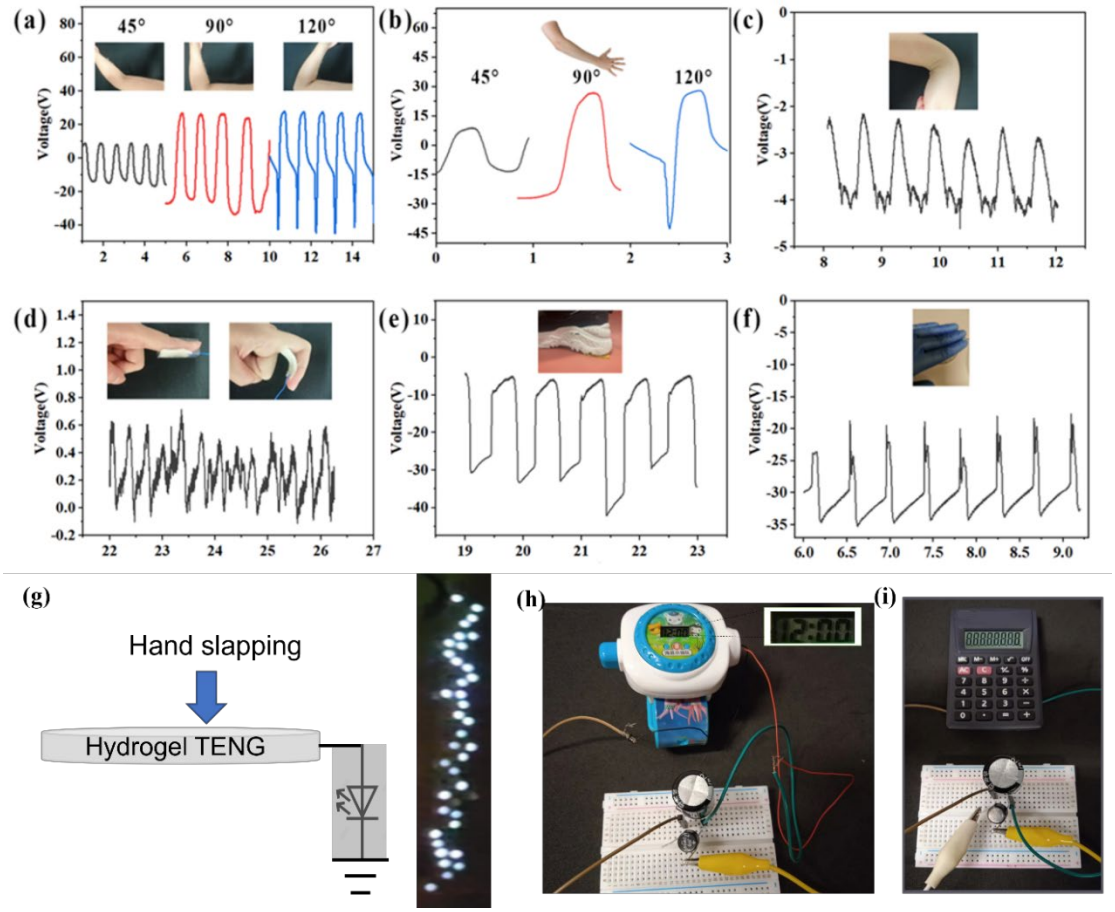

Figure 4.9 Output voltages generated by different stretched states and self-powered sensors for monitoring body movements (a) Output voltage signals of tube hydrogel-TENG in response to the elbow bend at 45°, 90°, and 120°. Voltage signals of the flake hydrogel-TENG in response to continuous bends of (b) elbow, (c) wrist, (d) finger, (e)

foot stepping (f) hand clapping. (g) Demonstration of g-C_3N_4/PVA hydrogel TENG light up 38 LEDs by gentle hand slapping. The photograph of a commercial (h) watch and (i) electrical calculator powered by a capacitor charged by hydrogel TENG.

4.4 Conclusions

In summary, flexible and stretchable triboelectric nanogenerators with dopant PVA hydrogel of g-C_3N_4 were first fabricated. An optimal doping concentration of g-C_3N_4 for the hydrogel TENGs was obtained as 2.7 wt. % with a maximum open-circuit voltage of 80 V, short-circuit current of 2.5 μA, and charge transfer of 28 nC, as well as power density with the maximum value of 45 mW/m^2 at a load resistance of 10 kΩ. The freestanding triboelectric materials for the hydrogel TENGs can be combined with materials including Kapton, PTFE, Cu coil, and Cu/Ni conductive fabric which showed great potential in low-frequency biomechanical energy harvesting. Other common

dopants including carbon nanotube, zinc chloride, and lithium chloride had also been evaluated because carbon nanotube could increase the conductivity, while muriate chloride could considerably raise the mechanical stretchability. The prepared TENG was flexible, stretchable, stable, and sensitive to versatile external mechanical stimuli such as stretching, compressing, twisting, and bending, as well as capable of harvesting energy from human motion for lighting up light-emitting diodes, charging commercial capacitors, powering electronic watch and scientific calculator. Besides, the properties of pristine PVA hydrogel such as conductivity, hygroscopicity, as well as the original electro-positivity enable it to be a good triboelectric material that can act as both electrode and dielectric positive tribo-layer. Owing to its non-toxic, non-irritating, highly flexible character, hydrogel-TENG can be further fabricated into electronic skin with functions of human motion detectors and energy harvesting for application. Different morphologies including discoid flake, tube shape, and innovative spiral shape

with PVA as either electrode (single electrode mode) or tribo-positive material (contact separation mode) have also been developed and evaluated. This work demonstrates the proposed composites' promising potential for versatile applications in biomechanical energy harvesting and self-powered human motion sensing.

CHAPTER 5 Wearable Triboelectric Nanogenerators Based on 2D Material-Graphitic Carbon Nitride (g-C_3N_4) Dopped Composites

5.1 Introduction

Recently, many research endeavors have been committed to the enhancement of the TENG's output performance. One major stream is to design and fabricate micro or nano architectures using ion etching process[75], such as photolithography[61], nanoimprinting lithography[76], laser interference[77], porous modification[78]. The other one is to improve the friction composites' permittivity[11] through doping certain materials into pristine triboelectric layers[14]. In practice, most of the doping is carried out in the electronegative dielectric medium, such as polydimethylsiloxane (PDMS)[60-63] whose pristine phase is liquid under normal circumstances. Compared with various preparation methods, electrospinning is a versatile[190], simple, economical, and accessible way to produce ultrathin fiber membranes with essential length, sufficient surface area, and

hierarchically intrinsic porosity comparatively. In past research, electrospinning has already been adopted as a suitable method in the field of energy harvesting for fabricating diverse nanofibrous surface[54] microstructures from economical materials, such as nylon (polyamide)[74], polyvinylidene fluoride (PVDF)[54-57], polytetrafluoroethylene (PTFE)[50, 58], ion gel[76, 85, 191], and so on. Nanofiber membranes feature lightweight, softness, and high porosity advantages and are superior to dense films or fabricated textiles with micron-sized pores in applications of TENGs. Herein, we adopted photosensitive g-C_3N_4 into electrospinning membrane PA_{66} to assemble a multifunctional TENG and enhanced twice the electric performance of TENG at a certain concentration with the micro-architecture composition of electropositive dielectric Polyamide (PA_{66} or $Nylon_{66}$). The prepared electrospinning membrane TENG could be used as flexible power-generating devices to scavenge the kinetic energy of human motion or flags to capture wind energy. The assembled TENG with 2 cm×2 cm

PA_{66} electrospinning membrane with doping g-C_3N_4 nanosheets can achieve more than 80 V of voltage and 45 mW/m^2 of power density, which was capable of lighting up 40 light-emitting diodes by gentle hand clapping. Our research could provide a useful approach for the fabrication and modification of wearable TENGs with customizable functionalities for applications.

5.2 Experimental Section

5.2.1 Materials

Melamine ($C_3H_6N_6$, 99% purity), Acetic acid, N, N-dimethylformamide (DMF, ≥99.8%, ACS reagent), formic acid (88−91%, ACS reagent), tetrahydrofuran (≥99.9%, ACS reagent), acetone (≥99.5%, ACS reagent), Ethanol, PVDF, PAN, polyimide (PI) were products of DIECKMANN. PDMS (SYLGARD 184 Silicone Elastomer kit) was purchased from Dow Corning Co, Ltd. Polyamide (PA_{66}) staple fiber was purchased

from Shandong Zhongxian Textile Technology Co, Ltd, China. Copper (Cu) wire and the Aluminum foil were bought from DongguaYishengxing Copper and Aluminum Materials Co, Ltd, China. Cu/Ni coated fabric was applied as the conductive fabric was purchased from 3M Corp. All reagents were used as received without further purification.

5.2.2 Synthesis of g-C_3N_4

Melamine ($C_3H_6N_6$, 99% purity) has been applied as raw materials to fabricate g-C_3N_4 by pyrolysis. Pure melamine ($C_3H_6N_6$, 99% purity) powder was first calcined in a tube furnace at 600 degrees Celsius (°C) for more than 8 hours at a heating rate of 5 °C per minute in a nitrogen atmosphere. Upon the furnace cooling to normal temperature, the synthesized powders were ground, washed with deionized water, then filtered and squeezed in a mortar to obtain comparatively pure g-C_3N_4, and finally dried in a vacuum drier under 50 °C[192]. Then, the g-C_3N_4 powder was crushed in a mortar[190] and added to

a small amount of alcohol to ultrasonic vibration for more than six hours[116], and then the alcohol was evaporated to make the powder as small as possible to be dispersed into a polymer solution. Because g-C_3N_4 is indiscerptible[173] in solvent formic acid and slightly soluble in water or a common organic solvent such as ethanol, the suspension solution of g-C_3N_4 increased the load capacity and made electrospinning less stable, which indirectly leads to agglomeration of g-C_3N_4 particles. So the upper concentration in the electrospinning membrane solution is limited to 0.7 wt. % of g-C_3N_4 according to the result of our experiments with ultrasonic time for dispersions over 12 hours.

5.2.3 Fabrication of the PA_{66} membrane

Given the above-mentioned insolubility problem, after several comparison experiments, we adopted the solution solvent for PA_{66} as 15% PA_{66} in 50% formic acid and 50% acetic acid, which has suitable volatility and less pungent smell. The g-C_3N_4 powder was mixed into the electrospinning membrane solution according to different

concentrations, and the dispersions of g-C_3N_4 and PA_{66} were prepared by ultrasonication overnight. Then the solutions were used for electrospinning at the voltage of 24 kV, drum rotating rate of 300 rpm, and flow rate of 2 ml/hour, with adding heater at 80 ℃ and dehumidifier for solutions with the dopant.

PA_{66} electrospinning membranes with g-C_3N_4 concentrations of 0.1 wt. % (low concentration) and 0.4 wt. % (high concentration), as well as pure PA_{66} membrane, were prepared because of the insolvability and solid-state of g-C_3N_4 powder. The maximum concentration limit in the experiment for electrospinning dispersions with dopant nanoparticles of graphitic carbon nitride was 0.7 wt. %, which is easily chapped and unable to fabricate.

5.2.4 Material characterization and performance measurement

Fourier transforms infrared (FTIR) absorption spectra were recorded on a spectrometer (Spectrum 100, Perkin Elmer). The SEM images were taken from Hitachi TM-3000

Tabletop Microscope. The cyclic contact-separation motion of TENG triboelectric performance measurements was realized by a life test machine (ZX-A03, Zhongxingda, Shenzhen) with a force gauge INTERFACE to quantify the impact force. Thermogravimetric analysis curve was obtained from the Mettler Toledo TGA/DSC1 system. The output open circuit voltage was recorded by a multifunctional oscilloscope (DSOX3024T, InfiniiVision), while the output short circuit current and transfer charge were performed by an electrometer (Keithley 6514, Tektronix).

5.3 Result and Discussion

We have developed g-C_3N_4 doped PA_{66} nanofibers using electrospinning as illustrated in Figure 5.1a. Figure 5.1b shows the SEM image of electrospinning PA_{66} film and nylon textile at different magnifications, respectively. As the concentration of g-C_3N_4 increased to 0.7 wt. %, the electrospinning membranes appeared as particles on the

surface under which situation the membrane was fragmented and unable to fabricate TENGs (Figure 5.1c). This kind of phenomenon has also been observed in other experiments with insoluble dopants such as liquid metal[25]. From the Fourier transform infrared spectra (Figure 5.1d) of the pyrolysis synthesized sample from melamine, several strong brands in the 1200-1650 cm^{-1} region were found corresponding to the typical CN heterocycles which were almost identical to the FTIR pattern of the standard g-C_3N_4 sample, making it possible for large use of synthesized g-C_3N_4 powder in our following experiments. Besides, Thermal gravimetric analysis (TGA) showed that the thermal decomposition temperature of PA_{66} is between 450 to 500 ℃, and g-C_3N_4 is between 600 to 750 ℃ as shown in Figure 5.1e.

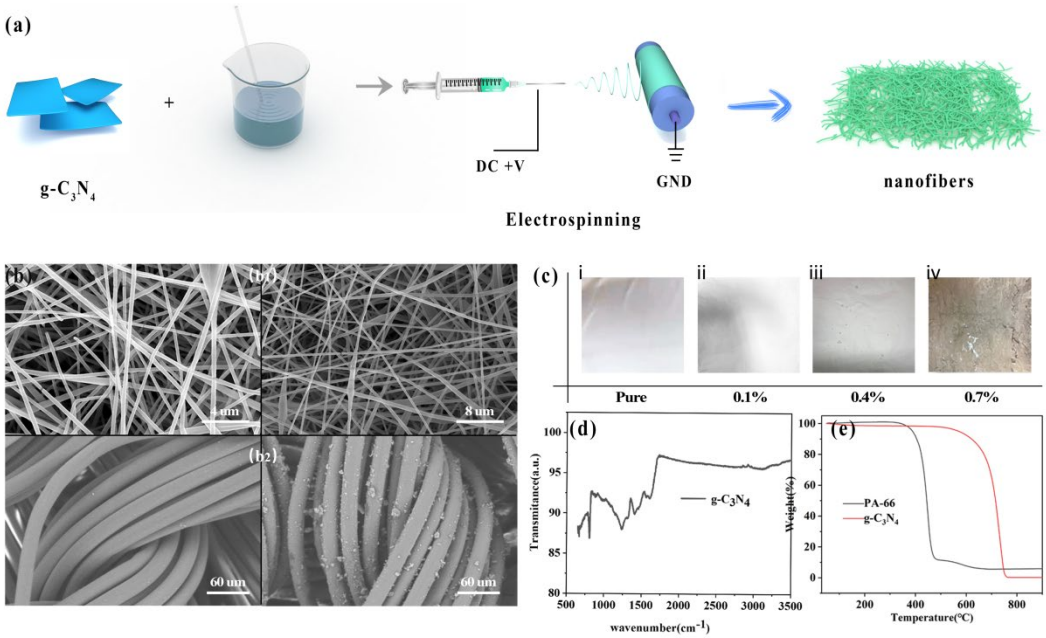

Figure 5.1 (a) Schematic illustration for preparation of electrospinning membrane. (b) SEM images of (b1) Electrospinning PA_{66} and (b2) Nylon textile cloth at different magnifications. (c) Photographic images of electrospinning membrane PA_{66} with different concentrations (i) pure (ii) 0.1 wt. % (iii) 0.4 wt. % (iv) 0.7 wt. % of g-C_3N_4. (d) Fourier transform infrared (FTIR) absorption spectra for g-C_3N_4 powders. (e) Thermal gravimetric analysis (TGA) of PA_{66} and g-C_3N_4.

The operating principle of electrospinning membrane TENG is schematically illustrated, exhibiting the process of electron transfer in a simple contact separation mode as shown

in Figure 5.2a. Subject to a periodic external force, in the initial state (Figure 5.2a(i)), positive dielectric--the PA_{66} electrospinning membrane with or without doped g-C_3N_4 contacted together with negative dielectric under force action, where the positive charges and negative charges were produced on the surface of both membranes respectively, making no electron transfer there. In the second state (Figure 5.2a(ii)), when the external force separated these two membranes and generated gaps from each other, the electronic potential difference was produced, then electrons were transferred through an external load[110] (or electrometer) from one electrode to another, then an electrical current was produced. Once two membranes were separated and the gap went to the maximum (Figure 5.2a(iii)), the electrostatic equilibrium made no electrons move. When the external force broke the electrostatic equilibrium, a new opposite potential difference was generated, and the electron current flowed in an opposite direction (Figure 5.2a(iv)). During the process of contact and separation, electrons flowed

between the bottom and top electrodes continuously and generated alternating current (AC). The whole power generation process and potential distribution were simulated and demonstrated by COMSOL Multiphysics software (Figure 5.2b), where red showed positive voltage and blue showed negative voltage.

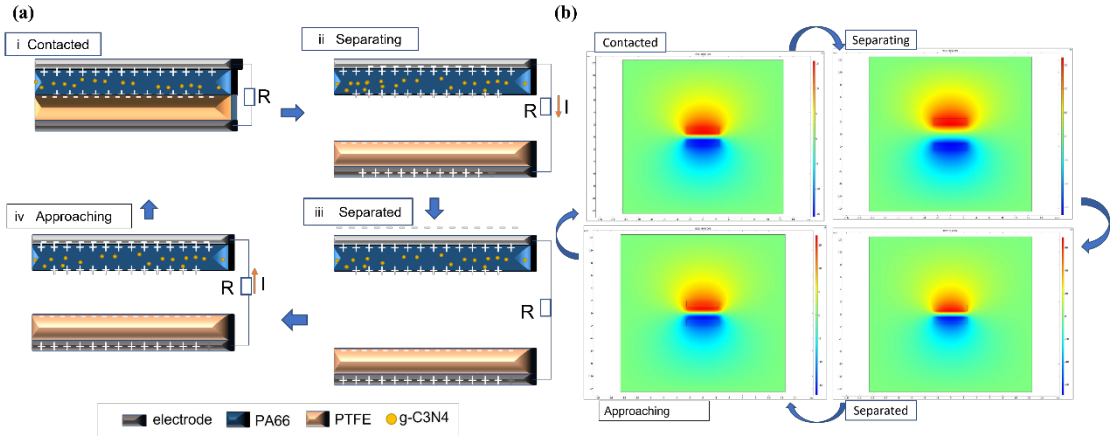

Figure 5.2 (a) Schematic diagrams of working mechanism for contact separation mode electrospinning membrane TENG with g-C_3N_4 dopant. (b) Simulation results of electrical potential distribution by COMSOL software.

The output performance of the electrospinning membrane PA_{66} with and without doping g-C_3N_4 in vertical contact-separation mode with the negative PTFE is systematically

studied as shown in Figure 5.3. At a given impact force of 30 N and 3 Hz, compared with electrospinning membrane PA_{66} without g-C_3N_4, the output open circuit voltage current maintained similar around 18 V, and short circuit current increased a little from 1.2 μA to 1.5 μA (Figure 5.3a-c), respectively. However, the transfer charge presented significant sensitivity after doping g-C_3N_4 even at a very low concentration of 0.1 wt. %, with about 12 times enhancement from 1.5 nC to 18 nC. With increasing the concentration from 0.1% to 0.4%, all three parameters—open circuit voltage, short circuit current, and transfer charge have almost doubled, as shown in Figure 5d-f. At the concentration of 0.4 wt. %, the as-made TENG shows the largest open-circuit voltage of 80 V and short current of 6 μA, as well as charge transfer around 50 nC.

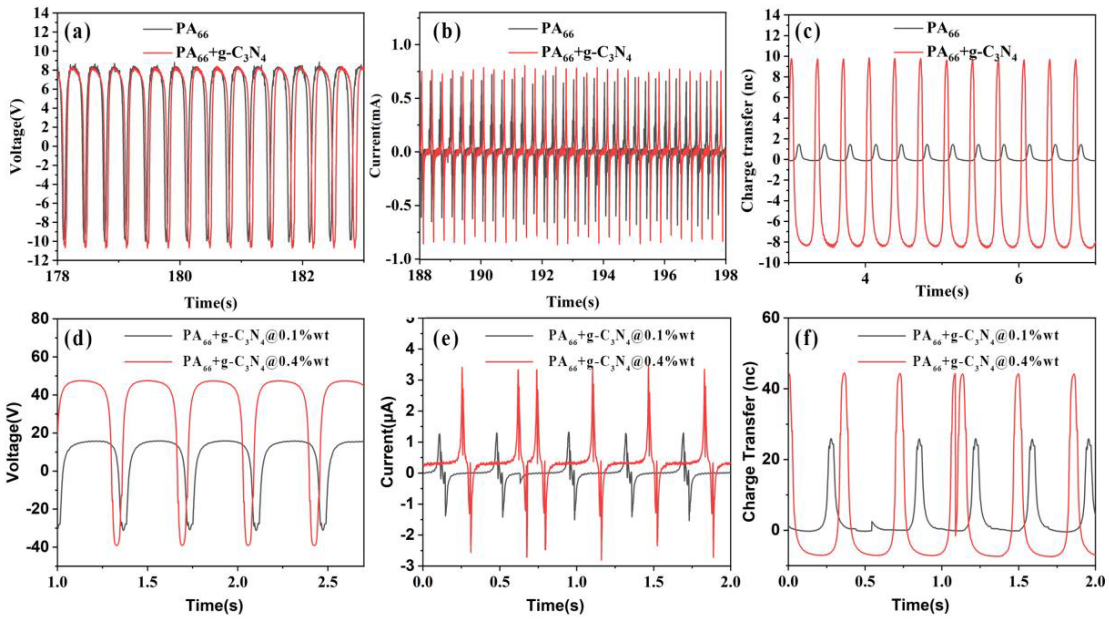

Figure 5.3 Output performance comparison of electrospinning membrane from pure PA_{66} and electrospinning membrane PA_{66} based on 0.1 wt. % doped g-C_3N_4 (low concentration) (a) open-circuit voltage (b) short circuit current (c) charge transfer. Output performance comparison of electrospinning membrane PA_{66} based on 0.1 wt. % doped g-C_3N_4(low concentration) and 0.4 wt. % doped g-C_3N_4 (high concentration) (d) open-circuit voltage (e) short circuit current (f) charge transfer.

The influences of doped PA_{66} TENG under different forces and frequencies are also studied in this study, as shown in Figure 5.4. The force's impact is not significant

(Figure 5.4a-c) as compared with the impact of frequency (Figure 5.4d-f). As for the influence of frequency, the current is increased gradually from 3 μA to 14 μA as the frequency was increased from 1 Hz to 8 Hz (Figure 5.4e), while voltage (Figure 5.4d) and charge transfer (Figure 5.4f) remain almost the same under different frequencies. One possible explanation might be that a higher impact frequency can stimulate the flow of external electrons in a shorter time under similar forces, which may result in an increased current output[151], while the thin electrospinning membrane cannot hold a large surface charge and surface potential to significantly affect voltage. Charge transfer has already been sensitive and significant even under small frequencies, so charge may not be able to increase significantly at growing frequencies[151].

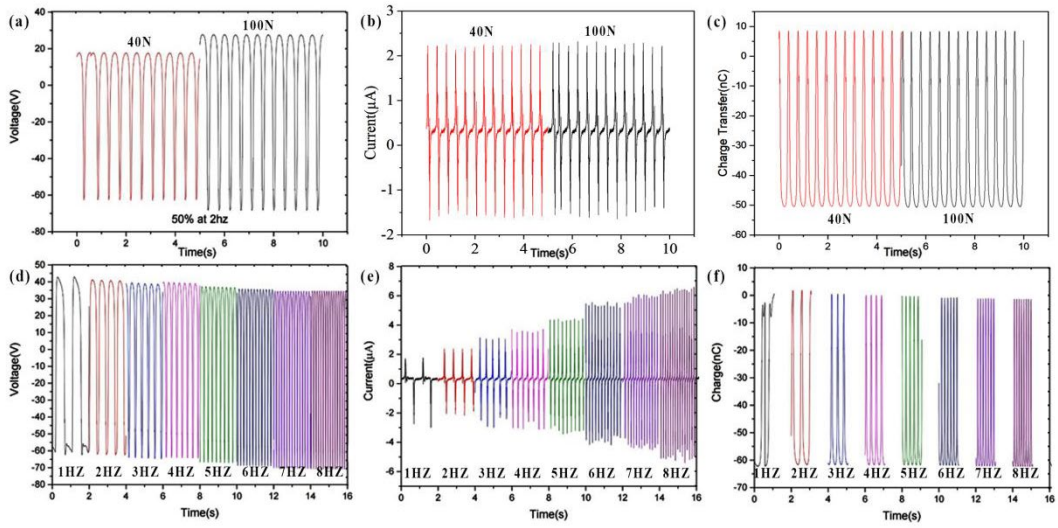

Figure 5.4 (a) Open-circuit voltage (b) Short-circuit current (c) Charge transfer of PA_{66} electrospinning membrane TENG with different impacting forces at 40 N and 100 N intensity under the same frequency of 3 Hz. (d) Open-circuit voltage (e) Short-circuit current and (f) Charge transfer of PA_{66} electrospinning membrane TENG with different frequencies from 1 Hz to 8 Hz under the same impact force of 100 N.

The change between the energy band and conduction band of a semiconductor makes it more sensitive in terms of charge transfer. Compared to dark conditions but has little effect on voltage and current (Figure 5.5a-b), even 0.1 wt. % low-concentration doping

can still produce great changes in charge transfer (from 20 nC to around 40 nC) under ultraviolet light conditions as shown in Figure 5.5c. g-C_3N_4 is a light-sensitive semiconductor, and its rich nitrogen element makes it easy to lose electrons, so adding it to the positive electrode dielectric can produce a superimposed triboelectrification generation effect. The C-N atom in its structure is sp2 hybridized to form a highly delocalized π-conjugated system[193]. Among them, the Npz orbital constitutes the highest occupied molecular orbital (HOMO) of g-C_3N_4[194], and the Cpz orbital constitutes the lowest unoccupied molecular orbital (LUMO)[195]. Its bandgap is around 2.7 eV, which can absorb blue-violet light with a wavelength of less than 475 nm in the solar spectrum[193]. Under light conditions (365 nm UV), the electrons in g-C_3N_4 can be easily lost[196] because the light is also one kind of electromagnetic wave, as shown in Figure 5.5d. Charge-transferring between the discretized energy levels generates energy band gaps. The intermolecular interactions facilitate electron hopping, the developing

microcurrents, and conductive networks[197]. The charge circuits in the produced conductive loops develop secondary fields and induce the magnetic moments in the 2D structures[124] (Figure 5.5e-f).

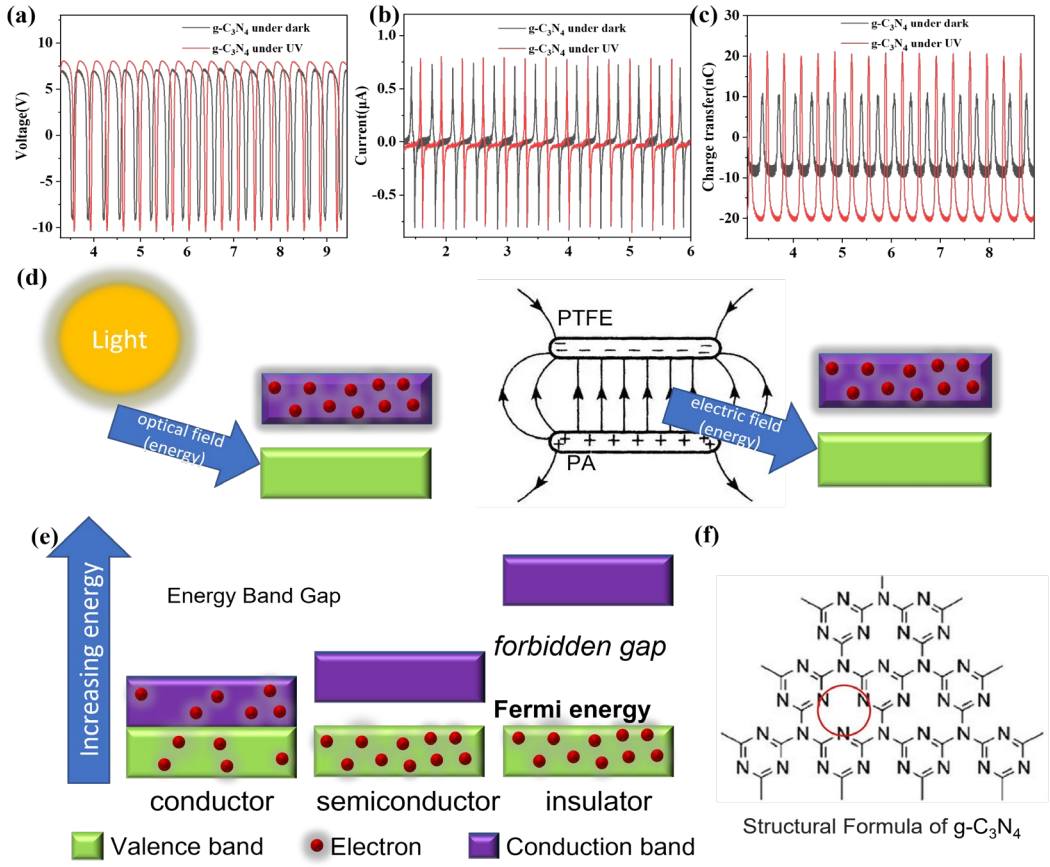

Figure 5.5 Electrical output comparison of electrospinning membrane PA_{66} TENG with doped g-C_3N_4 under UV light condition and dark condition (a) open-circuit voltage (b) short circuit current (c) charge transfer. (d) Illustration of light and electric field influence. (e) Energy bandgap theory of g-C_3N_4. (f) The molecular structural formula

of g-C_3N_4[198].

The magnetic and electric field coupling enhanced each other macroscopically from microcosmic. Therefore, the material used in the positive electrode is much more effective than the negative electrode. As a comparison, we did a comparative experiment of PVDF doped g-C_3N_4, which is using electrospinning membrane of PVDF with and without doping g-C_3N_4 powder as negative dielectric while utilizing PA_{66} electrospinning membrane as positive dielectric, all the others are the same as the electrospinning membrane TENG as stated above (using contact separation mode and Cu/Ni coated conductive fabric as electrode), where we can see that there are slight differences with open-circuit voltage, short circuit current and charge transfer[199] for PVDF membrane with and without doping g-C_3N_4 (Figure 5.6), which is consistent with our assumption. For comparison, Polyacrylonitrile (PAN) electrospinning membrane

TENG was also fabricated and evaluated, where short circuit current is also increased generally from about ±1 μA to ±4 μA at the frequencies from 2 Hz to 10 Hz, while open circuit voltage is increased slightly from 35 V to 60 V at a frequency of 2 Hz to 6 Hz and then keeps almost stable afterward (Figure 5.7). Besides, the electrospinning membrane surpasses usual films in TENG applications mainly due to its nano-scale high porosity, which also generated advantages like degradability, as well as disadvantages like vulnerability.

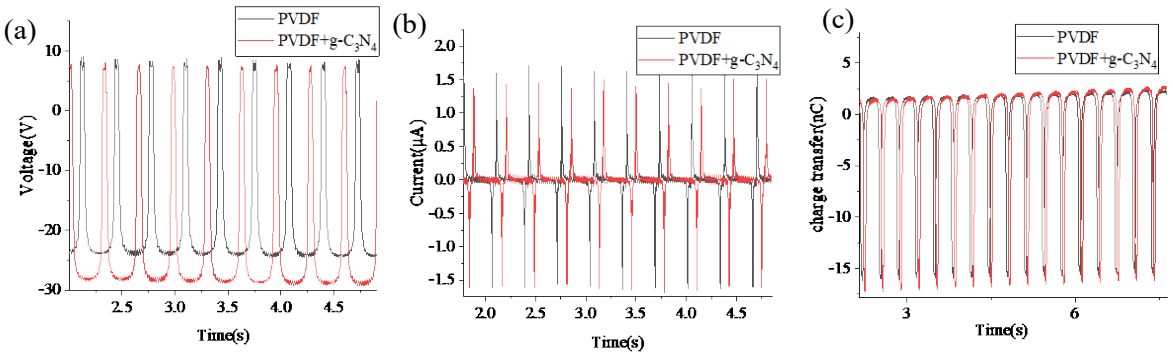

Figure 5.6 Electronic Output of PVDF electrospinning membrane with and without g-C_3N_4 doping of (a) open-circuit voltage (b) short circuit current (c) charge transfer.

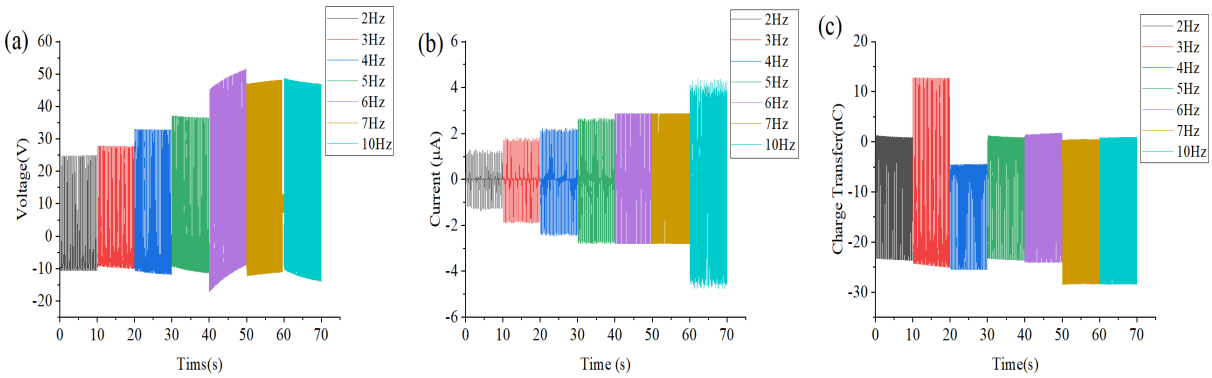

Figure 5.7 (a) Open-circuit voltage (b) short circuit current (c) charge transfer of PAN electrospinning membrane TENG with different frequencies 2 Hz, 3 Hz, 4 Hz, 5 Hz, 6 Hz, 7 Hz, 10 Hz under the same impact force of 100 N.

The charging capacity of the doped electrospinning membrane was also evaluated by using different capacitors. As a demonstration, the continuously generated energy was used to directly drive an electronic watch and calculator (Figure 5.8a). The output power generated by the electrospinning membrane TENG can light up at least 40 LEDs connected in series by gentle hand clapping (Figure 5.8b). The output power density of the electrospinning membrane was also systematically evaluated by connecting with

different external load resistances. At a fixed frequency of 3 Hz and impact force of 40 N, different resistors from 10 kΩ to 10 GΩ were externally connected to measure the output current, where the output current decreased with the increase of load resistance. Based on the measurements, the power density was calculated and reached the maximum value of 45 mW/m^2 at a load resistance of 500 MΩ (Figure 5.8c). The charging rates of the different capacitors were calculated as 14 mV/s for 1.5 μF, 6 mV/s for 4.7 μF, and 2 mV/s for 10 μF, respectively, with results shown in Figure 5.8d.

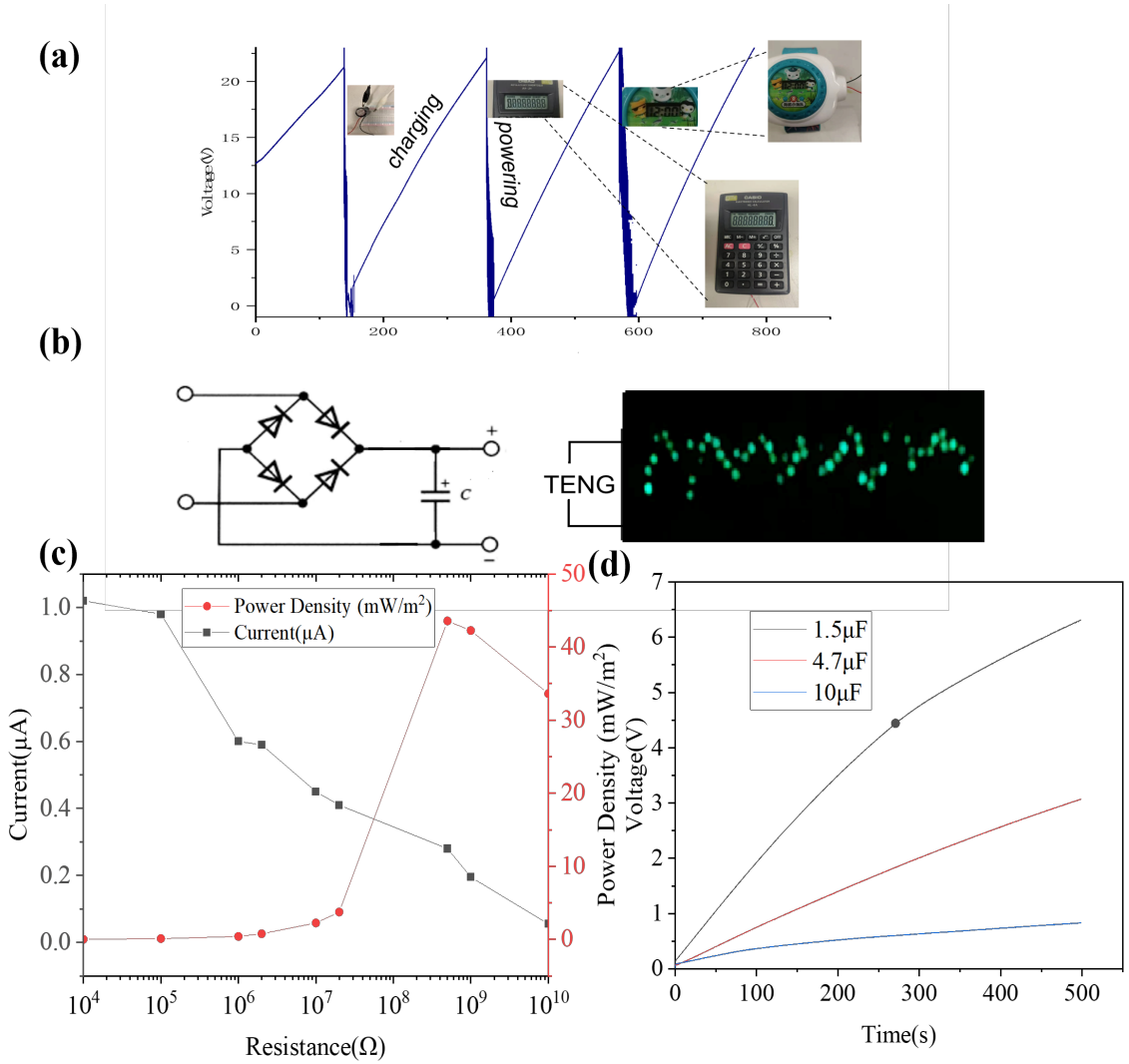

Figure 5.8 (a) Charging voltage curves of the electrospinning membrane TENG in the process of continuous powering calculators and electronic watches. (b) Illustration of electrospinning membrane TENG for lighting up 40 LEDs. (c) Dependence of output current and average power density of the electrospinning membrane TENG on load resistances. (d) Charging curves of 1.5 μF, 4.7 μF, and 10 μF capacitors.

This doped electrospinning membrane was also made into an energy device to harvest biomechanical energy from human motions. The structure of this wearable electrospinning membrane TENG is illustrated in Figure 5.9a, our electrospinning membrane acted as a positive tribe-layer adhered to an aluminum film electrode, while PTFE as a negative tribe-layer adhered to Cu/Ni conductive fabric electrode, then assembled these two using sponge to separate positive and negative layers with a litter space and wrapped insulating tapes outside. This thin TENG can be fixed on shoes or gloves, generating electricity during human motion, which also shows the potential application as an electronic signal sensor. For example, gentle touching by hand could generate electric pulses of 1 V, 400 nA, and 5 nC, and the output of stepping voltage, current, and charge transfer with foot are around 20 V, 0.8 μA, and 10 nC, respectively. As demonstration of applications, for its flexibility, the doped electrospinning membrane can also be made as an energy flag to scavenge wind kinetic energy (Figure

5.9b). With a similar structure, PTFE was adhered to conductive film and fixed to a vertical board, and the electrospinning membrane was adhered to soft conductive fabric and the upper side was fixed and placed near the PTFE board. The fan can generate three levels of different wind speeds (Fan1 with a low wind speed of 2.1 m/s, Fan2 with a middle wind speed of 3.0 m/s, and Fan3 with a high wind speed of 3.9 m/s). When the wind blew to the electrospinning membrane from one side, making the membrane contact and separate with PTFE film intermittently, this thin TENG can generate electricity with output positively related to wind speed, that is 3 V, 6 V, 9 V at 2.1 m/s, 3.0 m/s, 3.9 m/s, respectively.

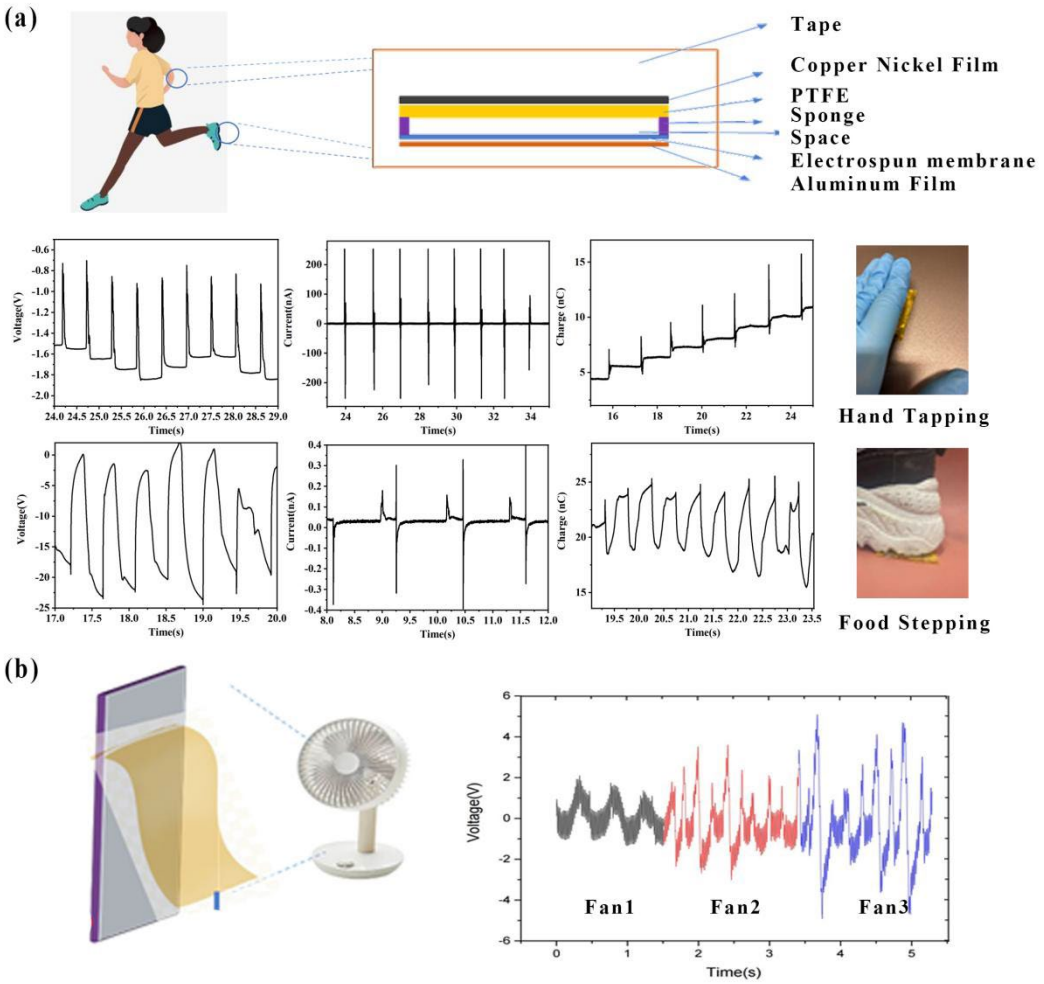

Figure 5.9 (a) Application of electrospinning membrane TENG for harvesting human motions. (b) Electrospinning membrane TENG for savaging wind energy under different levels of fan speed.

5.4 Conclusion

In summary, we have designed and fabricated a novel and multifunctional TENG with PA_{66} nanofibers doped with 2D g-C_3N_4 nanosheets. Resultantly, the doped TENG at 0.4 wt. % showed twice the electrical output performance as compared to the pure PA_{66} electrospinning membrane. The addition of g-C_3N_4 makes a tremendous difference in the charge transfer, which means charges are particularly sensitive to g-C_3N_4 doping probably because of the semiconductive character. In the presence and absence of light, low-concentration doping of g-C_3N_4 also affects charge transfer. Low-concentration doping (0.1 wt. %) has little effect on voltage and current but has a greater impact on charge transfer while a high concentration (0.4 wt. %) can double the electricity performance on voltage, current, and charge transfer. Demonstration of applications showed that TENG made from electrospinning membrane nanofibers can be well utilized to harvest biomechanical energy as electronic skin from human motions as well

as natural wind energy as flags and are expected to be further employed in self-powered device systems, where the doped material's character can be further developed for its multifunctional properties. Power density, intrinsic impedance, and energy conversion efficiency[200] of energy harvesting from electrospinning membrane TENG with this material should be further optimized in the future by regulating material composition, inventing unique structures, and employing power management circuits.

CHAPTER 6 Synergistic Effect Study of g-C_3N_4 Composites for High-performance Triboelectric Nanogenerators

6.1 Introduction

The world is in constant pursuit of sustainable energy sources. The potential applications of TENGs range from powering electronic devices to capturing energy from humans or the environment. Hence, extensive effort has been made to design and fabricate self-powered sensors[201], sustainable energy sources[202], and wearable intelligent systems[203] through the approach of nanogenerators.

From the perspective of large-scale production, the most realistic option is the introduction of high-dielectric materials into common dielectric to significantly enhance the permittivity and electrical performance[10].In the context of TENGs, doping is used to enhance the triboelectric properties to generate electrical energy through the triboelectric effect of PDMS[204]. The simplest option is the introduction of high-dielectric ceramic materials into the polymer matrix which inherently possesses a

comparatively low dielectric constant. By optimizing the doping process and concentration ratio, significant improvements in the efficiency and output of TENGs can be achieved, which makes them a more practical and feasible solution for energy applications.

In our previous research on this material[23], the simple addition of g-C_3N_4 in PDMS could increase the output of TENG. Unfortunately, the effect of combination or g-C_3N_4 hybrid dopants with PDMS, to the best of our knowledge, had not been studied or reported.

In this work, based on our previous work of novel 2D material g-C_3N_4, we further studied different g-C_3N_4 composites with various dopants such as carbon nanotubes, silver metal nanoparticles, MXene, silver oxide (AgO), at different concentrations and ratios to optimize the electrical output of hybrid dopants and summarize the generality with different combinations of dopants. In this research, we investigated the effect of

g-C_3N_4 and three substances co-doped into PDMS respectively and optimized the ratio for Ag/g-C_3N_4, CNT/g-C_3N_4 dopants. The optimal ratio under different concentrations was identified and utilized for application. The combination of a silver metal nanoparticle and g-C_3N_4 showed greater enhancement than either single dopant, and the optimum output was achieved at the ratio Ag:g-C_3N_4 of 3:1 with open circuit voltage (*Voc*) of 92 V, short circuit current (*Isc*) of 4.6 μA, charge transfer (*Qsc*) of 49 nC, which was 4 times higher than the performance of single dopant, and maximum power density achieved 1.45 $W \cdot m^{-2}$ under the resistance of 20 MΩ, at 100 N force/3 Hz frequency. Based on this hybrid dopant TENG, a self-powered multifunctional harvester was fabricated, which could be attached or adhered to different parts of the human body for biomechanical energy harvesting and human motion detectors with versatile applications. When connected to multi-channel acquisition and signal processing devices, we designed a novel disc device that detects pressure at different

locations and an insole that tracks the center of gravity and gait to correct the walking posture. The easy fabrication and enhanced performance of hybrid dopants TENG have shown their prospect for industrialization[17].

6.2 Experimental Sections

6.2.1 Materials

The silicone elastomer base and related curing agent for Polydimethylsiloxane (PDMS, SYLGARD® 184) were bought from Dow Chemical Company (USA). PDMS was fabricated by elastomer and curing agent with a ratio of 10:1. Stainless steel yarns (SSYs, Bekinox AISI 316L) were purchased from Bekaert (Belgium). CNF was purchased from 3M Carbon nanotubes (CNT), MXene, Ag, and AgO nanoparticles were from Dieckmann company, and g-C_3N_4 powders were purchased from Xianfeng Nano Co. Ltd. All the materials were used as received without further purification.

6.2.2 Fabrication of g-C_3N_4 hybrid PDMS composite

Taking Ag nanoparticles and g-C_3N_4 powders as an example, two dopants were mixed at a certain ratio and added into the PDMS liquid homogeneously, after thorough ultrasonication for more than 12 hours, 1 gram of curing agent, and 9 grams of PDMS liquid were added into the mixture and stirred for 20 minutes. Then the mixture was transferred to a mold and spread evenly across the surface of the blade to avoid air bubbles into the mixture and then kept in a desiccator under a vacuum oven at 80° for 6-12 h to form a self-standing film until it was completely cured and finally stored in a clean dry environment to avoid touching the surface. After curing, the dopant/PDMS composite films were peeled off for further characterization and fabrication, with excess PDMS trimmed away using a scalpel. The curing time might vary depending on the thickness of the coating and the specific PDMS used, as well as the environmental index.

6.2.3 Assemble of PDMS TENG

PDMS adhered to Cu/Ni conductive fabric to form the negative part, and the positive part was only CNF acting as both tribomaterial and electrode, which was then contacted and separated. The CNF electrodes were connected through copper wire and then to the electrometer to measure and collect signal of *Voc, Isc* as well as *Qsc*.

6.2.4 Characterization and Measurement

Fourier transform infrared (FTIR) absorption spectra were recorded on a spectrometer (Spectrum 100, Perkin Elmer). The Raman spectra were conducted by using a NomadicTM Raman 3-in-1 microscope with 532 nm lasers. The X-ray powder diffraction (XRD) patterns were recorded on an X-ray diffractometer (D8 Advance, Bruker) with Cu Kα radiation to identify the crystalline phase. Field Emission Scanning Electron Microscope (SEM, Tescan MIRA) was used to characterize the morphology and Energy Disperse Spectroscopy (EDS) data were acquired simultaneously. XPS

spectra were investigated on an ESCALAB210 spectrometer. The output performance under impacting/releasing cycles was evaluated by utilizing a Keyboard Life Tester (ZX-A03, Zhongxingda, Shenzhen), with impact force signal monitored simultaneously by the DAQ (Dewetron, Dewe-2600 DAQ system). The output voltage signal was collected by Keysight DSO-X3014A oscilloscope and N2790A high voltage probe with 8 MΩ internal resistance. Open-circuit voltage and short-circuit current were measured using an electrometer system Keithley 6514.

6.3 Result and Discussion

6.3.1 Fabrication and Characterization

Figure 6.1a shows the schematic fabrication of hybrid dopants TENG. Taking Ag/g-C_3N_4 PDMS as an example, after adding both silver and g-C_3N_4 nanoparticles into PDMS solution, the molecular structure manifests as 2D framework, wherein each

hexagonal unit of the g-C_3N_4 lattice encapsulates a single silver atom, facilitating synergistic interaction with increased conductivity, electron mobility, and more charge transfer[205]. Then the hybrid dopant PDMS composite was prepared by the blade-coating method, as illustrated in Figure 6.1b, where dopants included g-C_3N_4 powders with one of materials including Ag nanoparticles, MXene powders, nickel-coated carbon nanotubes, multiwall carbon nanotubes, and AgO at different weight ratios. Figure 6.1c demonstrated the architecture of basic contact-separation mode TENG, where the copper-nickel conductive fabric (CNF) acted as both positive dielectric and electrode, along with hybrid dopant/PDMS composite as negative dielectric, and the two dissimilar dielectric films faced with each other. The X-ray diffraction analysis (XRD) of g-C_3N_4 powder was executed, as shown in Figure 6.1d, where a significant peak at 28° is indexed to crystalline phase g-C_3N_4.

Surface functional groups were investigated by FTIR where PDMS composite with different ratios of silver nanoparticles and g-C_3N_4 powders showed a similar pattern, as shown in Figure 6.1e, mainly showing the peaks of PDMS functional groups. Typical peaks of Ag nanoparticles at 2,921 cm^{-1} and 1,029 cm^{-1} were marked in the FTIR pattern. Typical peaks of PDMS included ~3,000 cm^{-1} of CH_3, ~1,250 cm^{-1} of Si-CH_3, ~1,000 cm^{-1} for Si-O-Si, and ~750 cm^{-1} of Si-CH_3. Generally, g-C_3N_4 showed a sharp absorption at ~ 807 cm^{-1} where we could identify a peak around 800-850 cm^{-1} in the FTIR pattern for all three composites with small drift.

The Raman spectrum of g-C_3N_4 typically displayed a peak at around 800-900 cm^{-1} which was attributed to the in-plane stretching vibration of the carbon-nitrogen bonds, and another peak at around 1,300-1,400 cm^{-1} which was related to the out-of-plane bending mode of the nitrogen atoms[206]. Additionally, there might be peaks at higher frequencies (above 1,600 cm^{-1}) associated with the stretching modes of the carbon

atoms in this material.[207] Silver Raman spectrum typically showed several peaks corresponding to different vibrational modes of the silver atoms or molecules in the sample, which could be divided into two categories. The first one was related to the translational and rotational vibrations of the silver atoms, which were usually observed in the low-frequency region below 400 cm^{-1}. The second category corresponded to the vibrational modes of the silver molecules or clusters[208], and typically appeared in the high-frequency region above 400 cm^{-1}. The most prominent peak in the silver Raman spectrum was typically associated with the longitudinal optical phonon mode (LO) at around 400 cm^{-1} [209]. We could see from Figure 6.1f that with the increase of Ag concentration, the band in the Raman spectrum had increased significantly. Other notable peaks in the silver Raman spectrum included the transverse optical phonon mode (TO) at around 430 cm^{-1}, the surface-enhanced Raman scattering (SERS) peak at around 1,600 cm^{-1}, and the surface plasmon resonance (SPR) peak at around 380 nm in

the UV-Vis region[210]. PDMS had one significant big peak around 2,900 cm^{-1} and one small peak around 500 cm^{-1} [207]. The exact position and intensity of these peaks could depend on the specific synthesis method and composition. The position and intensity of these peaks provide information about the chemical composition, crystal structure, and bonding properties of the material. Scanning electron microscopy (SEM) and elemental mapping (EDS) of Ag/g-C_3N_4 PDMS composite were also employed to display the distribution of certain dopants, as shown in Figure 6.1g, which demonstrated the existence of silver, carbon and nitrogen element.

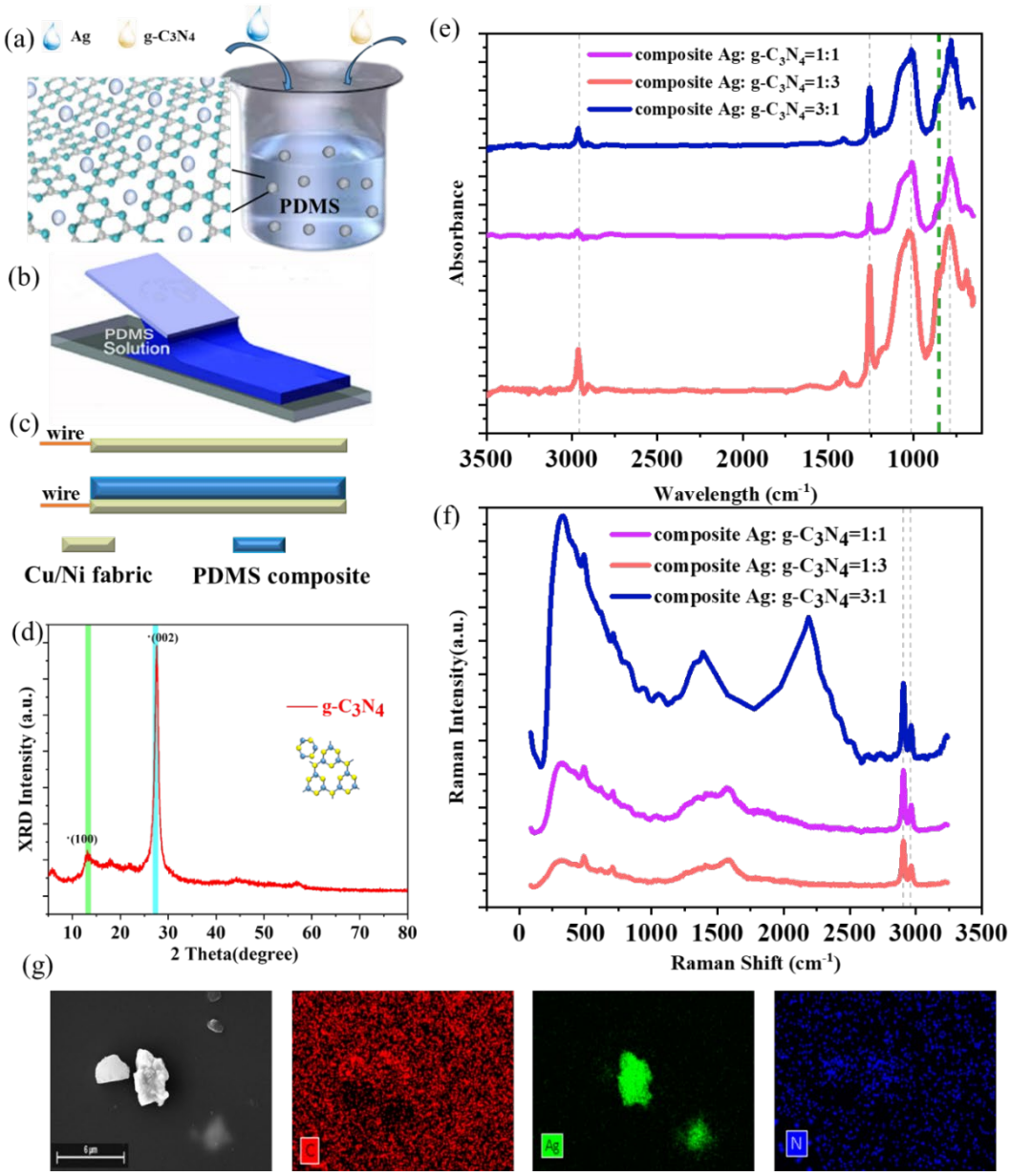

Figure 6.1 Illustration of fabrication of hybrid dopants TENG (taking dopants silver nanoparticles and g-C_3N_4 powder as an example). (a) Mixing of PDMS, silver nanoparticles, and g-C_3N_4 powders. (b) Blade coating of the mixture. (c) Structure of TENG. (d) XRD pattern of g-C_3N_4 powder. (e) FTIR spectra for PDMS composites

with different ratios of Ag/g-C_3N_4. (f) Raman spectra of a sample with a total of 1 wt. % dopant of Ag/g-C_3N_4 at different ratios in PDMS composite. (g) SEM of Ag/g-C_3N_4 PDMS composite and EDS mapping of elements.

The X-ray Photoelectron Spectroscopy analysis (XPS) shown in Figure 6.2 was also carried out to observe constituent elements of the Ag/g-C_3N_4 PDMS composite. From XPS spectra, apart from the constituent C and N elements, the presence of Ag could also be observed in the spectrum of the Ag/g-C_3N_4 PDMS composite[211]. Because of the low concentration of doping, the N and Ag peaks were not significant. The existence of Ag nanoparticles and g-C_3N_4 nanosheets in PDMS might lead to a strong interaction between two materials because of the intimate attachment of the two materials, and N could donate the lone pair of electrons to the outermost orbital of Ag.

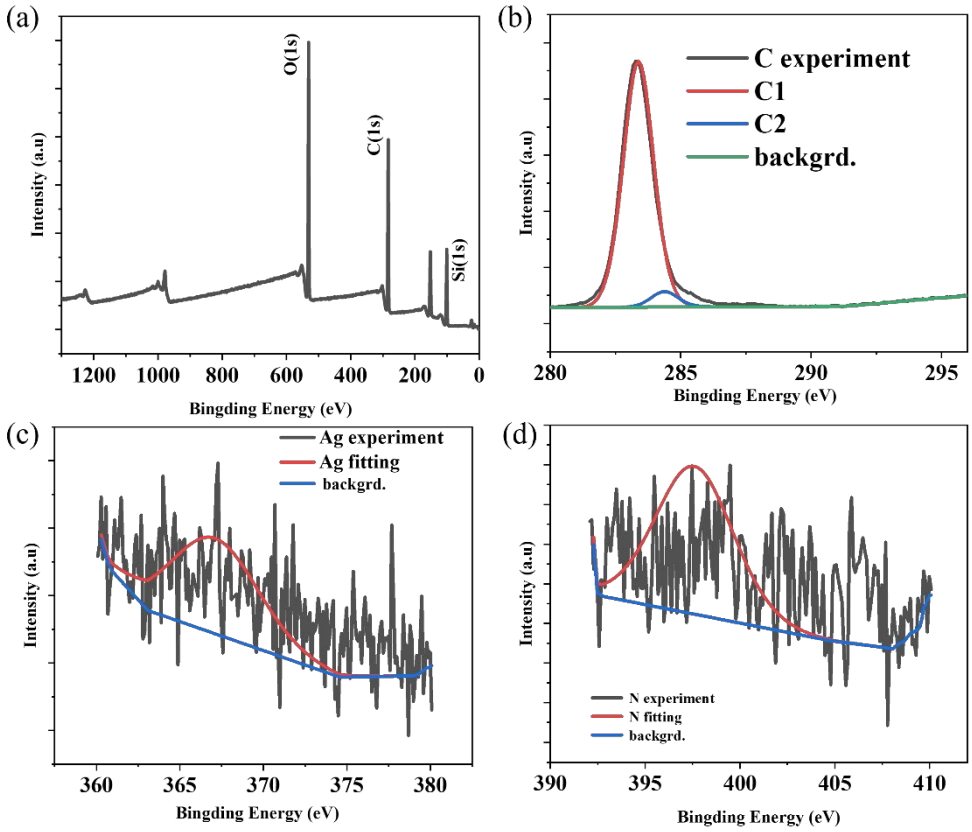

Figure 6.2 (a) XPS survey spectra of Ag/g-C_3N_4 PDMS composite. High-resolution XPS spectrum showing the binding energy of (b) C, (c) Ag, and (d) N electrons.

6.3.2 Mechanism

The schematic diagrams manifested the detailed working principle of a triboelectric device using the hybrid doped PDMS composite film as negative and CNF as positive triboelectric materials, respectively. From the first stage (Figure 6.3aI), where there was

no electron transfer and electrode potential, the applied impact force shown in Figure 6.3aII separated the two dielectrics, and then electrification induced the corresponding charges, which caused the charges to transfer from one electrode to another to balance the increased electric potential from decreasing capacity (Figure 6.3aIII). While approaching, the charges returned from the positive to the negative electrode for the increasing capacity and formed an opposite voltage as well as displacement current (Figure 6.3aIV)[212]. The process of repeated contact and separation thus generated a continuous alternating current[213]. The electric potential distribution was also simulated using COMSOL software to show the electricity-generating process, as shown in Figure 6.3b. Figure 6.3c demonstrated a rectifier as an electronic device that converted AC into DC with consistent polarity by using one or more P-N junction diodes or bridge rectifiers[142]. Figure 6.3d demonstrated a single alternate current pulse for one contact separation circle, where plus and minus peaks occurred while pressing and releasing

and the repeated back-and-forth process acquired continuous voltage pulses and alternating current[151]. Figure 6.3e illustrated the schematic structure of the PDMS composite TENG for output voltage[214]

$$V = \frac{(\sigma - \Delta\sigma) \cdot d_{gap}}{\varepsilon_0} - \frac{\Delta\sigma \cdot d_{dopant\ /\ PDMS}}{\varepsilon_0 \cdot \varepsilon_{dopant\ /\ PDMS}}$$

where V is the output voltage, σ is the triboelectric charge density on the dopant/PDMS surface, $\Delta\sigma$ is the charge density transferred between electrodes, ε_0 is the vacuum permittivity, and $\varepsilon_{dopant/PDMS}$ denotes the relative permittivity of the dopant/PDMS composite, d_{gap} stands for the inter-layer spacing, and $d_{dopant/PDMS}$ is the thickness of dopant/PDMS film. During open circuit conditions, the charge transfer is zero, indicating that *Voc* is maximum when the gap reaches maximum and *Voc* has no explicit dependency on the properties of triboelectric layer, but σ surface charge density is related to the dielectric constant of the triboelectric material[215].

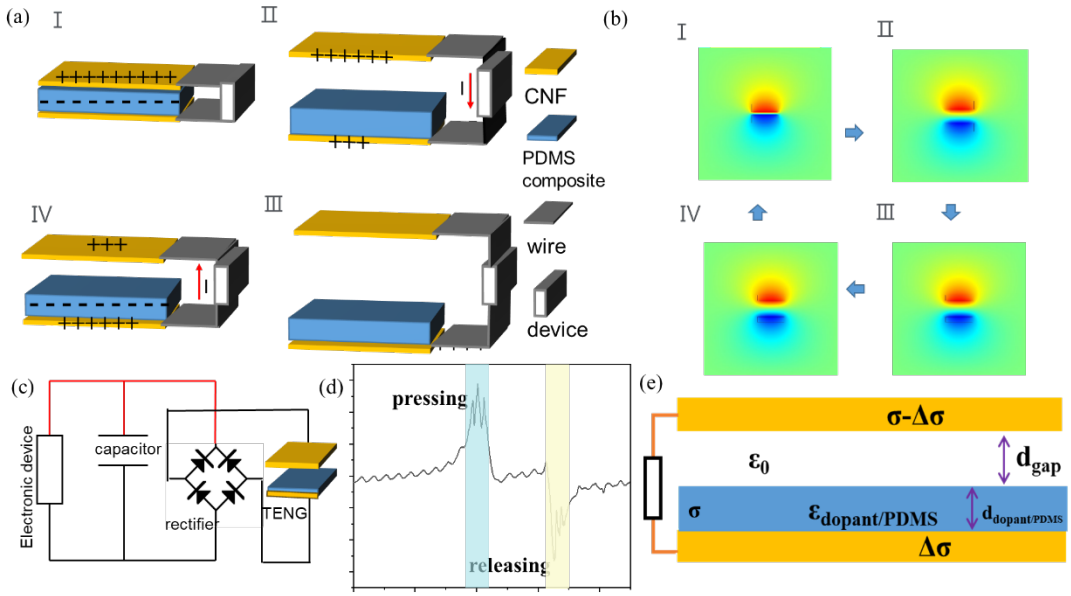

Figure 6.3 (a) (I-IV) Schematic diagrams of the working principle of contact and separation mode TENG. (b) Simulation results of electrical potential distribution by COMSOL Multiphysics software. (c) Equivalent circuit of a self-powered system TENG, capacitor, another device, and rectifier changing AC to DC. (d) Two opposite electric peaks during a single circle of contact and separation. (e) Schematic structure of dopant/PDMS TENG.

6.3.3 Electrical Output

To evaluate the triboelectric performance, the hybrid dopant/PDMS film was adhered to CNF to form the negative part, and the positive part was only CNF acting as both

triboelectric material and electrode, with an effective area of 4 cm^2, which was then contacted and separated under an impact force of 100 N at a frequency of 3 Hz. The CNF electrodes were connected through copper wire and then to the electrometer to measure and collect signal of *Voc, Isc* as well as *Qsc*. Based on our preliminary experimental results, the triboelectric performance increased significantly from dopant concentration 5 wt. ‰ to 5 wt. %, so we selected the total doping content at 1 wt. % to facilitate comparison for reasons of practicality and morphology. With consideration of the accuracy and comparability of the experiment, we set the total mass concentration at 1 wt. %, that was, each sample contains 9-gram elastomer, 1-gram curing agent, and 0.1-gram dopant in total.

For the group of dopants of CNT and g-C_3N_4, it was composed of a different ratio for each sample, which was 0.1 g CNT, 0.075 g CNT+0.025 g g-C_3N_4 (3:1), 0.05 g CNT+0.05 g g-C_3N_4 (1:1), 0.025 g CNT+0.075 g g-C_3N_4 (1:3), and 0.1 g g-C_3N_4

respectively, with electric performance *Voc* shown in Figure 6.4a, *Isc* in Figure 6.4b, and *Qsc* in Figure 6.4c. The hybrid dopant TENG showed higher values of three parameters of *Voc*, *Isc*, and *Qsc* than single dopant TENG of either CNT or g-C_3N_4. The optimum concentration ratio to achieve the best electric performance was CNT: g-C_3N_4 =0.05:0.05 (1:1), reaching peak-peak *Voc* at 122 V, *Isc* at 5.8 μA, and *Qsc* at 105 nC approximately. Conductive dopants could compete for a dual capacitive effect causing different performances with changes of concentration and ratio[216], which could be explained by the percolation theory. Once the concentration of CNT exceeded the percolation threshold concentration (Pc), conductive paths would be formed due to the direct contact of the CNT dopants and the quantum tunnel effect. This could be regarded as an equivalent circuit in which series capacitance and resistance were in parallel[217]. The triboelectric charge would be neutralized, thus decreasing the surface charge density[218].

For another group of dopants Ag and g-C_3N_4, the dopant weight was 0.1 g Ag, 0.09 g Ag+0.01g g-C_3N_4 (9:1), 0.075 g Ag+0.025 g g-C_3N_4 (3:1), 0.05 g Ag+0.05 g g-C_3N_4 (1:1), 0.025 g Ag+0.075 g g-C_3N_4 (1:3), 0.01 g Ag+0.09 g g-C_3N_4 (1:9), 0.1g g-C_3N_4, each for 10 g PDMS mixture, respectively. The optimum concentration ratio was Ag:g-C_3N_4 = 0.075:0.025 (3:1), reaching peak-to-peak *Voc* at 92 V as shown in Figure 6.4d, *Isc* at 4.6 μA in Figure 6.4e, and *Qsc* at 49 nC in Figure 6.4f, which was more than 4 times of either pure Ag or pure g-C_3N_4, approximately. In addition, the hybrid dopants Ag/g-C_3N_4 TENG showed higher *Voc, Isc*, and *Qsc* than single dopant TENG of either pure Ag or g-C_3N_4. Some other groups of hybrid dopants including AgO/g-C_3N_4 and MXene/g-C_3N_4 were also prepared and evaluated. A proper hypothesis might be that, when silver nanoparticles and g-C_3N_4 powders were co-doped in PDMS, the doping ratio affected the triboelectric properties and performance of the negative dielectric. A higher doping ratio of silver nanoparticles could improve the electrical conductivity of

the PDMS, enhancing the charge transfer and electrical output of the TENG. The capacitive effect would help to reduce the potential difference through polarizing and charging at the two end sides, thus increasing the generation amount of triboelectric charge. While too much filler would reduce the triboelectric charge through leaking current passing through the conduction path built by the inter-connected nanoparticles or tunneling current between adjacent nanoparticles, isolated distributed wire-like fillers would enhance the triboelectric charge amount through the capacitive effect[217], but too much doping could reduce the mechanical deformation of PDMS, affecting the charge generation[219]. On the other hand, g-C_3N_4 could introduce more active sites for charge transfer and improve the performance stability, However, too much silver nanoparticle doping could lead to an increase in resistance and a decrease in the flexibility of the PDMS. Therefore, a suitable doping ratio was necessary to balance the

electrical and mechanical properties of the negative electrode and achieve optimal TENG performance.

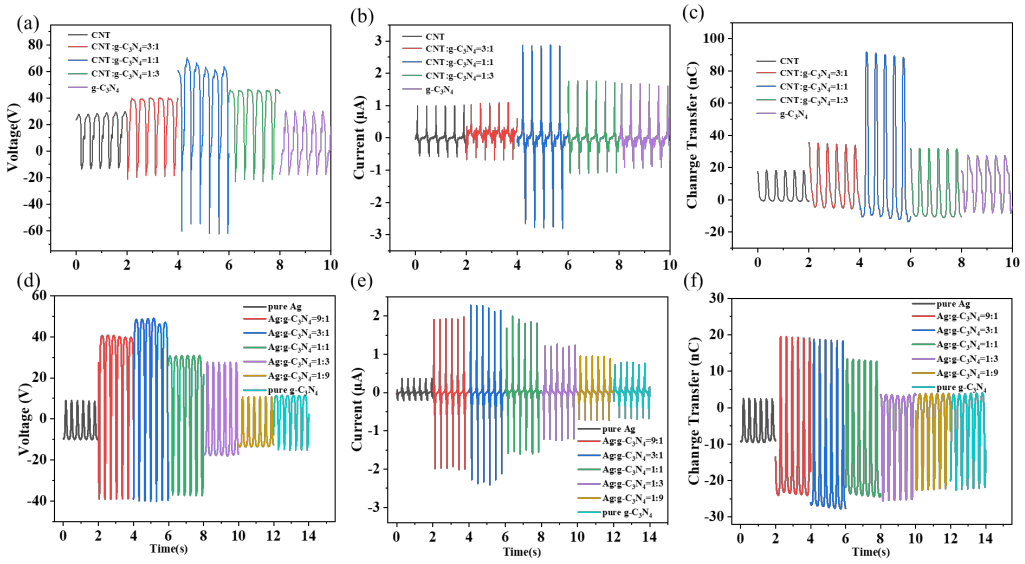

Figure 6.4 Electric performance of hybrid dopant TENG. (a) Open circuit voltage, (b) Short circuit current, (c) Charge transfer of TENG with different ratios of carbon nanotube and g-C_3N_4 at a total weight proportion of 1 wt. %. (d) Open circuit voltage, (e) Short circuit current, (f) Charge transfer of TENG with different ratios Ag nanoparticles and g-C_3N_4 at a total weight proportion of 1 wt. %.

6.3.4 Influence of External Factors

The performance of TENG can be influenced by frequency or external force[199], so we have evaluated the Ag/g-C_3N_4 hybrid dopant/PDMS TENG at the optimum concentration ratio of 3:1, at different frequencies of 1 Hz, 2 Hz, 3 Hz, 4 Hz, 5 Hz and 6 Hz under a fixed external force of 100 N, and different external forces of 10 N, 50 N, 100 N, and 200 N under a fixed frequency of 2 Hz, respectively. When the frequency increased gradually from 1 Hz to 6 Hz, the performance did not change very much around 80 V for *Voc* and about 25 nC for *Qsc* but increased significantly from 2.2 μA to 6.8 μA for *Isc*, as shown in Figure 6.5a-c. As the external force rose progressively from 10 N to 200 N, the *Voc* increased from 40 V to 130 V (Figure 6.5d). In the meantime, the *Isc* increased gradually from 2.0 μA to 10.2 μA (Figure 6.5e) and the *Qsc* increased from approximately 20 nC to 90 nC, approximately (Figure 6.5f). As discussed above, when the frequency increased, the current of TENG increased while the changes in charge and voltage were relatively small. This phenomenon could be

mainly due to the capacitive nature of TENGs, where the electric charge stored on the surface of the TENG increased with the frequency but the voltage across the TENG remained relatively constant. As a result, the current generated by the TENG increased with frequency, leading to an enhancement in the electrical output of the TENG. Moreover, the overall performance of the TENG also depended on other factors, such as material properties, surface roughness, operating conditions, and surrounding environment parameters including temperature, humidity, etc.

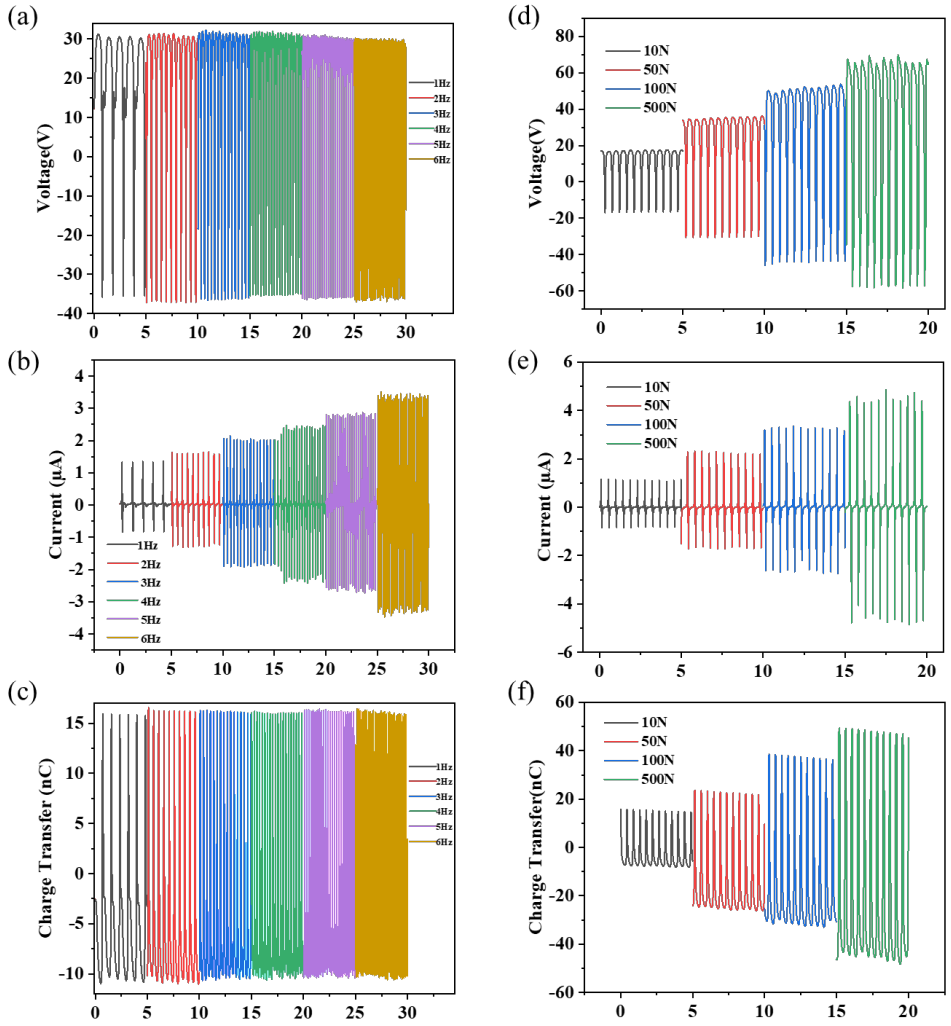

Figure 6.5 (a) Open circuit voltage (b) Short circuit current (c) Charge transfer at different frequencies from 1 Hz to 6 Hz and (d) Open circuit voltage (e) Short circuit current (f) Charge transfer at different impact forces of 10 N, 50 N, 100 N, and 200 N, respectively.

In Figure 6.6, doping nickel-coated CNTs with g-C_3N_4 at a 1:1 ratio in PDMS composite resulted in improved TENG performance, with *Voc, Isc*, and *Qsc* reaching 70 V, 3.5 μA, and 45 nC, respectively, doubling output compared to pure nickel-coated CNTs. Similarly, a 1:1 ratio of multiwall CNTs and g-C_3N_4 yielded a twofold increase in electrical parameters, with *Voc, Isc,* and *Qsc* at 140 V, 6 μA, and 100 nC, respectively. For MXene/g-C_3N_4 PDMS composites, the optimal electrical performance was reached at a 1:1 ratio, with peak *Voc* of 20 V and *Isc* of 0.45 μA, while the highest *Qsc* of 8 nC was observed at a 4:1 ratio. The comparative investigation found that silver dopants outperformed silver oxide in all parameters, while hybrid dopants consistently surpassed the performance of individual dopants. Our experimented dopants were either conductive (metal particles, carbon nanotubes) or semiconductive (g-C_3N_4, MXene).

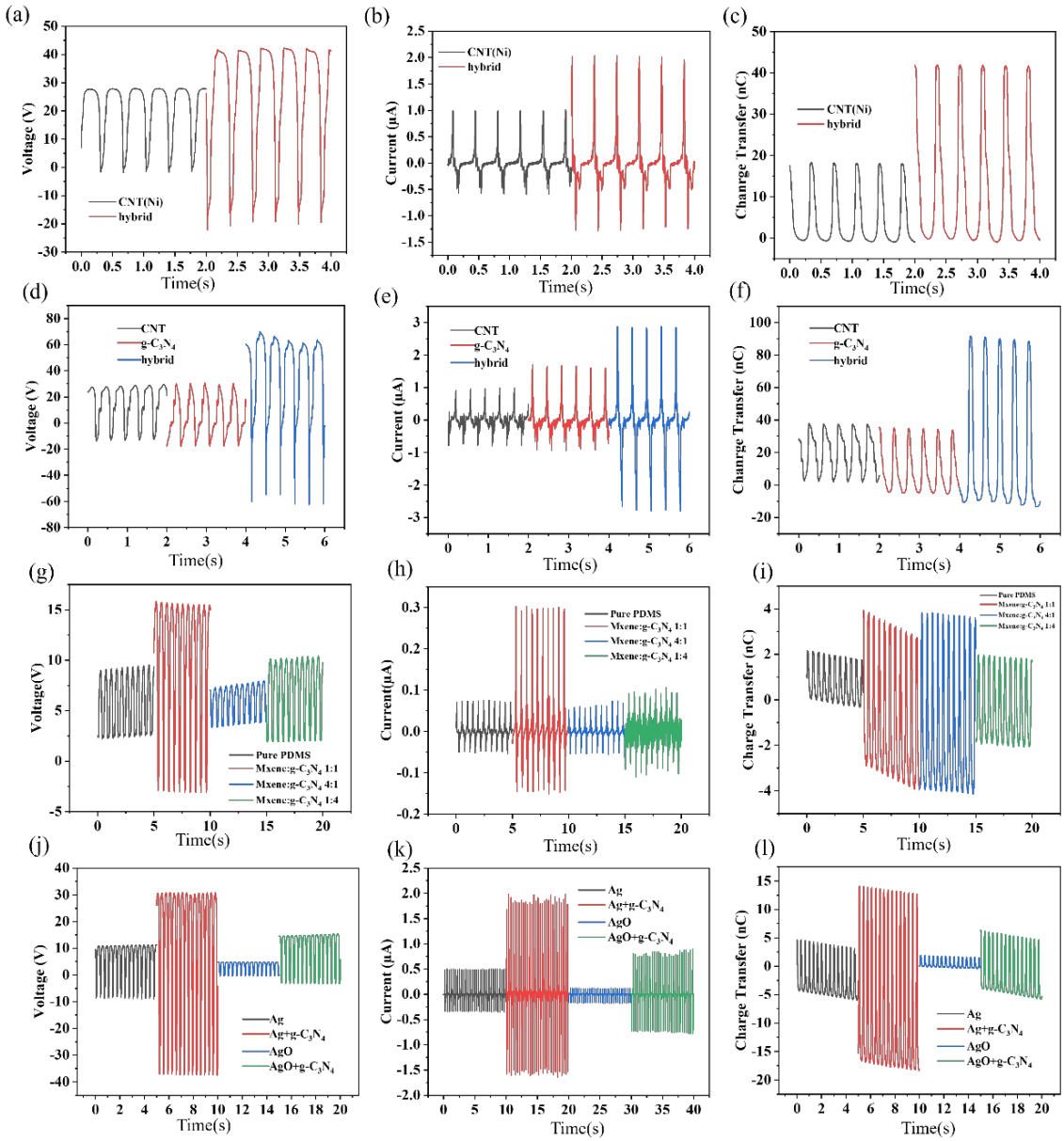

Figure 6.6 (a) Open circuit voltage, (b) Short circuit current, and (c) Charge Transfer of TENG with nickel-coated carbon nanotubes, nickel-coated carbon nanotubes together with g-C_3N_4. (d) Open circuit voltage, (e) Open circuit voltage, and (f) Charge Transfer of TENG with multiwall carbon nanotubes, g-C_3N_4, hybrid multiwall carbon

nanotubes and g-C_3N_4. (g) Open circuit voltage, (h) Short circuit current, and (i) Charge Transfer of TENG with MXene with different ratios of g-C_3N_4. (j) Open circuit voltage, (k) Short circuit current, and (l) Charge Transfer of TENG with Ag, Ag and g-C_3N_4, AgO, AgO and g-C_3N_4.

Table 3 below summarizes TENGs with various dopants where our hybrid dopant/PDMS TENG showed better performance.

Table 3. Comparison with other similar works

Dopants	Substrate	Size (cm^2)	V (V)	I (μA)	Power density (mW/m^2)	Ref.
CNT on surface	PDMS/steel	12×10	1.7	-	-	[220]
Aligned Li	ZnO nanowire	-	1.6	-	-	[221]
Ag	ZnO nanowire	10	2	0.5	-	[222]
TiO_2	PVDF	9×7.5	8.8	-	16	[223]
MAPbBr	PVDF	9.5×8.5	5	-	2.8	[224]
Vitamin B_2	PVDF	-	0.27	-	-	[225]
ZnO	PVDF	3×3	1.7	-	2	[226]
ZnS	PVDF	8×8	6	-	1.5	[227]
Cu nanowire	PDMS	2×2	45	-	134	[228]
FCB	PDMS	5×5	50	4	12	[229]
Ag+ g-C_3N_4	PDMS	2×2	92	4.2	1,450	This work
CNT+ g-C_3N_4	PDMS	2×2	122	5.8	-	This work

6.3.5 Application

The output power density was evaluated by connecting with different external load resistances from 1 Ω to 500 MΩ at a working frequency of 3 Hz and force impact of 100 N. It can be noted that the current decreased as the resistance increased. Then the instantaneous peak power density of TENG can be calculated by $P=I^2R/S$, where P, I, R, and S denoted power density, output current, resistance, and size. The peak power

density achieved maximum of 1.45 W/m^2 for Ag/g-C_3N_4 PDMS TENG at the resistance of 20 MΩ (Figure 6.7a) and 1.5 W/m^2 for CNT/g-C_3N_4 PDMS TENG at the resistance of 100 MΩ (Figure 6.7b) respectively. To assess the potential of TENGs as energy sources, we investigated the charging capabilities of Ag/g-C_3N_4 PDMS TENG in Figure 6.7c demonstrating the equivalent electrical circuit diagram of a self-powered system including TENG as a power source, a capacitor as an energy storage unit, and a rectifier as an alternating current-to-direct current converter. Typically, a smaller capacitance value results in a relatively higher charging speed. These findings suggested that TENGs can power small electronics such as calculators, watches or LEDs. By incorporating a TENG, capacitor, and rectifier into a self-powered system, the generated energy can effectively operate these devices. The durability and storability were essential properties for devices, which would influence further applications. Ag/g-C_3N_4 PDMS TENG was experimented with continuous impact force

up to 20,000 cycles and placed at room condition with temperature from 20 ℃ to 35 ℃ and humidity from 48% to 86% after immediately fabricated till 10 days, which showed similar, stable, and steady results, as shown in Figure 5d, demonstrating relative high durability and stability little affected by the external environment. Based on its flexibility in real-world applications, TENG could be fabricated as a self-powered wearable sensor when attached onto human joints of the knee, wrist, and elbow, as demonstrated in Figure 6.7e.

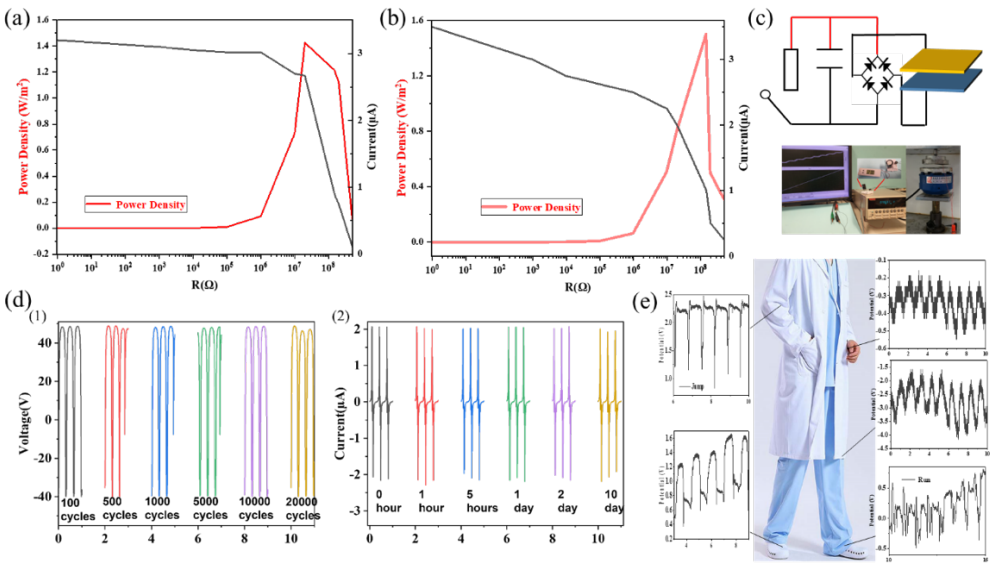

Figure 6.7 (a) The instantaneous peak power density of (a) Ag/g-C_3N_4 PDMS TENG (b) CNT/g-C_3N_4 PDMS TENG at a series of external resistance loadings and the

corresponding current output. (c) The equivalent circuit of charging capacitance and photographic demonstration. (d) Durability study for Ag/g-C_3N_4 PDMS TENG after (1) 100, 500, 1000, 5000, 10000, and 20000 cycles, respectively, as well as (2) 0 hour, 1 hour, 5 hours, 1 day, 2 days, 10 days, respectively. (e) Applications of Ag/g-C_3N_4 PDMS TENG as self-powered wearable sensors.

Subsequently, with a multichannel data acquisition system, the self-powered electric output via touch could recognize the tactile trajectory and detect the pressure distribution. A circular PDMS film was divided into eight equal segments with alternating conductive foil 1-4 to four channels for independent signal capture. Touching these sections activated a single electrode TENG, which could generate voltage pulse (>60 mV) in the corresponding channel while producing negligible signals in non-contacted channels (Figure 6.8a), enabling real-time touch localization

through electronic signal tracking (Figure 6.8b). Two round TENGs were also integrated into an insole at the front and back to monitor the center of gravity and analyze gait for posture correction using multi-channel signal acquisition and processing. Voltage outputs, depicted in Figure 6.8c, indicated a higher peak at the front TENG when weight was forward, and conversely, a higher rear TENG signal when weight shifted backward, as shown in Figure 6.8d. Balanced weight distribution resulted in nearly equal TENG signals, with average values and the insole's structure presented in Figure 6.8e.

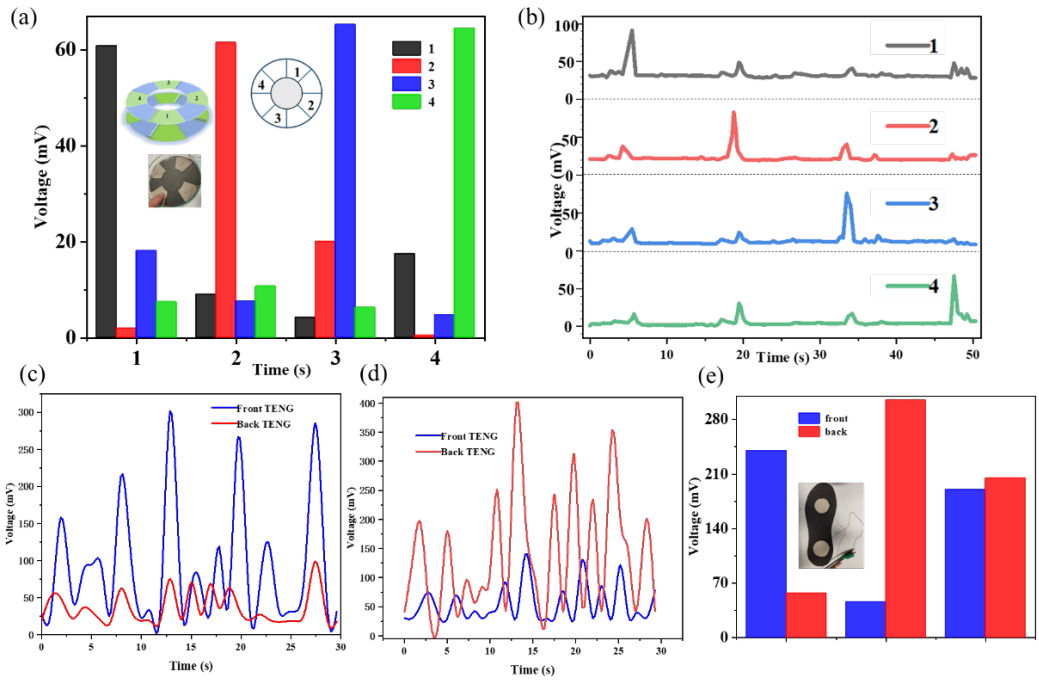

Figure 6.8 (a) Bar chart comparison of average sensing signals for a four-channel pressure sensing system, inset is the pattern illustration and real picture. (b) Sensing signal patterns by the sequence of pressing channels 1, 2, 3, and 4 in succession sequentially. (c) Signal pattern of the two-TENG insole while walking with the center of gravity at the front. (d) Signal pattern of the two-TENG insole while walking with the center of gravity at the back. (e) Bar chart comparison of average sensing signals while walking with center at the front, center at the back, and center at the middle, respectively, inset is the photo of the double-TENG insole.

Figure 6.9 (a-f) shows one application as adhered to elbow generating different levels of voltage with different movements, 1.5 voltage from total stretching to bending to angle 30°, 0.3 V from stretching to 90°-fold, and 0.5V from stretch to 30°. Based on the Bluetooth module and filter circuit module, the real-time signal generated by our hybrid

TENG can be transferred wirelessly to personal mobile devices and displayed on the software application functional interface (Figure 6.9g).

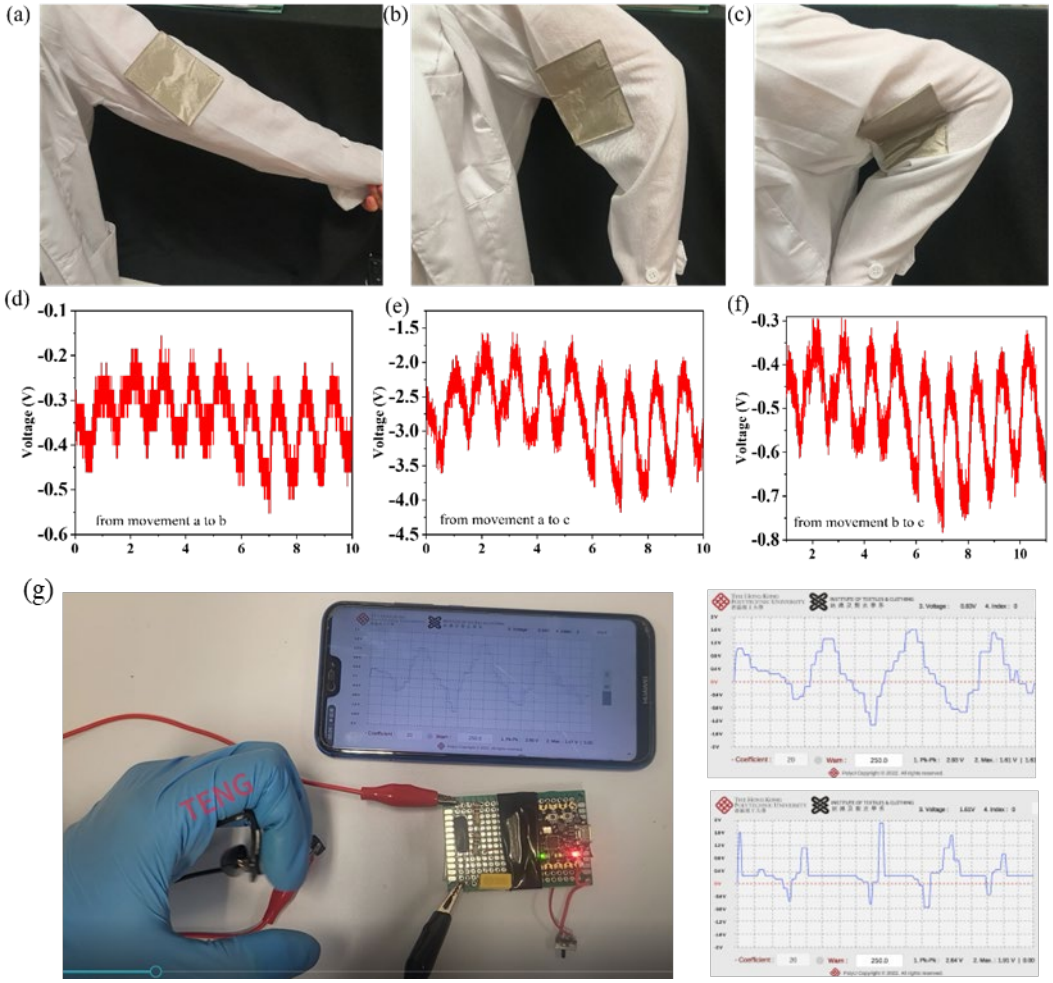

Figure 6.9 Monitoring of elbow bending angles by pasting hybrid dopant PDMS composite TENG on the elbow (a) stretching, (b) moving to 90°, (c) bending to 30°. Voltage generated while moving (d) from position a to b, (e) a to c, (f) from position b to c. (g) Bluetooth circuits intelligent wireless system and interface of mobile software.

6.4 Conclusions

In summary, the hybrid dopants/PDMS composites were designed and prepared by embedding nanoparticles into the PDMS matrix, and experiments on ratio optimization with different hybrid dopants were carried out. Ag/g-C_3N_4 at the ratio of 3:1 at 1 wt % in PDMS composite manifested the best electrical properties with *Voc* of 92 V, *Isc* of 4.6 μA, *Qsc* of 49 nC, under 100 N and 3 Hz, and the optimized composite TENG reached output power density of 1.45 W/m^2. Similar to that of Ag/g-C_3N_4, CNT/g-C_3N_4 embedded hybrid dopant/PDMS TENG presented the optimal mixture ratio at 1:1 to achieve the best electric performance of *Voc* at 122 V, *Isc* at 5.8 μA, and *Qsc* at 105 nC. Other groups of hybrid dopants including AgO/g-C_3N_4 and MXene/g-C_3N_4 were also evaluated. TENGs made from PDMS were flexible, resistant, and durable, which could be applied in wearable electronics and positioned at various joint parts of the human body. When connected to multi-channel acquisition and signal processing devices, we

designed a novel disc device that detected pressure at different locations and an insole that tracks the center of gravity of the gait to correct the walking posture. Our TENG could convert mechanical energy from human motion into electrical energy, providing energy sources as well as self-powered sensors for wearable devices. This work provided insights and a promising avenue for boosting the output of electricity and practical applications of TENG.

CHAPTER 7. Conclusion and Future Work

7.1 Conclusions

This research mainly highlights the enhancement of electrical performance with ongoing advancements and challenges in the field of TENGs, particularly focusing on two-dimensional materials with the integration of flexible and stretchable materials for triboelectric and electrode layers.

While a variety of materials exist for flexible triboelectric layers, suitable flexible and bionic-skin electrode materials remain limited. Hydrogels have emerged as promising candidates due to their excellent stretchability, self-healing capabilities, and conductive properties. However, they also present significant drawbacks, including low electrical conductivity, suboptimal mechanical and biocompatibility characteristics, limited responsiveness to external stimuli, and susceptibility to dehydration. For example, the output performance of the TENGs requires further development and essential

improvement in areas such as output power, energy transfer efficiency, sensor sensitivity, and compatibility with energy storage. This necessitates extensive research and the adoption of higher active materials or architectural structures. Addressing practical challenges in applications imposes more stringent requirements on safety, service life, pollution, and comfort of the energy supply devices, particularly when integrating TENGs with peripheral application devices, including electronic components, Bluetooth, WIFI, Arduino, etc.

By reviewing the development progress and presenting research status of TENGs for mechanical energy harvesting, this research points out the existing problems and challenges in this field. As a bridge for gaps between current issues and practical requirements, this research work aims at designing and fabricating several TENGs in innovative structures and rationally adopting novel materials. In the practice of electrospinning techniques, some novel doping materials were first experimented with,

reviewed, summarized, and systematically analyzed, including inorganic materials, organic materials, semiconductive materials, metals, halogens, and biological materials, based on their inherent and intrinsic characteristics. The goal is to develop TENGs with enhanced electrical output performance and multifunctionality, making them suitable for practical applications in advanced mechanical energy harvesting and contributing to the development of neutral carbon smart cities. The mechanism of triboelectrification, macro-level discussions on energy structure, and the practical application potentials of triboelectric nanogenerators will be further discussed in our future research. This research endeavors to bridge the gap between existing challenges and practical applications by designing and fabricating innovative TENG structures and employing novel materials. Through the application of electrospinning techniques and the exploration of various doping materials—including inorganic, organic, semiconductive, metallic, halogen, and biological materials—we have systematically analyzed their

inherent properties. The objective is to develop TENGs that not only enhance electrical output performance but also support multifunctionality for advanced mechanical energy harvesting, thereby contributing to the vision of a carbon-neutral smart city. In summary, this thesis systematically develops high-performance flexible triboelectric nanogenerators by exploring some 2D materials and rationally developing four kinds of innovative TENGs. Moreover, methods for synthesizing and processing the electroactive materials were carefully designed and adopted to sustain the inherent advantages of 2D materials. The developed TENG devices, including those with the PVA single electrode, TMCC dopant PDMS, and electrospun g-C_3N_4 structures, demonstrate promising solutions for enhancing the performance of TENGs in biomechanical energy harvesting and self-powered sensing applications. The series of flexible and wearable TENGs designed and fabricated in this research, including PVA single electrode, TMCC dopant PDMS, and electrospun with g-C_3N_4, provide

promising pathways for the development and innovation of 2D material in enhancing TENG for biomechanical energy harvesting and self-powered sensing. To bridge the gap between the existing issues and the practical requirements, several important conclusions are drawn, as outlined below.

First, Nb_2S_2C and Ta_2S_2C of Transition Metal Carbo-Chalcogenides (TMCCs), were employed to develop new TENGs with doping with PDMS. The optimum concentration ratio of 3 wt. ‰ was identified to achieve the best electric performance. Moreover, the tribology evaluation revealed that the Ta_2S_2C/PDMS composite presented a lower coefficient of friction (COF) than Nb_2S_2C/PDMS composite.

Second, PVA hydrogel of g-C_3N_4 was obtained at optimal doping concentration of 2.7 wt. % Other common dopants including carbon nanotube, zinc chloride, and lithium chloride had also been evaluated. Hydrogel-TENG can be further fabricated into electronic skin with functions of human motion detector and energy harvesting for

application. Different morphologies including discoid flake, tube shape, and innovative spiral shape with PVA as either electrode or tribo-positive material have also been developed and evaluated.

Third, a novel and multifunctional TENG designed and fabricated with PA_{66} nanofibers doped with 2D g-C_3N_4 nanosheets where 4 wt. ‰ showed twice the electrical output performance. Charge transfer was particularly sensitive with even 1 wt. ‰ g-C_3N_4 doping with significant difference in the presence and absence of light. Power density, intrinsic impedance, and energy conversion efficiency of energy harvesting from electrospinning membrane TENG with this material should be further optimized in the future.

Fourth, Hybrid dopant/PDMS composites were designed and prepared by embedding nanoparticles into the PDMS matrix. Ag/g-C_3N_4 at the ratio of 3:1 at 1 wt. % in PDMS composite manifested the best electrical properties with *Voc* of 92 V, *Isc* of 4.6 μA, *Qsc*

of 49 nC, power density of 1.45 W/m^2 under 100 N and 3 Hz. CNT/g-C_3N_4 embedded hybrid dopant/PDMS TENG presented the optimal mixture ratio at 1:1 to achieve the best electric performance of *Voc* at 122 V, *Isc* at 5.8 μA, and *Qsc* at 105 nC. Other groups of hybrid dopants including AgO/g-C_3N_4 and MXene/g-C_3N_4 were also evaluated. We designed a novel disc device that detected pressure at different locations and an insole that tracks the center of gravity of the gait to correct the walking posture with multi-channel acquisition and signal processing devices.

7.2 Limitations of the Work and Recommendations for Future Study

Despite the successful design, testing, and fabrication of TENGs with enhanced output through doping and material modifications, several key areas require further investigation. These include improving output power, energy transfer efficiency, sensor sensitivity, and compatibility with energy storage devices. The recommendations for

future study in this field can be summarized below:

(1) To meet the demands for practical applications, the output performance of the fabricated TENGs requires further enhancement, particularly in terms of output power and sensing capability. Improving the energy efficiency of the 2D material-based TENGs is another key priority, which can be achieved by adopting or inventing higher-performance triboelectric active materials or architectures. To meet the demands for practical applications, the output performance of the fabricated flexible TENGs still needs to be further enhanced. The output power and sensing capability of fiber TENGs should be optimized. To essentially improve the energy efficiency of 2D material-based TENGs, higher triboelectric active materials or architectures are supposed to be extensively adopted, invented, and experimented with.

(2) The underlying mechanisms of 2D materials should be further investigated to facilitate the development of novel 2D material systems. As more 2D materials are

being synthesized or developed, factors such as quantum confinement effects, surface effects, and interlayer interactions play crucial roles in governing the unique physical and chemical properties of 2D materials. Elucidating these fundamental mechanisms through experimental and theoretical studies will provide critical insights for the rational design and engineering of 2D materials with tailored functionalities. This knowledge can then be leveraged to expand the portfolio of 2D materials beyond the commonly explored graphene, transition metal dichalcogenides, and hexagonal boron nitride.

(3) In addition to dopant engineering, other strategies should be explored to enhance the performance of TENGs. Promising approaches encompass structural optimization, material selection, and interface modification, all of which can improve the output power, energy conversion efficiency, and durability of TENG devices. By incorporating high-performance piezoelectric or pyroelectric materials, employing micro/nano-

structuring techniques, and tailoring surface properties through functionalization, the overall performance of TENGs can be significantly boosted, thereby expanding their practical applicability in self-powered systems and energy harvesting.

(4) The real-world applications of TENGs require further development and demonstration. While TENGs have demonstrated considerable potential in various domains, such as self-powered sensors, flexible electronics, and biomedical devices, their widespread adoption necessitates addressing challenges related to power density, stability, and reliability. Fostering collaborative efforts among material scientists, device engineers, and end-users is essential to identify and address specific application-driven requirements, facilitating the seamless integration of TENG technology into practical, large-scale systems.

(5) Continued research on polymer-based substrates for TENG devices is crucial. The mechanical, electrical, and thermal properties of polymeric materials used as TENG

substrates exert significant influence on the overall device performance. Systematic investigations into molecular design, synthetic modification, and composite reinforcement of polymers can facilitate the development of advanced substrate materials with enhanced functionality. This knowledge can ultimately contribute to the optimization of TENG devices, improving their suitability for diverse applications, ranging from wearable electronics to integrated energy harvesting systems.

(6) As self-powered sensing applications, the electrical signals of TENGs are easily disturbed by jamming signals, necessitating improvements in their sensing accuracy. Strategies to enhance the signal-to-noise ratio and improve the sensing reliability of TENG-based sensors will be essential for their widespread adoption in practical applications.

(7) The stability of 2D materials under real-world conditions presents a considerable challenge. Moreover, the long-term health effects and biocompatibility of 2D materials

remain uncertain. Additionally, inconsistencies in fabrication methods and material purity levels further complicate the evaluation of their safety profile. Addressing these challenges requires systematic improvements in material stability and the development of standardized safety evaluation protocols. Long-term field testing under real-world conditions is essential to validate these approaches.

(8) Energy harvesting density remains insufficient for powering many practical devices. The inherently low charge density and high impedance of TENGs limit their ability to meet the demands of energy-intensive applications, such as continuous operation of wearable sensors or portable medical devices. Energy storage further compounds the limitations of TENG systems. As sensors, TENGs operate based on variations in current and voltage due to applied forces, which are inherently discontinuous. This results in lower precision and sensitivity compared to traditional stress/strain-based resistive or capacitive sensors. Albeit their practicality may be limited, especially in high-precision

applications, the major advantage of TENGs lies in their self-powering capability.

From mechanism aspect, one factor that dopants enhance the performance of TENGs could be the enhancement of dielectric constant—an undoubtedly valid mechanism supported by numerous studies and our own experiments with an LCR meter. However, quantitative research on surface charge density remains lacking in our current experiments, whereas in contemporary TENG research, it is considered a factor with a far more significant influence than dielectric constant. Kelvin Probe Force Microscopy (KPFM) experiments can, to some extent, quantify surface charge density, and its systematic and accurate influence holds substantial value for further investigation.

From mechanistic and microscopic perspective, the size, orientation, and distribution of dopant nanoparticles may possibly influence the performance of TENGs at the micro level, and the difference in influences on TENG with surface-localized dopants and bulk dopants can also be further investigated. Scanning Electron Microscopy with

Energy Dispersive X-ray Spectroscopy (SEM-EDS) and Atomic Force Microscopy (AFM) can be employed to characterize the size of nanoparticles, the degree of dispersion homogeneity, and the extent of agglomeration, as well as their subsequent effects on TENG performance. Given the symmetric structure of two-dimensional materials at the molecular level, the influence of orientation remains to be confirmed. However, for magnetic nanoparticles, significant changes and effects in orientation may occur under external electromagnetic fields.

Future improvements should focus on enhancing energy storage solutions and refining sensor sensitivity and precision, tailored to broaden their practical applicability. Additionally, improving the energy harvesting density through innovations in material design and triboelectric interface engineering will be crucial. Scalable manufacturing techniques, such as roll-to-roll processing and low-cost 3D printing, could also play a pivotal role in transitioning TENG-based systems from laboratory prototypes to

commercially viable products.

In conclusion, this research has made substantial progress in advancing flexible and wearable TENGs through the application of innovative 2D materials. However, further efforts are necessary to address the existing limitations and further enhance the performance, reliability, and practical applicability of these TENG devices. Collaborative interdisciplinary research involving material scientists, device engineers, and end-users will be crucial to unlocking the full potential of TENG technology and driving its integration into real-world self-powered systems and energy harvesting solutions.

References

1. Wu, C.; Wang, A. C.; Ding, W.; Guo, H.; Wang, Z. L., Triboelectric Nanogenerator: A Foundation of the Energy for the New Era. *Advanced Energy Materials* **2019,** *9* (1), 1802906.

2. He, W.; Liu, W.; Chen, J.; Wang, Z.; Liu, Y.; Pu, X.; Yang, H.; Tang, Q.; Yang, H.; Guo, H.; Hu, C., Boosting output performance of sliding mode triboelectric nanogenerator by charge space-accumulation effect. *Nat Commun* **2020,** *11* (1), 4277.

3. Chowdhury, A. R.; Abdullah, A. M.; Hussain, I.; Lopez, J.; Cantu, D.; Gupta, S. K.; Mao, Y. B.; Danti, S.; Uddin, M. J., Lithium doped zinc oxide based flexible piezoelectric-triboelectric hybrid nanogenerator. *Nano Energy* **2019,** *61*, 327-336.

4. Zhong, X.; Sun, P.; Wei, R.; Dong, H.; Jiang, S., Object recognition by a heat-resistant core-sheath triboelectric nanogenerator sensor. *Journal of Materials Chemistry A* **2022,** *10* (28), 15080-15088.

5. Tremmel, S.; Luo, X.; Rothammer, B.; Seynstahl, A.; Wang, B.; Rosenkranz, A.; Marian, M.; Zhu, L., Evaluation of DLC, MoS2, and Ti3C2T thin films for triboelectric nanogenerators. *Nano Energy* **2022,** *97*.

6. Fan, F.-R.; Tian, Z.-Q.; Lin Wang, Z., Flexible triboelectric generator. *Nano Energy* **2012,** *1* (2), 328-334.

7. Wang, Z. L., Triboelectric Nanogenerators as New Energy Technology for Self-Powered Systems and as Active Mechanical and Chemical Sensors. *Acs Nano* **2013,** *7* (11), 9533-9557.

8. Wang, Z. L., Triboelectric nanogenerators as new energy technology and self-powered sensors - principles, problems and perspectives. *Faraday Discuss* **2014,** *176*, 447-458.

9. Anlin, L. K.; Vijoy, K. V.; Pradeesh, K.; Thomas, S.; John, H.; Saji, K. J., Effects of Metal Nanoparticles on the Performance of PDMS Based Triboelectric Nanogenerators. *Physica B: Condensed Matter* **2022,** *639*.

10. Jing, T.; Xu, B.; Yang, Y., Liquid Doping Materials as Micro-Carrier of Functional Molecules for Functionalization of Triboelectric Materials and Flexible Triboelectric Nanogenerators for Energy Harvesting and Gesture Detection. *Nano Energy* **2020,** *74*.

11. Jing, T.; Xu, B.; Guan, X.; Yang, Y.; Wu, M.; Jiang, C., Liquid-Filling Polydimethylsiloxane Composites with Enhanced Triboelectric Performance for Flexible Nanogenerators. *Macromolecular Materials and Engineering* **2020,** *305* (9), 2000275.

12. Tang, Y.; Xu, B.; Tan, D.; Han, J.; Gao, Y.; Li, Z.; Liu, X., Ultrastrong-polar cyano-Prussian blue analogs hybrid tribomaterials for biomechanical energy harvesting and self-powered sensing. *Nano Energy* **2023,** *110*.

13. Tang, Y.; Xu, B.; Gao, Y.; Li, Z.; Tan, D.; Li, M.; Liu, Y.; Huang, J., Ultrastrong-polar polyacrylonitrile organic-inorganic architected nanogenerators with synergistic triboelectric behavior for efficient biomechanical energy harvesting and self-powered sensing. *Nano Energy* **2022,** *103*.

14. Jing, T.; Xu, B.; Yang, Y.; Jiang, C.; Wu, M., Interfacial Modification Boosted Permittivity and Triboelectric Performance of Liquid Doping Composites for High-Performance Flexible

Triboelectric Nanogenerators. *Nano Energy* **2020,** *78*, 105374.

15. Wang, Q.; Xu, B.; Huang, J.; Tan, D., Natural Silkworm Cocoon-Based Hierarchically Architected Composite Triboelectric Nanogenerators for Biomechanical Energy Harvesting. *ACS Appl Mater Interfaces* **2023**.

16. Wang, Q.; Xu, B.; Tan, D.; Hu, X.; Yang, Y.; Huang, J.; Gao, Y.; Liu, X., Nature-inspired Scalable High-performance Triboelectric Nanogenerators for Energy Harvesting and Sensing. *Nano Energy* **2023**.

17. Tan, D.; Xu, B.; Gao, Y.; Tang, Y.; Liu, Y.; Yang, Y.; Li, Z., Breathable fabric-based triboelectric nanogenerators with open-porous architected polydimethylsiloxane coating for wearable applications. *Nano Energy* **2022,** *104*.

18. Jing, T.; Xu, B.; Yang, Y.; Li, M.; Gao, Y., Organogel electrode enables highly transparent and stretchable triboelectric nanogenerators of high power density for robust and reliable energy harvesting. *Nano Energy* **2020,** *78*.

19. Jing, T.; Xu, B.; Xin, J. H.; Guan, X.; Yang, Y., Series to parallel structure of electrode fiber: an effective method to remarkably reduce inner resistance of triboelectric nanogenerator textiles. *Journal of Materials Chemistry A* **2021,** *9* (20), 12331-12339.

20. Jing, T.; Xu, B.; Yang, Y., Organogel Electrode Based Continuous Fiber with Large-Scale Production for Stretchable Triboelectric Nanogenerator Textiles. *Nano Energy* **2021,** *84*, 105867.

21. Miao, F.; Shao, C.; Li, X.; Wang, K.; Lu, N.; Liu, Y., Electrospun Carbon

Nanofibers/Carbon Nanotubes/Polyaniline Ternary Composites with Enhanced Electrochemical Performance for Flexible Solid-State Supercapacitors. *ACS Sustainable Chemistry & Engineering* **2016,** *4* (3), 1689-1696.

22. Pandey, P.; Jung, D.-H.; Choi, G.-J.; Seo, M.-K.; Lee, S.; Kim, J. M.; Park, I.-K.; Sohn, J. I., Nafion-mediated barium titanate-polymer composite nanofibers-based triboelectric nanogenerator for self-powered smart street and home control system. *Nano Energy* **2023,** *107*.

23. Xiao, Y.; Li, Z.; Xu, B., Flexible Triboelectric Nanogenerators based on Hydrogel/g-C(3)N(4) Composites for Biomechanical Energy Harvesting and Self-Powered Sensing. *ACS Appl Mater Interfaces* **2024**.

24. Xiao, Y.; Xu, B.; Bao, Q.; Lam, Y., Wearable Triboelectric Nanogenerators Based on Polyamide Composites Doped with 2D Graphitic Carbon Nitride. *Polymers* **2022,** *14* (15).

25. Ye, Q.; Wu, Y.; Qi, Y.; Shi, L.; Huang, S.; Zhang, L.; Li, M.; Li, W.; Zeng, X.; Wo, H.; Wang, X.; Dong, S.; Ramakrishna, S.; Luo, J., Effects of Liquid Metal Particles on Performance of Triboelectric Nanogenerator with Electrospun Polyacrylonitrile Fiber Films. *Nano Energy* **2019,** *61*, 381-388.

26. Verners, O.; Lapčinskis, L.; Ģermane, L.; Kasikov, A.; Timusk, M.; Pudzs, K.; Ellis, A. V.; Sherrell, P. C.; Šutka, A., Smooth polymers charge negatively: Controlling contact electrification polarity in polymers. *Nano Energy* **2022,** *104*.

27. Šutka, A.; Mālnieks, K.; Lapčinskis, L.; Kaufelde, P.; Linarts, A.; Bērziņa, A.; Zābels, R.; Jurķāns, V.; Gorņevs, I.; Blūms, J.; Knite, M., The role of intermolecular forces in contact

electrification on polymer surfaces and triboelectric nanogenerators. *Energy & Environmental Science* **2019,** *12* (8), 2417-2421.

28. Zhou, L.; Liu, D.; Zhao, Z.; Li, S.; Liu, Y.; Liu, L.; Gao, Y.; Wang, Z. L.; Wang, J., Simultaneously Enhancing Power Density and Durability of Sliding-Mode Triboelectric Nanogenerator via Interface Liquid Lubrication. *Advanced Energy Materials* **2020,** *10* (45).

29. Zhang, Z.; Jiang, D.; Zhao, J.; Liu, G.; Bu, T.; Zhang, C.; Wang, Z. L., Tribovoltaic Effect on Metal–Semiconductor Interface for Direct-Current Low-Impedance Triboelectric Nanogenerators. *Advanced Energy Materials* **2020,** *10* (9).

30. Seol, M.; Kim, S.; Cho, Y.; Byun, K. E.; Kim, H.; Kim, J.; Kim, S. K.; Kim, S. W.; Shin, H. J.; Park, S., Triboelectric Series of 2D Layered Materials. *Adv Mater* **2018,** *30* (39), e1801210.

31. Chekke, T.; Narzary, R.; Ngadong, S.; Satpati, B.; Bayan, S.; Das, U., 2D WS2-Based Single-Electrode Triboelectric Nanogenerator for Power Generation and Motion Sensing. *Journal of Electronic Materials* **2023,** *52* (4), 2685-2694.

32. Liu, X.; Xu, F.; Li, Z.; Liu, Z.; Yang, W.; Zhang, Y.; Fan, H.; Yang, H. Y., Design strategy for MXene and metal chalcogenides/oxides hybrids for supercapacitors, secondary batteries and electro/photocatalysis. *Coordination Chemistry Reviews* **2022,** *464*.

33. Majed, A.; Kothakonda, M.; Wang, F.; Tseng, E. N.; Prenger, K.; Zhang, X.; Persson, P. O. A.; Wei, J.; Sun, J.; Naguib, M., Transition Metal Carbo-Chalcogenide "TMCC:" A New Family of 2D Materials. *Adv Mater* **2022,** *34* (26), e2200574.

34. Bayan, S.; Bhattacharya, D.; Mitra, R. K.; Ray, S. K., Self-powered flexible photodetectors based on Ag nanoparticle-loaded g-C3N4 nanosheets and PVDF hybrids: role of plasmonic and piezoelectric effects. *Nanotechnology* **2020,** *31* (36).

35. Gogotsi, Y.; Anasori, B., The Rise of MXenes. *ACS Nano* **2019,** *13* (8), 8491-8494.

36. Bukhari, H.; Iqbal, A. M.; Awan, S. U.; Hussain, D.; Shah, S. A.; Rizwan, S., Intercalation of C60 into MXene Multilayers: A Promising Approach for Enhancing the Electrochemical Properties of Electrode Materials for High-Performance Energy Storage Applications. *ACS Omega* **2024,** *9* (1), 227-238.

37. Kim, T. I.; Park, I. J.; Kang, S.; Kim, T. S.; Choi, S. Y., Enhanced Triboelectric Nanogenerator Based on Tungsten Disulfide via Thiolated Ligand Conjugation. *ACS Appl Mater Interfaces* **2021,** *13* (18), 21299-21309.

38. Zhou, Y.; Zhang, J. H.; Li, S.; Qiu, H.; Shi, Y.; Pan, L., Triboelectric Nanogenerators Based on 2D Materials: From Materials and Devices to Applications. *Micromachines (Basel)* **2023,** *14* (5).

39. Li, M.; Li, T.; Jing, Y., Nb(2)S(2)C Monolayers with Transition Metal Atoms Embedded at the S Vacancy Are Promising Single-Atom Catalysts for CO Oxidation. *ACS Omega* **2023,** *8* (34), 31051-31059.

40. Xiao, Y.; Li, Z.; Tan, D.; Carsten, G.; Xu, B., Triboelectric Nanogenerators Based on Transition Metal Carbo-Chalcogenide (Nb2S2C and Ta2S2C) for Energy Harvesting and Self-Powered Sensing. *Advanced Science* **2024**.

41. Zou, H.; Zhang, Y.; Guo, L.; Wang, P.; He, X.; Dai, G.; Zheng, H.; Chen, C.; Wang, A. C.; Xu, C.; Wang, Z. L., Quantifying the triboelectric series. *Nat Commun* **2019,** *10* (1), 1427.

42. Zhong, W.; Xu, L.; Zhan, F.; Wang, H.; Wang, F.; Wang, Z. L., Dripping Channel Based Liquid Triboelectric Nanogenerators for Energy Harvesting and Sensing. *ACS Nano* **2020,** *14* (8), 10510-10517.

43. Jiang, C.; Wu, C.; Li, X.; Yao, Y.; Lan, L.; Zhao, F.; Ye, Z.; Ying, Y.; Ping, J., All-electrospun flexible triboelectric nanogenerator based on metallic MXene nanosheets. *Nano Energy* **2019,** *59*, 268-276.

44. Zhu, J.; Zhu, M.; Shi, Q.; Wen, F.; Liu, L.; Dong, B.; Haroun, A.; Yang, Y.; Vachon, P.; Guo, X.; He, T.; Lee, C., Progress in TENG technology—A journey from energy harvesting to nanoenergy and nanosystem. *EcoMat* **2020,** *2* (4), 12058.

45. Seung, W.; Gupta, M. K.; Lee, K. Y.; Shin, K. S.; Lee, J. H.; Kim, T. Y.; Kim, S.; Lin, J.; Kim, J. H.; Kim, S. W., Nanopatterned textile-based wearable triboelectric nanogenerator. *ACS Nano* **2015,** *9* (4), 3501-3509.

46. Guan, X.; Xu, B.; Wu, M.; Jing, T.; Yang, Y.; Gao, Y., Breathable, washable and wearable woven-structured triboelectric nanogenerators utilizing electrospun nanofibers for biomechanical energy harvesting and self-powered sensing. *Nano Energy* **2021,** *80*, 105549.

47. Qiao, H.; Zhang, Y.; Huang, Z.; Wang, Y.; Li, D.; Zhou, H., 3D printing individualized triboelectric nanogenerator with macro-pattern. *Nano Energy* **2018,** *50*, 126-132.

48. Ma, H.; Hsiao, B. S., Electrospun Nanofibrous Membranes for Desalination. In *Current*

Trends and Future Developments on (Bio-) Membranes, 2019; pp 81-104.

49. Ahmed, F. E.; Lalia, B. S.; Hashaikeh, R., A review on electrospinning for membrane fabrication: Challenges and applications. *Desalination* **2015,** *356*, 15-30.

50. Rocco, K. A.; Maxfield, M. W.; Best, C. A.; Dean, E. W.; Breuer, C. K., In vivo applications of electrospun tissue-engineered vascular grafts: a review. *Tissue Eng Part B Rev* **2014,** *20* (6), 628-640.

51. Zhu, G.; Su, Y.; Bai, P.; Chen, J.; Jing, Q.; Yang, W.; Wang, Z. L., Harvesting water wave energy by asymmetric screening of electrostatic charges on a nanostructured hydrophobic thin-film surface. *ACS Nano* **2014,** *8* (6), 6031-6037.

52. Ma, Z.; Ai, J.; Shi, Y.; Wang, K.; Su, B., A Superhydrophobic Droplet-Based Magnetoelectric Hybrid System to Generate Electricity and Collect Water Simultaneously. *Adv Mater* **2020,** *32* (50), e2006839.

53. Ray, S. S.; Chen, S.-S.; Nguyen, N. C.; Nguyen, H. T., Electrospinning: A Versatile Fabrication Technique for Nanofibrous Membranes for Use in Desalination. In *Nanoscale Materials in Water Purification*, 2019; pp 247-273.

54. Sha, Z.; Boyer, C.; Li, G.; Yu, Y.; Allioux, F.-M.; Kalantar-Zadeh, K.; Wang, C.-H.; Zhang, J., Electrospun liquid metal/PVDF-HFP nanofiber membranes with exceptional triboelectric performance. *Nano Energy* **2022,** *92*.

55. Pu, X.; Zha, J.-W.; Zhao, C.-L.; Gong, S.-B.; Gao, J.-F.; Li, R. K. Y., Flexible PVDF/nylon-11 electrospun fibrous membranes with aligned ZnO nanowires as potential

triboelectric nanogenerators. *Chemical Engineering Journal* **2020,** *398*.

56. Kim, Y.; Wu, X.; Lee, C.; Oh, J. H., Characterization of PI/PVDF-TrFE Composite Nanofiber-Based Triboelectric Nanogenerators Depending on the Type of the Electrospinning System. *ACS Appl Mater Interfaces* **2021**.

57. Bairagi, S.; Ali, S. W., Flexible lead-free PVDF/SM-KNN electrospun nanocomposite based piezoelectric materials: Significant enhancement of energy harvesting efficiency of the nanogenerator. *Energy* **2020,** *198*.

58. Lin, S.; Cheng, Y.; Mo, X.; Chen, S.; Xu, Z.; Zhou, B.; Zhou, H.; Hu, B.; Zhou, J., Electrospun Polytetrafluoroethylene Nanofibrous Membrane for High-Performance Self-Powered Sensors. *Nanoscale Res Lett* **2019,** *14* (1), 251.

59. Roy, S.; Maji, P. K.; Goh, K.-L., Sustainable design of flexible 3D aerogel from waste PET bottle for wastewater treatment to energy harvesting device. *Chemical Engineering Journal* **2021,** *413*.

60. Wen, R.; Fan, L.; Li, Q.; Zhai, J., A composite triboelectric nanogenerator based on flexible and transparent film impregnated with ZIF-8 nanocrystals. *Nanotechnology* **2021,** *32* (34).

61. Qi, D.; Zhang, K.; Tian, G.; Jiang, B.; Huang, Y., Stretchable Electronics Based on PDMS Substrates. *Adv Mater* **2020**, e2003155.

62. Mao, Y.; Li, Y.; Xie, J.; Liu, H.; Guo, C.; Hu, W., Triboelectric nanogenerator/supercapacitor in-one self-powered textile based on PTFE yarn wrapped

PDMS/MnO2NW hybrid elastomer. *Nano Energy* **2021,** *84*.

63. Alqadami, A. S. M.; Jamlos, M. F.; Jamlos, M. A., Efficacy of a wideband flexible antenna on a multilayer polymeric nanocomposites Fe3O4-PDMS substrate for wearable applications. *Current Applied Physics* **2019,** *19* (11), 1259-1265.

64. Guo, H.; Leng, Q.; He, X.; Wang, M.; Chen, J.; Hu, C.; Xi, Y., A Triboelectric Generator Based on Checker-Like Interdigital Electrodes with a Sandwiched PET Thin Film for Harvesting Sliding Energy in All Directions. *Advanced Energy Materials* **2015,** *5* (1).

65. Zou, Y.; Tan, P.; Shi, B.; Ouyang, H.; Jiang, D.; Liu, Z.; Li, H.; Yu, M.; Wang, C.; Qu, X.; Zhao, L.; Fan, Y.; Wang, Z. L.; Li, Z., A bionic stretchable nanogenerator for underwater sensing and energy harvesting. *Nat Commun* **2019,** *10* (1), 2695.

66. Zhang, R.; Dahlstrom, C.; Zou, H.; Jonzon, J.; Hummelgard, M.; Ortegren, J.; Blomquist, N.; Yang, Y.; Andersson, H.; Olsen, M.; Norgren, M.; Olin, H.; Wang, Z. L., Cellulose-Based Fully Green Triboelectric Nanogenerators with Output Power Density of 300 W m(-2). *Adv Mater* **2020**, e2002824.

67. Wang, Y.; Zhang, L.; Lu, A., Highly Stretchable, Transparent Cellulose/PVA Composite Hydrogel for Multiple Sensing and Triboelectric Nanogenerators. *Journal of Materials Chemistry A* **2020,** *8* (28), 13935-13941.

68. Shi, K.; Huang, X.; Sun, B.; Wu, Z.; He, J.; Jiang, P., Cellulose/BaTiO3 aerogel paper based flexible piezoelectric nanogenerators and the electric coupling with triboelectricity. *Nano Energy* **2019,** *57*, 450-458.

69. Sun, Z.; Yang, L.; Liu, S.; Zhao, J.; Hu, Z.; Song, W., A Green Triboelectric Nano-Generator Composite of Degradable Cellulose, Piezoelectric Polymers of PVDF/PA6, and Nanoparticles of BaTiO3. *Sensors (Basel)* **2020,** *20* (2).

70. Qian, C.; Li, L.; Gao, M.; Yang, H.; Cai, Z.; Chen, B.; Xiang, Z.; Zhang, Z.; Song, Y., All-printed 3D hierarchically structured cellulose aerogel based triboelectric nanogenerator for multi-functional sensors. *Nano Energy* **2019,** *63*.

71. Zhang, Y.; Zhou, Z.; Sun, L.; Liu, Z.; Xia, X.; Tao, T. H., Genetically engineered" biofunctional triboelectric nanogenerators using recombinant spider silk. *Advanced Materials* **2018,** *30* (50), 1805722.

72. Wen, D.-L.; Liu, X.; Deng, H.-T.; Sun, D.-H.; Qian, H.-Y.; Brugger, J.; Zhang, X.-S., Printed silk-fibroin-based triboelectric nanogenerators for multi-functional wearable sensing. *Nano Energy* **2019,** *66*, 104123.

73. Zhang, R.; Olin, H., Material choices for triboelectric nanogenerators: A critical review. *EcoMat* **2020,** *2* (4).

74. Guan, X.; Zheng, G.; Dai, K.; Liu, C.; Yan, X.; Shen, C.; Guo, Z., Carbon Nanotubes-Adsorbed Electrospun PA66 Nanofiber Bundles with Improved Conductivity and Robust Flexibility. *ACS Appl Mater Interfaces* **2016,** *8* (22), 14150-14159.

75. Wang, Z.; Zhang, F.; Yao, T.; Li, N.; Li, X.; Shang, J., Self-Powered Non-Contact Triboelectric Rotation Sensor with Interdigitated Film. *Sensors (Basel)* **2020,** *20* (17).

76. Ma, Z.; Huang, Q.; Xu, Q.; Zhuang, Q.; Zhao, X.; Yang, Y.; Qiu, H.; Yang, Z.; Wang, C.;

Chai, Y.; Zheng, Z., Permeable superelastic liquid-metal fibre mat enables biocompatible and monolithic stretchable electronics. *Nat Mater* **2021,** *20* (6), 859-868.

77. Chen, Y.; Xie, B.; Long, J.; Kuang, Y.; Chen, X.; Hou, M.; Gao, J.; Zhou, S.; Fan, B.; He, Y.; Zhang, Y. T.; Wong, C. P.; Wang, Z.; Zhao, N., Interfacial Laser-Induced Graphene Enabling High-Performance Liquid-Solid Triboelectric Nanogenerator. *Adv Mater* **2021**, e2104290.

78. Yang, Y.; Jing, T.; Xu, B., Self-Assembly of Porous Microstructured Polydimethylsiloxane Films for Wearable Triboelectric Nanogenerators. *Macromolecular Materials and Engineering* **2020,** *305* (9).

79. Yamada, T.; Hayamizu, Y.; Yamamoto, Y.; Yomogida, Y.; Izadi-Najafabadi, A.; Futaba, D. N.; Hata, K., A Stretchable Carbon Nanotube Strain Sensor for Human-Motion Detection. *Nat Nanotechnol* **2011,** *6* (5), 296-301.

80. Zhang, D.; Xu, Z.; Yang, Z.; Song, X., High-Performance Flexible Self-Powered Tin Disulfide Nanoflowers/Reduced Graphene Oxide Nanohybrid-Based Humidity Sensor Driven by Triboelectric Nanogenerator. *Nano Energy* **2020,** *67*.

81. Zhao, X. J.; Kuang, S. Y.; Wang, Z. L.; Zhu, G., Highly Adaptive Solid-Liquid Interfacing Triboelectric Nanogenerator for Harvesting Diverse Water Wave Energy. *ACS Nano* **2018,** *12* (5), 4280-4285.

82. Chen, X.; Iwamoto, M.; Shi, Z.; Zhang, L.; Wang, Z. L., Self-Powered Trace Memorization by Conjunction of Contact-Electrification and Ferroelectricity. *Advanced Functional Materials* **2015,** *25* (5), 739-747.

83. Nair, R. R.; Ren, W.; Jalil, R.; Riaz, I.; Kravets, V. G.; Britnell, L.; Blake, P.; Schedin, F.; Mayorov, A. S.; Yuan, S.; Katsnelson, M. I.; Cheng, H. M.; Strupinski, W.; Bulusheva, L. G.; Okotrub, A. V.; Grigorieva, I. V.; Grigorenko, A. N.; Novoselov, K. S.; Geim, A. K., Fluorographene: A Two-Dimensional Counterpart of Teflon. *Small* **2010,** *6* (24), 2877-2884.

84. Wang, N.; Wang, X. X.; Yan, K.; Song, W.; Fan, Z.; Yu, M.; Long, Y. Z., Anisotropic Triboelectric Nanogenerator Based on Ordered Electrospinning. *ACS Appl Mater Interfaces* **2020,** *12* (41), 46205-46211.

85. Pan, R.; Xuan, W.; Chen, J.; Dong, S.; Jin, H.; Wang, X.; Li, H.; Luo, J., Fully biodegradable triboelectric nanogenerators based on electrospun polylactic acid and nanostructured gelatin films. *Nano Energy* **2018,** *45*, 193-202.

86. Guo, H. Y.; Chen, J.; Wang, L. F.; Wang, A. C.; Li, Y. F.; An, C. H.; He, J. H.; Hu, C. G.; Hsiao, V. K. S.; Wang, Z. L., A highly efficient triboelectric negative air ion generator. *Nature Sustainability* **2020**.

87. Shuai, L.; Guo, Z. H.; Zhang, P.; Wan, J.; Pu, X.; Wang, Z. L., Stretchable, self-healing, conductive hydrogel fibers for strain sensing and triboelectric energy-harvesting smart textiles. *Nano Energy* **2020,** *78*, 105389.

88. Zhang, X.; Huang, H.; Zhang, W.; Hu, Z.; Li, X.; Liu, J.; Xu, G.; Yang, C., Self-powered triboelectric nanogenerator driven nanowires electrode array system for the urine sterilization. *Nano Energy* **2022,** *96*, 107111.

89. Jayababu, N.; Kim, D., Co/Zn bimetal organic framework elliptical nanosheets on flexible

conductive fabric for energy harvesting and environmental monitoring via triboelectricity. *Nano Energy* **2021,** *89*.

90. San, S. T.; Jo, S.; Roh, H.; Jayababu, N.; Kim, I.; Kim, Y.; Kim, D., Hybridized generator: Freely movable ferromagnetic nanoparticle-embedded balls for a self-powered tilt and direction sensor. *Extreme Mechanics Letters* **2020,** *41*, 101063.

91. An, S.; Sankaran, A.; Yarin, A. L., Natural Biopolymer-Based Triboelectric Nanogenerators via Fast, Facile, Scalable Solution Blowing. *ACS Appl Mater Interfaces* **2018,** *10* (43), 37749-37759.

92. Wang, Z.; Liu, Z.; Zhao, G.; Zhang, Z.; Zhao, X.; Wan, X.; Zhang, Y.; Wang, Z. L.; Li, L., Stretchable Unsymmetrical Piezoelectric BaTiO3 Composite Hydrogel for Triboelectric Nanogenerators and Multimodal Sensors. *ACS Nano* **2022**.

93. Yu, J.; Hou, X.; Cui, M.; Zhang, N.; Zhang, S.; He, J.; Chou, X., Skin-conformal BaTiO3/ecoflex-based piezoelectric nanogenerator for self-powered human motion monitoring. *Materials Letters* **2020,** *269*.

94. Xie, L.; Huang, X.; Yang, K.; Li, S.; Jiang, P., "Grafting to" route to PVDF-HFP-GMA/BaTiO3 nanocomposites with high dielectric constant and high thermal conductivity for energy storage and thermal management applications. *Journal of Materials Chemistry A* **2014,** *2* (15).

95. Sriphan, S.; Charoonsuk, T.; Maluangnont, T.; Vittayakorn, N., High-Performance Hybridized Composited-Based Piezoelectric and Triboelectric Nanogenerators Based on

BaTiO3/PDMS Composite Film Modified with Ti0.8O2 Nanosheets and Silver Nanopowders Cofillers. *Acs Applied Energy Materials* **2019,** *2* (5), 3840-3850.

96. Li, Z.; Wang, X.; Hu, Y.; Li, L.; Wang, C., Triboelectric Properties of BaTiO3/Polyimide Nanocomposite Film. *Applied Surface Science* **2022,** *572*.

97. Guan, X.; Xu, B.; Gong, J., Hierarchically Architected Polydopamine Modified BaTiO3@P(VDF-TrFE) Nanocomposite Fiber Mats for Flexible Piezoelectric Nanogenerators and Self-Powered Sensors. *Nano Energy* **2020,** *70*.

98. Li, Y.; Li, G.; Zhang, P.; Zhang, H.; Ren, C.; Shi, X.; Cai, H.; Zhang, Y.; Wang, Y.; Guo, Z.; Li, H.; Ding, G.; Cai, H.; Yang, Z.; Zhang, C.; Wang, Z. L., Contribution of Ferromagnetic Medium to the Output of Triboelectric Nanogenerators Derived from Maxwell's Equations. *Advanced Energy Materials* **2021**.

99. Vidyasagar, D.; Ghugal, S. G.; Umare, S. S.; Banavoth, M., Extended Pi-Conjugative N-P Type Homostructural Graphitic Carbon Nitride for Photodegradation and Charge-Storage Applications. *Sci Rep* **2019,** *9* (1), 7186.

100. Wu, Z.; Zhang, B.; Zou, H.; Lin, Z.; Liu, G.; Wang, Z. L., Multifunctional Sensor Based on Translational-Rotary Triboelectric Nanogenerator. *Advanced Energy Materials* **2019,** *9* (33).

101. Ma, T.; Gao, Q.; Li, Y.; Wang, Z.; Lu, X.; Cheng, T., An Integrated Triboelectric–Electromagnetic–Piezoelectric Hybrid Energy Harvester Induced by a Multifunction Magnet for Rotational Motion. *Advanced Engineering Materials* **2019,** *22* (2).

102. Luo, X.; Zhu, L.; Wang, Y. C.; Li, J.; Nie, J.; Wang, Z. L., A Flexible Multifunctional

Triboelectric Nanogenerator Based on MXene/PVA Hydrogel. *Advanced Functional Materials* **2021,** *31* (38).

103. Wang, Z.; Bu, T.; Li, Y.; Wei, D.; Tao, B.; Yin, Z.; Zhang, C.; Wu, H., Multidimensional Force Sensors Based on Triboelectric Nanogenerators for Electronic Skin. *ACS Appl Mater Interfaces* **2021**.

104. Dutta, T.; Yadav, N.; Wu, Y.; Cheng, G. J.; Liang, X.; Ramakrishna, S.; Sbai, A.; Gupta, R.; Mondal, A.; Hongyu, Z.; Yadav, A., Electronic properties of 2D materials and their junctions. *Nano Materials Science* **2023**.

105. Chaves, A.; Azadani, J. G.; Alsalman, H.; da Costa, D. R.; Frisenda, R.; Chaves, A. J.; Song, S. H.; Kim, Y. D.; He, D.; Zhou, J.; Castellanos-Gomez, A.; Peeters, F. M.; Liu, Z.; Hinkle, C. L.; Oh, S.-H.; Ye, P. D.; Koester, S. J.; Lee, Y. H.; Avouris, P.; Wang, X.; Low, T., Bandgap engineering of two-dimensional semiconductor materials. *npj 2D Materials and Applications* **2020,** *4* (1).

106. Liu, J.; Li, B.; Li, Q., Two-Dimensional Doped Materials. *Magnetochemistry* **2022,** *8* (12).

107. Xiao, Y.; Lu, J.; Xu, B., Synergistic effect study of g-C3N4 composites for high-performance triboelectric nanogenerators. *Energy Materials* **2025,** *5* (6).

108. Perera, A.; Madhushani, K. A. U.; Punchihewa, B. T.; Kumar, A.; Gupta, R. K., MXene-Based Nanomaterials for Multifunctional Applications. *Materials (Basel)* **2023,** *16* (3).

109. Palchoudhury, S.; Ramasamy, K.; Han, J.; Chen, P.; Gupta, A., Transition metal chalcogenides for next-generation energy storage. *Nanoscale Adv* **2023,** *5* (10), 2724-2742.

110. Kim, W. G.; Kim, D. W.; Tcho, I. W.; Kim, J. K.; Kim, M. S.; Choi, Y. K., Triboelectric Nanogenerator: Structure, Mechanism, and Applications. *ACS Nano* **2021,** *15* (1), 258-287.

111. Huang, T.; Lu, M.; Yu, H.; Zhang, Q.; Wang, H.; Zhu, M., Enhanced Power Output of a Triboelectric Nanogenerator Composed of Electrospun Nanofiber Mats Doped with Graphene Oxide. *Sci Rep* **2015,** *5*, 13942.

112. Wu, Y.; Luo, Y.; Qu, J.; Daoud, W. A.; Qi, T., Liquid single-electrode triboelectric nanogenerator based on graphene oxide dispersion for wearable electronics. *Nano Energy* **2019,** *64*.

113. Shen, D.; Duley, W. W.; Peng, P.; Xiao, M.; Feng, J.; Liu, L.; Zou, G.; Zhou, Y. N., Moisture-Enabled Electricity Generation: From Physics and Materials to Self-Powered Applications. *Adv Mater* **2020,** *32* (52), e2003722.

114. Maitra, A.; Paria, S.; Karan, S. K.; Bera, R.; Bera, A.; Das, A. K.; Si, S. K.; Halder, L.; De, A.; Khatua, B. B., Triboelectric Nanogenerator Driven Self-Charging and Self-Healing Flexible Asymmetric Supercapacitor Power Cell for Direct Power Generation. *ACS Appl Mater Interfaces* **2019,** *11* (5), 5022-5036.

115. Ma, C.; Wang, R.; Tetik, H.; Gao, S.; Wu, M.; Tang, Z.; Lin, D.; Ding, D.; Wu, W., Hybrid nanomanufacturing of mixed-dimensional manganese oxide/graphene aerogel macroporous hierarchy for ultralight efficient supercapacitor electrodes in self-powered ubiquitous nanosystems. *Nano Energy* **2019,** *66*.

116. Bao, Q.; Zhang, D.; Qi, P., Synthesis and characterization of silver nanoparticle and

graphene oxide nanosheet composites as a bactericidal agent for water disinfection. *J Colloid Interface Sci* **2011,** *360* (2), 463-470.

117. Liquid single-electrode triboelectric nanogenerator based on graphene oxide dispersion for wearable electronics supporting document.

118. Grutzmacher, P. G.; Suarez, S.; Tolosa, A.; Gachot, C.; Song, G.; Wang, B.; Presser, V.; Mucklich, F.; Anasori, B.; Rosenkranz, A., Superior Wear-Resistance of Ti3C2Tx Multilayer Coatings. *ACS Nano* **2021,** *15* (5), 8216-8224.

119. Kohlhauser, B.; Vladu, C. I.; Gachot, C.; Mayrhofer, P. H.; Rodríguez Ripoll, M., Reactive in-situ formation and self-assembly of MoS2 nanoflakes in carbon tribofilms for low friction. *Materials & Design* **2021,** *199*.

120. Zou, H.; Guo, L.; Xue, H.; Zhang, Y.; Shen, X.; Liu, X.; Wang, P.; He, X.; Dai, G.; Jiang, P.; Zheng, H.; Zhang, B.; Xu, C.; Wang, Z. L., Quantifying and understanding the triboelectric series of inorganic non-metallic materials. *Nat Commun* **2020,** *11* (1), 2093.

121. Liu, Y.; Li, E.; Yan, Y.; Lin, Z.; Chen, Q.; Wang, X.; Shan, L.; Chen, H.; Guo, T., A one-structure-layer PDMS/Mxenes based stretchable triboelectric nanogenerator for simultaneously harvesting mechanical and light energy. *Nano Energy* **2021,** *86*.

122. Liao, G.; Chen, S.; Quan, X.; Yu, H.; Zhao, H., Graphene Oxide Modified g-C3N4 Hybrid with Enhanced Photocatalytic Capability under Visible Light Irradiation. *J. Mater. Chem.* **2012,** *22* (6), 2721-2726.

123. Bayan, S.; Bhattacharya, D.; Mitra, R. K.; Ray, S. K., Two-Dimensional Graphitic Carbon

Nitride Nanosheets: A Novel Platform for Flexible, Robust and Optically Active Triboelectric Nanogenerators. *Nanoscale* **2020,** *12* (41), 21334-21343.

124. Peymanfar, R.; Selseleh-Zakerin, E.; Ahmadi, A., Tailoring Energy Band Gap and Microwave Absorbing Features of Graphite-Like Carbon Nitride (g-C3N4). *Journal of Alloys and Compounds* **2021,** *867*.

125. Hatta, F. F.; Mohammad Haniff, M. A. S.; Mohamed, M. A., A review on applications of graphene in triboelectric nanogenerators. *International Journal of Energy Research* **2021**.

126. VahidMohammadi, A.; Rosen, J.; Gogotsi, Y., The world of two-dimensional carbides and nitrides (MXenes). *Science* **2021,** *372* (6547).

127. Salauddin, M.; Rana, S. M. S.; Sharifuzzaman, M.; Lee, S. H.; Zahed, M. A.; Do Shin, Y.; Seonu, S.; Song, H. S.; Bhatta, T.; Park, J. Y., Laser-carbonized MXene/ZiF-67 nanocomposite as an intermediate layer for boosting the output performance of fabric-based triboelectric nanogenerator. *Nano Energy* **2022,** *100*.

128. Zhang, S.; Rana, S. M. S.; Bhatta, T.; Pradhan, G. B.; Sharma, S.; Song, H.; Jeong, S.; Park, J. Y., 3D printed smart glove with pyramidal MXene/Ecoflex composite-based toroidal triboelectric nanogenerators for wearable human-machine interaction applications. *Nano Energy* **2023,** *106*.

129. Yang, P.; Wang, P.; Diao, D., Graphene Nanosheets Enhanced Triboelectric Output Performances of PTFE Films. *ACS Applied Electronic Materials* **2022,** *4* (6), 2839-2850.

130. Ikram, M.; Mahmud, M. A. P., Advanced triboelectric nanogenerator-driven drug delivery

systems for targeted therapies. *Drug Deliv Transl Res* **2023,** *13* (1), 54-78.

131. Tat, T.; Libanori, A.; Au, C.; Yau, A.; Chen, J., Advances in triboelectric nanogenerators for biomedical sensing. *Biosensors and Bioelectronics* **2021,** *171*, 112714.

132. Yu, J. R.; Yang, X. X.; Gao, G. Y.; Xiong, Y.; Wang, Y. F.; Han, J.; Chen, Y. H.; Zhang, H.; Sun, Q. J.; Wang, Z. L., Bioinspired mechano-photonic artificial synapse based on graphene/MoS

heterostructure. *Science Advances* **2021,** *7* (12).

133. Pang, L.; Li, Z.; Zhao, Y.; Zhang, X.; Du, W.; Chen, L.; Yu, A.; Zhai, J., Triboelectric Nanogenerator Based on Polyimide/Boron Nitride Nanosheets/Polyimide Nanocomposite Film with Enhanced Electrical Performance. *ACS Applied Electronic Materials* **2022,** *4* (6), 3027-3035.

134. Shi, L.; Jin, H.; Dong, S.; Huang, S.; Kuang, H.; Xu, H.; Chen, J.; Xuan, W.; Zhang, S.; Li, S.; Wang, X.; Luo, J., High-performance triboelectric nanogenerator based on electrospun PVDF-graphene nanosheet composite nanofibers for energy harvesting. *Nano Energy* **2021,** *80*.

135. Tang, W.; Jiang, T.; Fan, F. R.; Yu, A. F.; Zhang, C.; Cao, X.; Wang, Z. L., Liquid-Metal Electrode for High-Performance Triboelectric Nanogenerator at an Instantaneous Energy Conversion Efficiency of 70.6%. *Advanced Functional Materials* **2015,** *25* (24), 3718-3725.

136. Chen, J.; Guo, H.; Zheng, J.; Huang, Y.; Liu, G.; Hu, C.; Wang, Z. L., Self-Powered Triboelectric Micro Liquid/Gas Flow Sensor for Microfluidics. *ACS Nano* **2016,** *10* (8), 8104-8112.

137. Lin, L.; Xie, Y.; Niu, S.; Wang, S.; Yang, P. K.; Wang, Z. L., Robust triboelectric nanogenerator based on rolling electrification and electrostatic induction at an instantaneous energy conversion efficiency of approximately 55%. *ACS Nano* **2015,** *9* (1), 922-930.

138. Xie, Y.; Wang, S.; Niu, S.; Lin, L.; Jing, Q.; Yang, J.; Wu, Z.; Wang, Z. L., Grating-structured freestanding triboelectric-layer nanogenerator for harvesting mechanical energy at 85% total conversion efficiency. *Adv Mater* **2014,** *26* (38), 6599-6607.

139. Guo, H.; Chen, J.; Yeh, M. H.; Fan, X.; Wen, Z.; Li, Z.; Hu, C.; Wang, Z. L., An ultrarobust high-performance triboelectric nanogenerator based on charge replenishment. *ACS Nano* **2015,** *9* (5), 5577-5584.

140. Tang, W.; Chen, B. D.; Wang, Z. L., Recent Progress in Power Generation from Water/Liquid Droplet Interaction with Solid Surfaces. *Advanced Functional Materials* **2019,** *29* (41), 1901069.

141. Liang, F.; Zhao, X. J.; Li, H. Y.; Fan, Y. J.; Cao, J. W.; Wang, Z. L.; Zhu, G., Stretchable shape-adaptive liquid-solid interface nanogenerator enabled by in-situ charged nanocomposite membrane. *Nano Energy* **2020,** *69*, 104414.

142. Xiao, Y., Design, Fabrication, and Application Study of Droplet Tube Based Triboelectric Nanogenerators. *Tribology in Industry* **2023,** *45* (4), 699-709.

143. Nguyen, Q.-T.; Ahn, K.-K. K., Fluid-Based Triboelectric Nanogenerators: A Review of Current Status and Applications. *International Journal of Precision Engineering and Manufacturing-Green Technology* **2020,** *8* (3), 1043-1060.

144. Lee, J. H.; Kim, S.; Kim, T. Y.; Khan, U.; Kim, S.-W., Water droplet-driven triboelectric nanogenerator with superhydrophobic surfaces. *Nano Energy* **2019,** *58*, 579-584.

145. Liang, Q.; Yan, X.; Liao, X.; Zhang, Y., Integrated multi-unit transparent triboelectric nanogenerator harvesting rain power for driving electronics. *Nano Energy* **2016,** *25*, 18-25.

146. Zhang, L. M.; Han, C. B.; Jiang, T.; Zhou, T.; Li, X. H.; Zhang, C.; Wang, Z. L., Multilayer wavy-structured robust triboelectric nanogenerator for harvesting water wave energy. *Nano Energy* **2016,** *22*, 87-94.

147. Zhang, S. L.; Xu, M.; Zhang, C.; Wang, Y.-C.; Zou, H.; He, X.; Wang, Z.; Wang, Z. L., Rationally designed sea snake structure based triboelectric nanogenerators for effectively and efficiently harvesting ocean wave energy with minimized water screening effect. *Nano Energy* **2018,** *48*, 421-429.

148. Yoo, D.; Park, S.-C.; Lee, S.; Sim, J.-Y.; Song, I.; Choi, D.; Lim, H.; Kim, D. S., Biomimetic anti-reflective triboelectric nanogenerator for concurrent harvesting of solar and raindrop energies. *Nano Energy* **2019,** *57*, 424-431.

149. Cheng, P.; Guo, H.; Wen, Z.; Zhang, C.; Yin, X.; Li, X.; Liu, D.; Song, W.; Sun, X.; Wang, J.; Wang, Z. L., Largely enhanced triboelectric nanogenerator for efficient harvesting of water wave energy by soft contacted structure. *Nano Energy* **2019,** *57*, 432-439.

150. Bai, Y.; Xu, L.; He, C.; Zhu, L.; Yang, X.; Jiang, T.; Nie, J.; Zhong, W.; Wang, Z. L., High-performance triboelectric nanogenerators for self-powered, in-situ and real-time water quality mapping. *Nano Energy* **2019,** *66*.

151. Gao, Y.; Li, Z.; Xu, B.; Li, M.; Jiang, C.; Guan, X.; Yang, Y., Scalable Core–Spun Coating Yarn-Based Triboelectric Nanogenerators with Hierarchical Structure for Wearable Energy Harvesting and Sensing via Continuous Manufacturing. *Nano Energy* **2022,** *91*.

152. Peng, X.; Dong, K.; Ye, C.; Jiang, Y.; Zhai, S.; Cheng, R.; Liu, D.; Gao, X.; Wang, J.; Wang, Z. L., A breathable, biodegradable, antibacterial, and self-powered electronic skin based on all-nanofiber triboelectric nanogenerators. *Science Advances 6* (26), eaba9624.

153. Niu, S.; Wang, S.; Lin, L.; Liu, Y.; Zhou, Y. S.; Hu, Y.; Wang, Z. L., Theoretical study of contact-mode triboelectric nanogenerators as an effective power source. *Energy & Environmental Science* **2013,** *6* (12).

154. Yang, Y.; Xu, B.; Li, M.; Gao, Y.; Han, J., Statistical modeling enabled design of high-performance conductive composite fiber materials for energy harvesting and self-powered sensing. *Chemical Engineering Journal* **2023,** *466*.

155. Li, Z.; Xu, B.; Han, J.; Huang, J.; Fu, H., A Polycation-Modified Nanofillers Tailored Polymer Electrolytes Fiber for Versatile Biomechanical Energy Harvesting and Full-Range Personal Healthcare Sensing. *Advanced Functional Materials* **2021**.

156. Jiang, C. M.; Li, X. J.; Ying, Y. B.; Ping, J. F., A multifunctional TENG yarn integrated into agrotextile for building intelligent agriculture. *Nano Energy* **2020,** *74*.

157. Kim, S.; Gupta, M. K.; Lee, K. Y.; Sohn, A.; Kim, T. Y.; Shin, K. S.; Kim, D.; Kim, S. K.; Lee, K. H.; Shin, H. J.; Kim, D. W.; Kim, S. W., Transparent flexible graphene triboelectric nanogenerators. *Adv Mater* **2014,** *26* (23), 3918-3925.

158. Chen, H.; Xu, Y.; Bai, L.; Jiang, Y.; Zhang, J.; Zhao, C.; Li, T.; Yu, H.; Song, G.; Zhang, N.; Gan, Q., Crumpled Graphene Triboelectric Nanogenerators: Smaller Devices with Higher Output Performance. *Advanced Materials Technologies* **2017,** *2* (6).

159. Han, S. A.; Lee, K. H.; Kim, T.-H.; Seung, W.; Lee, S. K.; Choi, S.; Kumar, B.; Bhatia, R.; Shin, H.-J.; Lee, W.-J.; Kim, S.; Kim, H. S.; Choi, J.-Y.; Kim, S.-W., Hexagonal boron nitride assisted growth of stoichiometric Al2O3 dielectric on graphene for triboelectric nanogenerators. Nano Energy 2015, 12, 556-566.

160. Park, S.; Park, J.; Kim, Y.-g.; Bae, S.; Kim, T.-W.; Park, K.-I.; Hong, B. H.; Jeong, C. K.; Lee, S.-K., Laser-directed synthesis of strain-induced crumpled MoS2 structure for enhanced triboelectrification toward haptic sensors. *Nano Energy* **2020,** *78*.

161. Cao, Y.; Guo, Y.; Chen, Z.; Yang, W.; Li, K.; He, X.; Li, J., Highly sensitive self-powered pressure and strain sensor based on crumpled MXene film for wireless human motion detection. *Nano Energy* **2022,** *92*.

162. Cui, P.; Wang, J.; Xiong, J.; Li, S.; Zhang, W.; Liu, X.; Gu, G.; Guo, J.; Zhang, B.; Cheng, G.; Du, Z., Meter-scale fabrication of water-driven triboelectric nanogenerator based on in-situ grown layered double hydroxides through a bottom-up approach. *Nano Energy* **2020,** *71*.

163. Wu, C.; Kim, T. W.; Choi, H. Y., Reduced graphene-oxide acting as electron-trapping sites in the friction layer for giant triboelectric enhancement. *Nano Energy* **2017,** *32*, 542-550.

164. Grutzmacher, P. G.; Cutini, M.; Marquis, E.; Ripoll, M. R.; Riedl, H.; Kutrowatz, P.; Bug, S.; Hsu, C. J.; Bernardi, J.; Righi, M. C.; Gachot, C.; Erdemir, A., Se Nano-Powder Conversion

into Lubricious 2D Selenide Layers by Tribochemical Reactions. *Adv Mater* **2023**, e2302076.

165. Li, L.; Hao, M.; Yang, X.; Sun, F.; Bai, Y.; Ding, H.; Wang, S.; Zhang, T., Sustainable and Flexible Hydrovoltaic Power Generator for Wearable Sensing Electronics. *Nano Energy* **2020,** *72*.

166. Gao, X.; Xing, F.; Guo, F.; Yang, Y.; Hao, Y.; Chen, J.; Chen, B.; Wang, Z. L., Turbine Disk-Type Triboelectric Nanogenerator for Wind Energy Harvesting and Self-Powered Wild Fire Pre-Warning. *Materials Today Energy* **2021**.

167. Li, Z.; Xu, B.; Han, J.; Tan, D.; Huang, J.; Gao, Y.; Fu, H., Surface-modified liquid metal nanocapsules derived multiple triboelectric composites for efficient energy harvesting and wearable self-powered sensing. *Chem. Eng. J.* **2023,** *460*, 141737.

168. Li, Z.; Xu, B.; Han, J.; Huang, J.; Fu, H., A Polycation-Modified Nanofillers Tailored Polymer Electrolytes Fiber for Versatile Biomechanical Energy Harvesting and Full-Range Personal Healthcare Sensing. *Adv. Funct. Mater.* **2022,** *32* (6), 2106731.

169. Chen, Y.; Li, J.; Lu, J.; Ding, M.; Chen, Y., Synthesis and Properties of Poly(vinyl Alcohol) Hydrogels with High Strength and Toughness. *Polymer Testing* **2022,** *108*.

170. Shen, Y.; Yang, L.; Xu, J.; Zhou, C.; Yuan, C.; Pan, X.; Cao, F.; Wang, H., Significantly Enhanced Energy Harvesting Based on Ba(Ti,Sn)O3 and P(VDF-CTFE) Composite by Piezoelectric and Triboelectric Hybrid. *Journal of Materials Science: Materials in Electronics* **2021**.

171. Ge, L.; Han, C., Synthesis of MWNTs/g-C3N4 Composite Photocatalysts with Efficient

Visible Light Photocatalytic Hydrogen Evolution Activity. *Applied Catalysis B: Environmental* **2012,** *117-118*, 268-274.

172. Wang, R.-C.; Lin, Y.-C.; Chen, H.-C.; Lin, W.-Y., Energy Harvesting from g-C3N4 Piezoelectric Nanogenerators. *Nano Energy* **2021,** *83*.

173. Ong, W. J.; Tan, L. L.; Ng, Y. H.; Yong, S. T.; Chai, S. P., Graphitic Carbon Nitride (g-C3N4)-Based Photocatalysts for Artificial Photosynthesis and Environmental Remediation: Are We a Step Closer To Achieving Sustainability? *Chem Rev* **2016,** *116* (12), 7159-7329.

174. Ma, L.; Fan, H.; Fu, K.; Lei, S.; Hu, Q.; Huang, H.; He, G., Protonation of Graphitic Carbon Nitride (g-C3N4) for an Electrostatically Self-Assembling Carbon@g-C3N4 Core–Shell Nanostructure toward High Hydrogen Evolution. *ACS Sustainable Chemistry & Engineering* **2017,** *5* (8), 7093-7103.

175. Wang, S.; Zhang, Y., A Functional Triboelectric Nanogenerator Based on the LiCl/PVA Hydrogel for Cheerleading Training. *Materials Technology* **2022**, 1-6.

176. Narkbuakaew, T.; Sujaridworakun, P., Synthesis of Tri-S-Triazine Based g-C3N4 Photocatalyst for Cationic Rhodamine B Degradation under Visible Light. *Topics in Catalysis* **2020,** *63* (11-14), 1086-1096.

177. Pareek, S.; Sharma, M.; Lal, S.; Quamara, J. K., Polymeric graphitic carbon nitride–barium titanate nanocomposites with different content ratios: a comparative investigation on dielectric and optical properties. *Journal of Materials Science: Materials in Electronics* **2018,** *29* (15), 13043-13051.

178. Zi, Y.; Niu, S.; Wang, J.; Wen, Z.; Tang, W.; Wang, Z. L., Standards and Figure-of-Merits for Quantifying the Performance of Triboelectric Nanogenerators. *Nat Commun* **2015,** *6*, 8376.

179. Kim, J. N.; Lee, J.; Lee, H.; Oh, I. K., Stretchable and Self-Healable Catechol-Chitosan-Diatom Hydrogel for Triboelectric Generator and Self-Powered Tremor Sensor Targeting at Parkinson Disease. *Nano Energy* **2021,** *82*.

180. Jiang, B.; Long, Y.; Pu, X.; Hu, W.; Wang, Z. L., A Stretchable, Harsh Condition-Resistant and Ambient-Stable Hydrogel and Its Applications in Triboelectric Nanogenerator. *Nano Energy* **2021,** *86*.

181. Chen, P.; Wang, Q.; Wan, X.; Yang, M.; Liu, C. L.; Xu, C.; Hu, B.; Feng, J. X.; Luo, Z. Q., Wireless Electrical Stimulation of the Vagus Nerves by Ultrasound-Responsive Programmable Hydrogel Nanogenerators for Anti-Inflammatory Therapy in Sepsis. *Nano Energy* **2021,** *89*.

182. Chen, T.; Shi, Q.; Zhu, M.; He, T.; Sun, L.; Yang, L.; Lee, C., Triboelectric Self-Powered Wearable Flexible Patch as 3D Motion Control Interface for Robotic Manipulator. *ACS Nano* **2018,** *12* (11), 11561-11571.

183. Sun, H.; Zhao, Y.; Jiao, S.; Wang, C.; Jia, Y.; Dai, K.; Zheng, G.; Liu, C.; Wan, P.; Shen, C., Environment Tolerant Conductive Nanocomposite Organohydrogels as Flexible Strain Sensors and Power Sources for Sustainable Electronics. *Advanced Functional Materials* **2021,** *31* (24).

184. Chang, Q.; He, Y.; Liu, Y.; Zhong, W.; Wang, Q.; Lu, F.; Xing, M., Protein Gel Phase

Transition: Toward Superiorly Transparent and Hysteresis-Free Wearable Electronics. *Advanced Functional Materials* **2020,** *30* (27).

185. Jeong, S.-H.; Lee, Y.; Lee, M.-G.; Song, W. J.; Park, J.-U.; Sun, J.-Y., Accelerated Wound Healing with An Ionic Patch Assisted by A Triboelectric Nanogenerator. *Nano Energy* **2021,** *79*.

186. Jakmuangpak, S.; Prada, T.; Mongkolthanaruk, W.; Harnchana, V.; Pinitsoontorn, S., Engineering Bacterial Cellulose Films by Nanocomposite Approach and Surface Modification for Biocompatible Triboelectric Nanogenerator. *ACS Applied Electronic Materials* **2020,** *2* (8), 2498-2506.

187. He, F.; You, X.; Gong, H.; Yang, Y.; Bai, T.; Wang, W.; Guo, W.; Liu, X.; Ye, M., Stretchable, Biocompatible, and Multifunctional Silk Fibroin-Based Hydrogels toward Wearable Strain/Pressure Sensors and Triboelectric Nanogenerators. *ACS Applied Materials & Interfaces* **2020,** *12* (5), 6442-6450.

188. Wang, X.; Wang, X.; Pi, M.; Ran, R., High-Strength, Highly Conductive and Woven Organic Hydrogel Fibers for Flexible Electronics. *Chemical Engineering Journal* **2022,** *428*.

189. Han, X.; Jiang, D.; Qu, X.; Bai, Y.; Cao, Y.; Luo, R.; Li, Z., A Stretchable, Self-Healable Triboelectric Nanogenerator as Electronic Skin for Energy Harvesting and Tactile Sensing. *Materials (Basel)* **2021,** *14* (7).

190. Bao, Q.; Zhang, S. F.; Zhang, D., Synthesis and Electrochemical Behavior of Two Microporous Polyoxomolybdates. *Advanced Materials Research* **2009,** *79-82*, 1479-1482.

191. Huang, Y.; Lai, F.; Zhang, L.; Lu, H.; Miao, Y. E.; Liu, T., Elastic Carbon Aerogels

Reconstructed from Electrospun Nanofibers and Graphene as Three-Dimensional Networked Matrix for Efficient Energy Storage/Conversion. *Sci Rep* **2016,** *6*, 31541.

192. Wang, Y.; Zhao, S.; Zhang, Y.; Fang, J.; Chen, W.; Yuan, S.; Zhou, Y., Facile Synthesis of Self-Assembled g-C3N4 with Abundant Nitrogen Defects for Photocatalytic Hydrogen Evolution. *ACS Sustainable Chemistry & Engineering* **2018,** *6* (8), 10200-10210.

193. Sun, J.-F.; Xu, Q.-Q.; Qi, J.-L.; Zhou, D.; Zhu, H.-Y.; Yin, J.-Z., Isolated Single Atoms Anchored on N-Doped Carbon Materials as a Highly Efficient Catalyst for Electrochemical and Organic Reactions. *ACS Sustainable Chemistry & Engineering* **2020,** *8* (39), 14630-14656.

194. Suzuki, Y.; Cardone, G.; Restrepo, D.; Zavattieri, P. D.; Baker, T. S.; Tezcan, F. A., Self-assembly of coherently dynamic, auxetic, two-dimensional protein crystals. *Nature* **2016,** *533* (7603), 369-373.

195. Grützmacher, P.; Gachot, C.; Eder, S. J., Visualization of microstructural mechanisms in nanocrystalline ferrite during grinding. *Materials & Design* **2020,** *195*.

196. Liu, J.; Fu, W.; Liao, Y.; Fan, J.; Xiang, Q., Recent advances in crystalline carbon nitride for photocatalysis. *Journal of Materials Science & Technology* **2021,** *91*, 224-240.

197. Grima, J. N.; Winczewski, S.; Mizzi, L.; Grech, M. C.; Cauchi, R.; Gatt, R.; Attard, D.; Wojciechowski, K. W.; Rybicki, J., Tailoring graphene to achieve negative Poisson's ratio properties. *Adv Mater* **2015,** *27* (8), 1455-1459.

198. Inagaki, M.; Tsumura, T.; Kinumoto, T.; Toyoda, M., Graphitic carbon nitrides (g-C3N4) with comparative discussion to carbon materials. *Carbon* **2019,** *141*, 580-607.

199. Li, Z.; Xu, B.; Han, J.; Huang, J.; Chung, K. Y., Interfacial Polarization and Dual Charge Transfer Induced High Permittivity of Carbon Dots-Based Composite as Humidity-Resistant Tribomaterial for Efficient Biomechanical Energy Harvesting. *Advanced Energy Materials* **2021**.

200. Cheng, X.; Miao, L.; Song, Y.; Su, Z.; Chen, H.; Chen, X.; Zhang, J.; Zhang, H., High efficiency power management and charge boosting strategy for a triboelectric nanogenerator. *Nano Energy* **2017,** *38*, 438-446.

201. Chung, K. Y.; Xu, B.; Tan, D.; Yang, Q.; Li, Z.; Fu, H., Naturally Crosslinked Biocompatible Carbonaceous Liquid Metal Aqueous I

nk Printing Wearable Electronics for Multi-Sensing and Energy Harvesting. *Nanomicro Lett* **2024,** *16* (1), 149.

202. Guan, X.; Xu, B.; Huang, J.; Jing, T.; Gao, Y., Fiber-Shaped Stretchable Triboelectric Nanogenerator with a Novel Synergistic Structure of Opposite Poisson's Ratios. *Chemical Engineering Journal* **2022,** *427*, 131698.

203. So, M. Y.; Xu, B.; Li, Z.; Lai, C. L.; Jiang, C., Flexible corrugated triboelectric nanogenerators for efficient biomechanical energy harvesting and human motion monitoring. *Nano Energy* **2023,** *106*.

204. Li, Z.; Xu, B.; Han, J.; Tan, D.; Huang, J.; Gao, Y.; Fu, H., Surface-modified liquid metal nanocapsules derived multiple triboelectric composites for efficient energy harvesting and wearable self-powered sensing. *Chemical Engineering Journal* **2023,** *460*.

205. Tang, J.-Y.; Er, C.-C.; Kong, X. Y.; Ng, B.-J.; Chew, Y.-H.; Tan, L.-L.; Mohamed, A. R.; Chai, S.-P., Two-dimensional interface engineering of g-C3N4/g-C3N4 nanohybrid: Synergy between isotype and p-n heterojunctions for highly efficient photocatalytic CO2 reduction. *Chemical Engineering Journal* **2023,** *466*.

206. Li, H.; Jing, Y.; Ma, X.; Liu, T.; Yang, L.; Liu, B.; Yin, S.; Wei, Y.; Wang, Y., Construction of a well-dispersed Ag/graphene-like g-C3N4 photocatalyst and enhanced visible light photocatalytic activity. *RSC Advances* **2017,** *7* (14), 8688-8693.

207. Bokobza, L.; Bruneel, J.-L.; Couzi, M., Raman Spectra of Carbon-Based Materials (from Graphite to Carbon Black) and of Some Silicone Composites. *C* **2015,** *1* (1), 77-94.

208. Hadjiivanov, K. I.; Panayotov, D. A.; Mihaylov, M. Y.; Ivanova, E. Z.; Chakarova, K. K.; Andonova, S. M.; Drenchev, N. L., Power of Infrared and Raman Spectroscopies to Characterize Metal-Organic Frameworks and Investigate Their Interaction with Guest Molecules. *Chem Rev* **2021,** *121* (3), 1286-1424.

209. Li, W.; Chen, F., Ultraviolet–visible absorption, Raman, vibration spectra of pure silver and Ag–Cu clusters: A density functional theory study. *Physica B: Condensed Matter* **2014,** *451*, 96-105.

210. Ha Pham, T. T.; Vu, X. H.; Dien, N. D.; Trang, T. T.; Kim Chi, T. T.; Phuong, P. H.; Nghia, N. T., Ag nanoparticles on ZnO nanoplates as a hybrid SERS-active substrate for trace detection of methylene blue. *RSC Adv* **2022,** *12* (13), 7850-7863.

211. Song, Y.; Gao, S.; Tian, J.; Zhang, H., Construction of Ag/g-C3N4 composites with

uniform-sized Ag nanoparticles and the application for sulfisoxazole degradation in the presence of visible radiation. *Journal of Environmental Chemical Engineering* **2020,** *8* (5).

212. Tan, D.; Xu, B.; Chung, K. Y.; Yang, Y.; Wang, Q.; Gao, Y.; Huang, J., Self-Adhesive, Detach-on-Demand, and Waterproof Hydrophobic Electronic Skins with Customized Functionality and Wearability. *Advanced Functional Materials* **2023**.

213. Yang, Y.; Xu, B.; Gao, Y.; Li, M., Conductive Composite Fiber with Customizable Functionalities for Energy Harvesting and Electronic Textiles. *ACS Appl Mater Interfaces* **2021**.

214. Niu, S.; Wang, Z. L., Theoretical systems of triboelectric nanogenerators. *Nano Energy* **2015,** *14*, 161-192.

215. Bulathsinghala, R. L.; Ravichandran, A.; Zhao, H.; Ding, W.; Dharmasena, R. D. I. G., The intrinsic impact of dielectric constant on output generation of triboelectric nanogenerators. *Nano Energy* **2024,** *123*.

216. Liu, Z.; Muhammad, M.; Cheng, L.; Xie, E.; Han, W., Improved Output Performance of Triboelectric Nanogenerators Based on Polydimethylsiloxane Composites by the Capacitive Effect of Embedded Carbon Nanotubes. *Applied Physics Letters* **2020,** *117* (14).

217. Wang, D.; Bao, Y.; Zha, J. W.; Zhao, J.; Dang, Z. M.; Hu, G. H., Improved dielectric properties of nanocomposites based on poly(vinylidene fluoride) and poly(vinyl alcohol)-functionalized graphene. *ACS Appl Mater Interfaces* **2012,** *4* (11), 6273-6279.

218. Saini, P.; Choudhary, V.; Singh, B. P.; Mathur, R. B.; Dhawan, S. K., Polyaniline–MWCNT nanocomposites for microwave absorption and EMI shielding. *Materials Chemistry*

and Physics **2009,** *113* (2-3), 919-926.

219. Suo, X.; Li, B.; Ji, H. F.; Mei, S. L.; Miao, S.; Gu, M. W.; Yang, Y. Z.; Jiang, D. S.; Cui, S. J.; Chen, L. G.; Chen, G. Y.; Wen, Z.; Huang, H. B., Dielectric layer doping for enhanced triboelectric nanogenerators. *Nano Energy* **2023,** *114*.

220. Javadi, M.; Heidari, A.; Darbari, S., Realization of enhanced sound-driven CNT-based triboelectric nanogenerator, utilizing sonic array configuration. *Current Applied Physics* **2018,** *18* (4), 361-368.

221. Sohn, J. I.; Cha, S. N.; Song, B. G.; Lee, S.; Kim, S. M.; Ku, J.; Kim, H. J.; Park, Y. J.; Choi, B. L.; Wang, Z. L.; Kim, J. M.; Kim, K., Engineering of efficiency limiting free carriers and an interfacial energy barrier for an enhancing piezoelectric generation. *Energy Environ. Sci.* **2013,** *6* (1), 97-104.

222. Lee, S.; Lee, J.; Ko, W.; Cha, S.; Sohn, J.; Kim, J.; Park, J.; Park, Y.; Hong, J., Solution-processed Ag-doped ZnO nanowires grown on flexible polyester for nanogenerator applications. *Nanoscale* **2013,** *5* (20), 9609-9614.

223. Alam, M. M.; Sultana, A.; Mandal, D., Biomechanical and Acoustic Energy Harvesting from TiO2 Nanoparticle Modulated PVDF Nanofiber Made High Performance Nanogenerator. *ACS Applied Energy Materials* **2018,** *1* (7), 3103-3112.

224. Sultana, A.; Alam, M. M.; Sadhukhan, P.; Ghorai, U. K.; Das, S.; Middya, T. R.; Mandal, D., Organo-lead halide perovskite regulated green light emitting poly(vinylidene fluoride) electrospun nanofiber mat and its potential utility for ambient mechanical energy harvesting

application. *Nano Energy* **2018,** *49*, 380-392.

225. Karan, S. K.; Maiti, S.; Agrawal, A. K.; Das, A. K.; Maitra, A.; Paria, S.; Bera, A.; Bera, R.; Halder, L.; Mishra, A. K.; Kim, J. K.; Khatua, B. B., Designing high energy conversion efficient bio-inspired vitamin assisted single-structured based self-powered piezoelectric/wind/acoustic multi-energy harvester with remarkable power density. *Nano Energy* **2019,** *59*, 169-183.

226. Sun, B.; Li, X.; Zhao, R.; Ji, H.; Qiu, J.; Zhang, N.; He, D.; Wang, C., Electrospun poly(vinylidene fluoride)-zinc oxide hierarchical composite fiber membrane as piezoelectric acoustoelectric nanogenerator. *Journal of Materials Science* **2018,** *54* (3), 2754-2762.

227. Sultana, A.; Alam, M. M.; Ghosh, S. K.; Middya, T. R.; Mandal, D., Energy harvesting and self-powered microphone application on multifunctional inorganic-organic hybrid nanogenerator. *Energy* **2019,** *166*, 963-971.

228. Li, G.-Z.; Cai, Y.-W.; Wang, G.-G.; Sun, N.; Li, F.; Zhou, H.-L.; Zhang, X.-N.; Zhao, H.-X.; Wang, Y.; Han, J.-C.; Yang, Y., Performance enhancement of transparent and flexible triboelectric nanogenerator based on one-dimensionally hybridized copper/polydimethylsiloxane film. *Nano Energy* **2022,** *99*.

229. Mu, J.; Song, J.; Han, X.; Xian, S.; Hou, X.; He, J.; Chou, X., Dual-Mode Self-Powered Rainfall Sensor Based on Interfacial-Polarization-Enhanced and Nanocapacitor-Embedded FCB@PDMS Composite Film. *Advanced Materials Technologies* **2022,** *7* (6).